

Washington University in St. Louis

## Washington University Open Scholarship

---

All Theses and Dissertations (ETDs)

---

January 2010

### Adaptive OFDM Radar for Target Detection and Tracking

Satyabrata Sen

*Washington University in St. Louis*

Follow this and additional works at: <https://openscholarship.wustl.edu/etd>

---

#### Recommended Citation

Sen, Satyabrata, "Adaptive OFDM Radar for Target Detection and Tracking" (2010). *All Theses and Dissertations (ETDs)*. 318.

<https://openscholarship.wustl.edu/etd/318>

This Dissertation is brought to you for free and open access by Washington University Open Scholarship. It has been accepted for inclusion in All Theses and Dissertations (ETDs) by an authorized administrator of Washington University Open Scholarship. For more information, please contact [digital@wumail.wustl.edu](mailto:digital@wumail.wustl.edu).

WASHINGTON UNIVERSITY IN ST. LOUIS  
School of Engineering and Applied Science  
Department of Electrical & Systems Engineering

Dissertation Examination Committee:

Dr. Arye Nehorai, Chair  
Dr. R. Martin Arthur  
Dr. I. Norman Katz  
Dr. Nan Lin  
Dr. Hiro Mukai  
Dr. Carlos H. Muravchik

ADAPTIVE OFDM RADAR FOR TARGET DETECTION AND TRACKING

by

Satyabrata Sen

A dissertation presented to the Graduate School of Arts and Sciences  
of Washington University in partial fulfillment of the  
requirements for the degree of

DOCTOR OF PHILOSOPHY

December 2010  
Saint Louis, Missouri

copyright by  
Satyabrata Sen  
2010

## ABSTRACT OF THE DISSERTATION

Adaptive OFDM Radar for Target Detection and Tracking

by

Satyabrata Sen

Doctor of Philosophy in Electrical Engineering

Washington University in St. Louis, December 2010

Research Advisor: Dr. Arye Nehorai

We develop algorithms to detect and track targets by employing a wideband orthogonal frequency division multiplexing (OFDM) radar signal. The frequency diversity of the OFDM signal improves the sensing performance since the scattering centers of a target resonate variably at different frequencies. In addition, being a wideband signal, OFDM improves the range resolution and provides spectral efficiency.

We first design the spectrum of the OFDM signal to improve the radar's wideband ambiguity function. Our designed waveform enhances the range resolution and motivates us to use adaptive OFDM waveform in specific problems, such as the detection and tracking of targets.

We develop methods for detecting a moving target in the presence of multipath, which exist, for example, in urban environments. We exploit the multipath reflections by utilizing different Doppler shifts. We analytically evaluate the asymptotic performance of the detector and adaptively design the OFDM waveform, by maximizing the noncentrality-parameter expression, to further improve the detection performance.

Next, we transform the detection problem into the task of a sparse-signal estimation by making use of the sparsity of multiple paths. We propose an efficient sparse-recovery algorithm by employing a collection of multiple small Dantzig selectors, and analytically compute the reconstruction performance in terms of the  $\ell_1$ -constrained minimal singular value. We solve a constrained multi-objective optimization algorithm to design the OFDM waveform and infer that the resultant signal-energy distribution is in proportion to the distribution of the target energy across different subcarriers.

Then, we develop tracking methods for both a single and multiple targets. We propose a tracking method for a low-grazing angle target by realistically modeling different physical and statistical effects, such as the meteorological conditions in the troposphere, curved surface of the earth, and roughness of the sea-surface. To further enhance the tracking performance, we integrate a maximum mutual information based waveform design technique into the tracker.

To track multiple targets, we exploit the inherent sparsity on the delay-Doppler plane to develop an computationally efficient procedure. For computational efficiency, we use more prior information to dynamically partition a small portion of the delay-Doppler plane. We utilize the block-sparsity property to propose a block version of the CoSaMP algorithm in the tracking filter.

# Acknowledgments

I am sincerely grateful to my research advisor, Dr. Arye Nehorai, for his valuable guidance throughout my doctoral research. I thank him for leading me to interesting research topics and giving me the freedom to explore different avenues that I found truly exciting. I feel fortunate to be a part of his excellent research group.

I would like to thank my dissertation committee members, Dr. R. Martin Arthur, Dr. I. Norman Katz, Dr. Nan Lin, Dr. Hiro Mukai, and Dr. Carlos H. Muravchik, for carefully revising and providing constructive suggestions to this dissertation. I especially thank Dr. Lynnea Brumbaugh for her editorial suggestions on this dissertation.

My sincere gratitude goes to my instructors, including Dr. Dibyen Majumdar, Dr. Dan Schonfeld, and Dr. Daniela Tuninetti from University of Illinois at Chicago, and Dr. Daniel R. Fuhrmann, Dr. Joseph A. O'Sullivan, Dr. Barry E. Spielman, and Dr. T. J. Tarn from Washington University in Saint Louis, for helping me to build a strong background of my research work. I would also like to thank all the staff members of the Electrical & Systems Engineering Department at WashU for their time and help.

I convey my heartiest thanks and warm regards to all my past and present labmates. Their friendships made our lab not only a wonderful place for research but also for fun that I will cherish forever. Particularly, I thank Mr. Murat Akçakaya for his friendship and constant support in my research over the last five years. I thank Mr. Gongguo Tang for his collaboration on my research. I am also thankful to my friends from Chicago and Saint Louis for being with me throughout this wonderful journey.

I offer my deepest gratitude to my parents and family in India for their endless love and emotional support. Their unlimited care and encouragement have always provided me with an indispensable inspiration. This dissertation is dedicated to them.

Satyabrata Sen

*Washington University in Saint Louis*  
*December 2010*

To my parents.

# Contents

<b>Abstract</b> . . . . .	<b>ii</b>
<b>Acknowledgments</b> . . . . .	<b>iv</b>
<b>List of Tables</b> . . . . .	<b>ix</b>
<b>List of Figures</b> . . . . .	<b>x</b>
<b>List of Abbreviations</b> . . . . .	<b>xiv</b>
<b>List of Notations</b> . . . . .	<b>xv</b>
<b>1 Introduction</b> . . . . .	<b>1</b>
1.1 Motivation of OFDM in Radar Processing . . . . .	3
1.2 Survey of Existing OFDM Radar . . . . .	6
1.3 Our Contributions . . . . .	8
1.4 Outline of the Dissertation . . . . .	12
<b>2 Waveform Design to Improve Wideband Ambiguity Function</b> . . . . .	<b>13</b>
2.1 Introduction . . . . .	14
2.2 Signal Model and Wideband Ambiguity Function . . . . .	15
2.2.1 Signal Model . . . . .	16
2.2.2 WAF of a Single Pulse . . . . .	18
2.2.3 WAF of a Pulse Train . . . . .	21
2.3 Adaptive Waveform Design . . . . .	22
2.4 Numerical Results . . . . .	24
2.5 Summary . . . . .	27
<b>3 Target Detection in Multipath Scenarios</b> . . . . .	<b>28</b>
3.1 Introduction . . . . .	29
3.2 Problem Description and Modeling . . . . .	31
3.2.1 Measurement Model . . . . .	32
3.2.2 Statistical Assumptions . . . . .	35
3.3 Detection Test . . . . .	35
3.4 Adaptive Waveform Design . . . . .	37
3.4.1 Distributions of the Test Statistic for Known Target Velocity . . . . .	38
3.4.2 Waveform Design . . . . .	41



3.5	Temporally Correlated Noise . . . . .	42
3.5.1	Statistical Assumptions . . . . .	43
3.5.2	Detection Test Under Temporal Correlations . . . . .	44
3.6	Numerical Results . . . . .	45
3.7	Summary . . . . .	52
<b>4</b>	<b>Waveform Design Based on Multi-Objective Optimization . . . . .</b>	<b>54</b>
4.1	Introduction . . . . .	55
4.2	Problem Description and Modeling . . . . .	58
4.2.1	Sparse Measurement Model . . . . .	59
4.2.2	Statistical Assumptions . . . . .	62
4.3	Sparse Recovery and Performance Analysis . . . . .	62
4.3.1	Sparse Recovery . . . . .	62
4.3.2	Performance Analysis . . . . .	64
4.4	Adaptive Waveform Design . . . . .	67
4.4.1	Minimizing the Error Bound . . . . .	67
4.4.2	Maximizing the Mahalanobis-Distance . . . . .	68
4.4.3	Multi-Objective Optimization . . . . .	70
4.5	Numerical Results . . . . .	71
4.6	Summary . . . . .	82
<b>5</b>	<b>Target Tracking in Low-Grazing Angle Scenarios . . . . .</b>	<b>84</b>
5.1	Introduction . . . . .	85
5.2	Tropospheric Propagation Models . . . . .	87
5.3	Problem Description and Modeling . . . . .	90
5.3.1	Dynamic State Model . . . . .	90
5.3.2	Measurement Model . . . . .	92
5.3.3	Clutter Model . . . . .	96
5.3.4	Statistical Assumptions . . . . .	97
5.4	Tracking Filter . . . . .	99
5.5	Adaptive Waveform Design . . . . .	100
5.5.1	Mutual Information . . . . .	102
5.5.2	Waveform Design . . . . .	103
5.6	Numerical Results . . . . .	105
5.7	Summary . . . . .	112
<b>6</b>	<b>Multi-Target Tracking Using Delay-Doppler Sparsity . . . . .</b>	<b>113</b>
6.1	Introduction . . . . .	113
6.2	Problem Description and Modeling . . . . .	116
6.2.1	Dynamic State Model . . . . .	116
6.2.2	Measurement Model . . . . .	119
6.3	Sparse Modeling . . . . .	123
6.3.1	Block Sparsity . . . . .	123

6.3.2	Sparse Measurement Model . . . . .	125
6.3.3	Properties of the Measurement Matrix and Coherence Measures	126
6.3.4	Minimizing the Block-Coherence . . . . .	128
6.4	Tracking Filter . . . . .	130
6.5	Numerical Results . . . . .	132
6.6	Summary . . . . .	139
<b>7</b>	<b>Conclusions . . . . .</b>	<b>141</b>
7.1	Key Contributions . . . . .	141
7.2	Future Work . . . . .	143
<b>Appendix A</b>	. . . . .	<b>145</b>
<b>Appendix B</b>	. . . . .	<b>146</b>
<b>Appendix C</b>	. . . . .	<b>148</b>
<b>Appendix D</b>	. . . . .	<b>150</b>
<b>Appendix E</b>	. . . . .	<b>152</b>
<b>References</b>	. . . . .	<b>154</b>
<b>Vita</b>	. . . . .	<b>170</b>

# List of Tables

6.1	BCoSaMP Recovery Algorithm . . . . .	131
6.2	Average time (in seconds) to compute the estimated state per pulse interval . . . . .	140

# List of Figures

1.1	Basic principle of radar. . . . .	2
1.2	An OFDM signal in (a) time and (b) frequency domains. . . . .	3
1.3	Principle of adaptive waveform design in radar. . . . .	4
1.4	Variations of RCS of a (a) thin dipole and (b) perfectly conducting sphere with respect to frequency. . . . .	5
2.1	(a) Ideal and (b) thumbtack ambiguity functions. . . . .	15
2.2	Plots of wideband ambiguity functions for (a) fixed and (b) adaptive waveforms over a region $\mathcal{R} = \{ \tau  \leq T,  \nu  \leq 1/(2T_{\text{PRI}})\}$ . . . . .	25
2.3	(a) Zero-Doppler cuts (auto-correlation functions) and (b) zero-delay cuts of the wideband ambiguity functions corresponding to the adaptive and fixed waveforms. . . . .	26
2.4	Distributions of signal energy and target response over different OFDM subcarriers (a) before and (b) after the optimization process. . . . .	27
3.1	The exploitation of multipath propagations increases the spatial diversity. . . . .	30
3.2	A schematic representation of the multipath scenario considered for numerical examples. . . . .	46
3.3	Effects of different SNR values on detection probability as a function of probability of false alarm. . . . .	47
3.4	Effects of different number of subcarriers on detection probability as a function of probability of false alarm. . . . .	48
3.5	Effects of different directions of target velocity vector on detection probability as a function of probability of false alarm. . . . .	48
3.6	Effects of exploiting the multipath reflections on detection probability as a function of probability of false alarm. . . . .	49
3.7	Effects of ignoring the multipath reflections at the detector on detection probability as a function of probability of false alarm. . . . .	50
3.8	Gain due to adaptive waveform design of detection probability as a function of probability of false alarm. . . . .	51
3.9	Effects of different temporal correlations on detection probability as a function of probability of false alarm. . . . .	51
3.10	Loss due to the target-velocity estimation of detection probability as a function of probability of false alarm. . . . .	52
4.1	A schematic representation of the multipath scenario. . . . .	58

4.2	A schematic representation of the multipath scenario considered in the numerical examples. . . . .	72
4.3	Comparison of performances of the standard Dantzig selector and decomposed Dantzig selector to detect Target 1 in terms of the (a) normalized RMSE, (b) empirical ROC, and (c) computation time with respect to the target to clutter-plus-noise ratio. . . . .	74
4.4	Comparison of performances of the standard Dantzig selector and decomposed Dantzig selector to detect Target 2 in terms of the (a) normalized RMSE, (b) empirical ROC, and (c) computation time with respect to the target to clutter-plus-noise ratio. . . . .	76
4.5	Results of the NSGA-II for Target 1: (a), (b) optimal solutions and values of the objective functions at the 0-th generation; (c), (d) optimal solutions and values of the objective functions at the 5-th generation; and (e), (f) optimal solutions and values of the objective functions at the 50-th generation. . . . .	77
4.6	Results of the NSGA-II for Target 2: (a), (b) optimal solutions and values of the objective functions at the 0-th generation; (c), (d) optimal solutions and values of the objective functions at the 5-th generation; and (e), (f) optimal solutions and values of the objective functions at the 50-th generation. . . . .	78
4.7	Comparison of performances due to the fixed and adaptive waveforms to detect Target 1 in terms of the (a) normalized RMSE and (b) empirical ROC with respect to the target to clutter-plus-noise ratio. . .	79
4.8	Comparison of performances due to the fixed and adaptive waveforms to detect Target 2 in terms of the (a) normalized RMSE and (b) empirical ROC with respect to the target to clutter-plus-noise ratio. . .	80
4.9	Results of the NSGA-II for Target 3: (a), (b) optimal solutions and values of the objective functions at the 50-th generation. . . . .	81
4.10	Comparison of performances due to the fixed and adaptive waveforms to detect Target 3 in terms of the (a) normalized RMSE and (b) empirical ROC with respect to the target to clutter-plus-noise ratio. . .	82
5.1	Low-grazing angle tracking is a challenging problem in maritime applications. . . . .	85
5.2	Equivalent representations of curved and flat earth models. . . . .	89
5.3	(a) Direct-direct, (b) direct-reflected, (c) reflected-direct, and (b) reflected-reflected signal paths. . . . .	93
5.4	Flowchart of the key steps involved in the tracking and waveform design procedure. . . . .	101
5.5	Comparison of the (a) true and estimated trajectories and (b) associated errors in position estimation due to the earth's curvature and standard lower atmosphere modeling. . . . .	106

5.6	Absolute error in scattering coefficients at three different frequencies with (solid lines) and without (dotted lines) considering earth's curvature and standard lower atmosphere modeling. . . . .	107
5.7	Comparison of the (a) true and estimated trajectories and (b) associated errors in position estimation due to the earth's curvature and evaporating duct modeling. . . . .	108
5.8	Absolute error in scattering coefficients at three different frequencies with (solid lines) and without (dotted lines) considering earth's curvature and evaporation duct modeling. . . . .	108
5.9	Comparison of the (a) true and estimated trajectories and (b) associated errors in position estimation due to the OFDM MIMO configurations. . . . .	109
5.10	Comparison of the (a) true and estimated trajectories and (b) associated errors in position estimation due to the polarization-sensitive transceivers. . . . .	110
5.11	Comparison of the (a) true and estimated trajectories and (b) associated errors in position estimation due to the fixed and adaptive waveforms. . . . .	111
5.12	Absolute error in scattering coefficients at three different frequencies with fixed (dotted lines) and adaptive (solid lines) waveforms. . . . .	111
6.1	A schematic representation of a multi-target tracking scenario (not drawn to scale). . . . .	117
6.2	Description of a particular target dynamics for two consecutive pulse intervals. . . . .	118
6.3	A schematic representation of the simulation scenario (not drawn to scale). . . . .	133
6.4	Comparison of the (a) true and estimated trajectories and (b) associated root-mean-squared errors in position estimation of two non-crossing target paths using the sparsity-based and PF-based tracking algorithms. . . . .	135
6.5	Comparison of the (a) true and estimated trajectories and (b) associated root-mean-squared errors in position estimation of two crossing target paths using the sparsity-based and PF-based tracking algorithms. . . . .	136
6.6	Comparison of the (a) true and estimated trajectories and (b) associated root-mean-squared errors in position estimation of two non-crossing target paths using the sparsity-based (with 50% measurements) and PF-based tracking algorithms. . . . .	137
6.7	Comparison of the (a) true and estimated trajectories and (b) associated root-mean-squared errors in position estimation of two crossing target paths using the sparsity-based (with 50% measurements) and PF-based tracking algorithms. . . . .	138

6.8	Comparison of the (a) true and estimated trajectories and (b) associated root-mean-squared errors in position estimation of two non-crossing target paths using the sparsity-based (with 10% measurements) and PF-based tracking algorithms. . . . .	139
6.9	Comparison of the (a) true and estimated trajectories and (b) associated root-mean-squared errors in position estimation of two crossing target paths using the sparsity-based (with 10% measurements) and PF-based tracking algorithms. . . . .	140

# List of Abbreviations

ACF	Auto-correlation function
AML	Approximate maximum likelihood
BCoSaMP	Block-CoSaMP
CFAR	Constant false alarm rate
CMSV	Constrained minimal singular value
CNR	Clutter-to-noise ratio
CoSaMP	Compressive sampling matching pursuit
CPI	Coherent processing interval
DS	Dantzig selector
DOA	Direction-of-arrival
GMANOVA	Generalized multivariate analysis of variance
GLR	Generalized likelihood ratio
LFM	Linear frequency modulation
LGA	Low-grazing angle
LOS	Line-of-sight
MCPC	Multi-carrier phase-coded
MIMO	Multiple-input multiple-output
MLE	Maximum likelihood estimate
MOEA	Multi-objective evolutionary algorithm
MOO	Multi-objective optimization
NSGA	Nondominated sorting genetic algorithm
OFDM	Orthogonal frequency division multiplexing
OMP	Orthogonal matching pursuit
PAPR	Peak-to-average power ratio
PRF	Pulse repetition frequency
PRI	Pulse repetition interval
RCS	Radar cross section
RIC	Restricted isometry constant
RMSE	Root mean squared error
ROC	Receiver operating characteristic
SISO	Single-input single-output
SNR	Signal-to-noise ratio
TCNR	Target to clutter-plus-noise ratio
TCR	Target-to-clutter ratio
UWB	Ultra-wideband
WAF	Wideband ambiguity function



# List of Notations

$a$	lowercase math italic denotes a scalar
$\mathbf{a}$	lowercase bold denotes a vector $\mathbf{a} \in \mathbb{C}^n$
$\mathbf{A}$	uppercase bold denotes a matrix $\mathbf{A} \in \mathbb{C}^{m \times n}$
$ \mathbf{A} $	determinant of $\mathbf{A}$
$[\mathbf{A}]_{(i,j)}$	$(i, j)$ -th element of $\mathbf{A}$
$\mathbf{A}^*$	conjugate of $\mathbf{A}$
$\mathbf{A}^T$	transpose of $\mathbf{A}$
$\mathbf{A}^H$	conjugate-transpose (Hermitian) of $\mathbf{A}$
$\mathbf{A}^-$	generalized inverse of $\mathbf{A}$ such that $\mathbf{A}\mathbf{A}^-\mathbf{A} = \mathbf{A}$
$\mathbf{A}^\dagger$	pseudo-inverse of $\mathbf{A}$ , defined as $\mathbf{A}^\dagger = (\mathbf{A}^H\mathbf{A})^{-1}\mathbf{A}^H$
$\text{vec}(\mathbf{A})$	forms a column vector of length $mn$ by stacking the columns of $\mathbf{A}$
$\text{tr}(\mathbf{A})$	trace of square matrix $\mathbf{A} \in \mathbb{C}^{n \times n}$
$\text{diag}(\dots)$	forms a square matrix with non-zero entries only on the main diagonal
$\mathbf{I}_n$	identity matrix of dimension $n$
$\text{Re}\{\cdot\}$	real part of a complex quantity
$\text{Im}\{\cdot\}$	imaginary part of a complex quantity
$\lceil \cdot \rceil$	nearest integer greater than a fractional quantity
$\ \cdot\ _0$	number of non-zero elements in a vector
$\ \cdot\ _p$	$p$ -th norm of a vector, $p = 1, 2$
$\ \cdot\ _\infty$	maximum of the absolute-valued elements in a vector
$\langle \cdot, \cdot \rangle$	inner-product operator
$\otimes$	Kronecker product operator
$\odot$	element-wise Hadamard product operator
$\mathcal{N}$	Gaussian distribution
$\mathbb{CN}_k$	complex Gaussian distribution of a vector of length $k$
$\mathbb{CN}_{k,l}$	complex Gaussian distribution of a matrix of dimension $k \times l$

# Chapter 1

## Introduction

Radar is an active, remote electromagnetic sensor used to surveil and detect different reflecting objects (or targets), such as aircrafts, missiles, ships, people, and even the natural environment. The word *radar* is derived from the phrase *radio detection and ranging*. Being an active sensing system, a radar has three primary functions: (i) it generates and transmits an electromagnetic signal towards a scene; (ii) it receives a backscattered portion of the transmitted energy from the scene towards the radar; and (iii) it processes the received signal to determine the presence of targets (*detection*) and their locations (*ranging*) in the presence of other undesired interfering echoes from the environment (usually referred to as *clutter*) [1]. Fig. 1.1 schematically depicts these functionalities.

During its early inception around the middle of the 1930s, the operational tasks of radar were limited only to detection and ranging. However, with the advent of World War II, radar technology developed tremendously, and soon the idea of ranging extended to include the direction and radial velocity of the target with respect to radar; see [1, Ch. 1.6], [2] for some historical references on radar. Presently, radar systems are very sophisticated and advanced, and they can provide more information about the

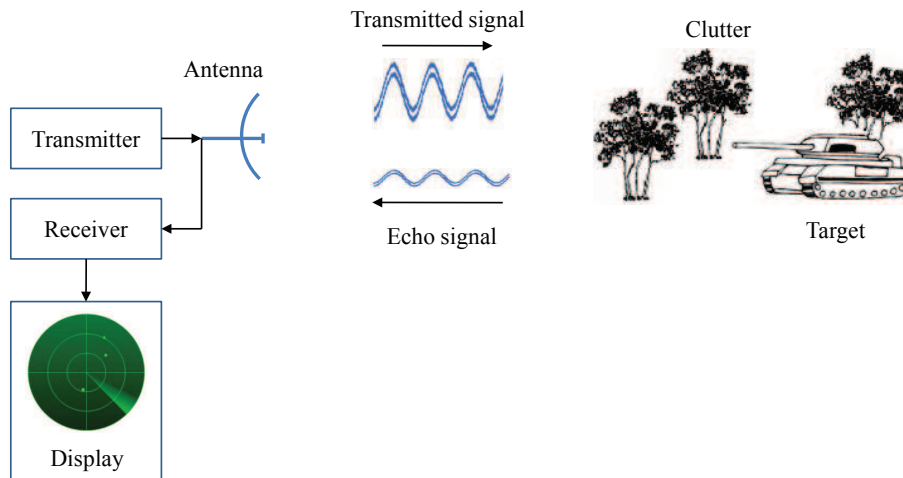


Figure 1.1: Basic principle of radar.

target, such as its shape, size, and trajectory. Modern radar signal designs are being conceived to further improve the resolution, accuracy, detection, discrimination, and identification capabilities. However, designing a radar signal to satisfy these different criteria poses a challenging task involving a lot of analytical and practical trade-offs.

In this dissertation, we propose to employ a wideband orthogonal frequency division multiplexing (OFDM) radar signal primarily for target detection and tracking problems. An OFDM signal is composed of a set of sub-carriers that are mathematically orthogonal in the time domain [3]; i.e., each carrier has an integer number of cycles over a symbol period (see Fig. 1.2). Consequently, the spectrum of each carrier has a null at the center frequency of the other carriers in the system, and thus a higher level of spectral efficiency can be achieved. In addition, we develop adaptive waveform design techniques to select the spectral parameters of the OFDM signal for further improving the sensing performances, as shown in Fig. 1.3. The estimated target and clutter parameters enable us to adaptively design the parameters of the next transmitting signal based on some optimality criteria. Recent advances in sensor

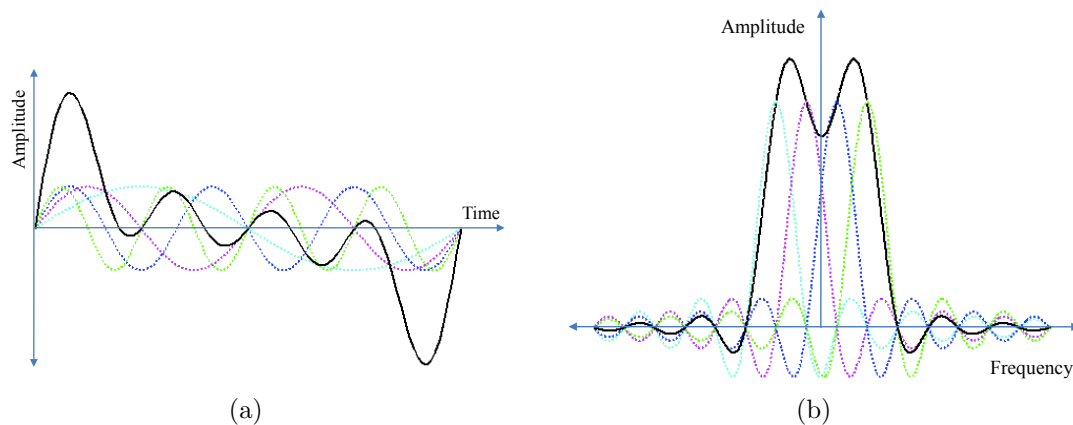


Figure 1.2: An OFDM signal in (a) time and (b) frequency domains.

information processing and flexible digital waveform modulator hardware make it feasible to adjust the transmit waveform on a periodic basis, as often as pulse-by-pulse if required. Thus, there is a potential to achieve the highest possible performance level even in a dynamically changing scenario through adaptive waveform design.

In this chapter, we first describe the motivation of using the OFDM signals in radar processing, along with a brief survey on the existing OFDM radar systems and methodologies. Then, we present in detail our contributions in this field.

## 1.1 Motivation of OFDM in Radar Processing

The range resolution of a radar system is inversely proportional to the transmitted signal bandwidth. Hence, the most obvious way to improve the range resolution is to shorten the pulse duration, since the bandwidth of a pulse is inversely proportional to its duration. On the other hand, for good detection capability a radar needs to transmit higher signal energy, and that is achieved by applying long duration pulses since the radar transmitters are typically operated near their peak power limitation.

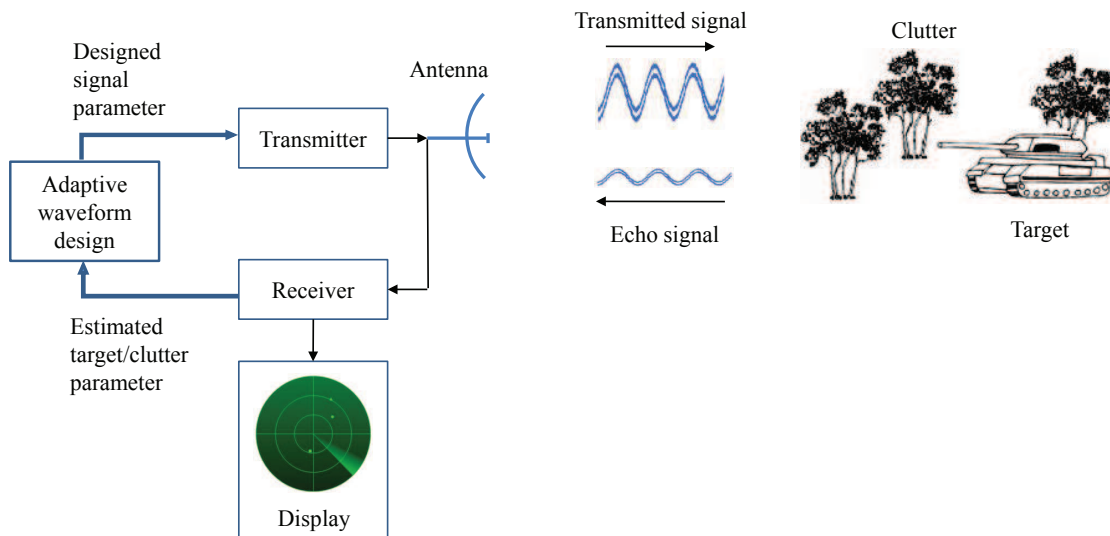


Figure 1.3: Principle of adaptive waveform design in radar.

Therefore, to overcome this dilemma on the pulse duration, in the late 1950s and early 1960s a new concept was developed, namely *pulse compression* [1, Ch. 6.5], [4, Ch. 7]. It uses a long duration pulse modulated in frequency or phase, i.e., with increased effective bandwidth, to simultaneously achieve the resolution of a short duration pulse and the energy of a long duration pulse.

Traditionally, there have been two classes of pulse compression techniques: linear frequency modulation (LFM) and phase coding. The basic concept of the LFM was first described in a patent issued in 1953 [5]. It involves a linear sweep of the carrier frequency across the desired bandwidth during the pulse duration. Effectively, this introduces a continuous quadratic phase shift over the duration of the transmit pulse. Alternatively, in the phase coding technique, a long pulse is divided into multiple identical segments, and each subpulse is coded with a different phase value. Thus, an increase in bandwidth is achieved since the rate of phase change over time corresponds to frequency. The simplest way to impart the phase change is by binary phase coding, an example of which is the Barker code [6]. When phase coding is done with more

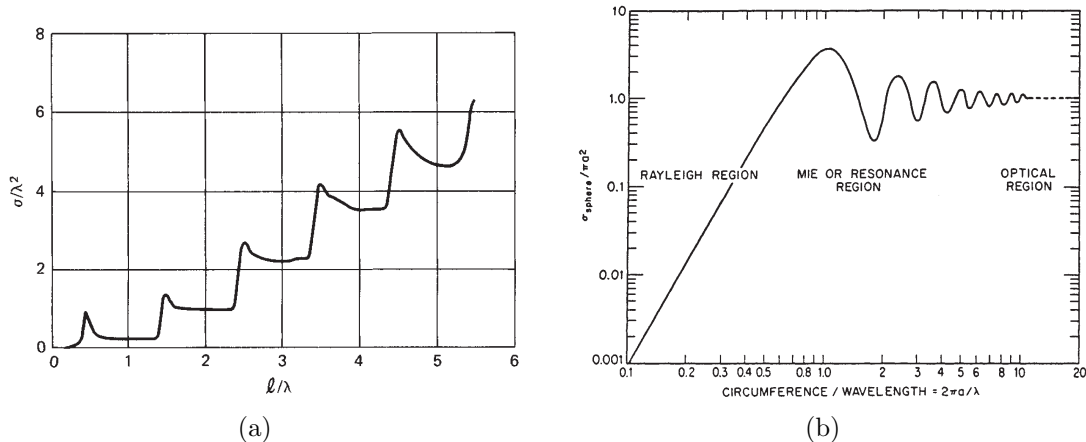


Figure 1.4: Variations of RCS of a (a) thin dipole and (b) perfectly conducting sphere with respect to frequency.

than two phase values the coded pulse is called polyphase code, examples of which are the Frank code [7], [8], four different P-codes [9], [10], etc.

Conventional LFM pulse compression does not have the similar pulse-to-pulse diversity as the phase codes have. It can only change the sign of the linear frequency slope. However, LFM has better spectral efficiency, since its spectrum is approximately rectangular in shape, whereas phase codes can have abrupt phase changes resulting in unintended spectral spread. Therefore, it is necessary to design a radar signal that can provide the benefits of both the LFM and phase coding. In this regard, a potential solution is the multi-carrier radar signals based on OFDM [11] – [16].

Along with providing improved range resolution and spectral efficiency, a multi-carrier OFDM signal also offers frequency diversity to the radar system. The advantage of using multiple frequencies has been well established in various radar applications, such as remote sensing of clouds and precipitation [17], detection of landmines [18], target-classification [19], interpretation of an urban scene [20], [21], etc. We know that the target responses strongly depend on the frequency content of the transmitted

signal [22]. For example, Fig. 1.4 shows the variations of the radar cross section (RCS) of a thin dipole and perfectly conducting sphere as a function of frequency [22, Figs. 11.7, 11.3]. Depending on their respective electrical lengths, different scattering centers of a target resonate at different transmitted frequencies and produce varying responses that can be exploited by a multi-carrier OFDM signal. Consequently, an OFDM radar can better discriminate a target from the background clutter when other standard processing is not effective. For example, Doppler processing cannot be used to detect a static or slowly moving target.

## 1.2 Survey of Existing OFDM Radar

The basic principle of OFDM has been in existence for several years as a multi-carrier, digital modulation technique for high-rate data communication [23]. Over the years, it has been used in wideband communication over mobile radio FM channels, asymmetric digital subscriber lines (ADSL) [24], European digital audio broadcasting (DAB), and terrestrial digital video broadcasting (DVB-T) standards [25]. It has also been chosen as the transmission technique for wireless local and metropolitan area networks in the HiperLAN/2, IEEE 802.11, and WiMAX standards [26], [27]; and for other wireline systems such as power line communication (PLC) [28].

However, the usage of the OFDM signal in radar applications is still in its infancy. Apart from the seminal work by Levanon on the multi-carrier phase-coded (MCPC) signal [16, Ch. 11], there have been only a few works on the OFDM-based radar signal processing. Poullin employed the coded OFDM (COFDM) signals of the European DAB and DVB standards in a passive radar system to improve the target-detection capability by canceling the unwanted zero-Doppler clutter effects [29]. Berger et al.

also followed the same signaling principle in a passive radar framework to estimate the targets' bi-static range and velocity using a sparsity-based approach [30], [31].

Several researchers have investigated the possibility of using the OFDM signals jointly as the communication and radar waveforms. Garmatyuk et al. analyzed the performance of a multi-carrier radar/communication system, based on ultra-wideband (UWB) waveform obtained using OFDM, for high-resolution synthetic aperture radar (SAR) imaging [32] – [34] and in the presence of in-band GPS signals [35]. Based on the OFDM architecture, they designed and built an experimental system that can be used interchangeably as a radar sensor and communication device without any hardware alterations [36], [37]. Van Genderen et al. also explored the principle of using OFDM-based multi-carrier signals in a radar plus communication system. They analyzed various aspects of an OFDM waveform in terms of Doppler tolerance [38] and wideband ambiguity function [39]; demonstrated the capability of Doppler sensitive OFDM signal to reduce Doppler ambiguity [40], [41]; studied the relation between the Doppler sidelobes and peak-to-average power ratio (PAPR) of the OFDM signal [42], and employed Golay complementary sequences to reduce PAPR [43]. Donnett and Longstaff utilized the OFDM communication technique in coherent MIMO radar applications to distribute the processed data to remote users [44].

In addition, Paichard et al. developed a wideband OFDM radar prototype named HYCAM (Hyperfrequency Camera), to measure and analyze the RCS of time-varying targets [45]. Tran used the OFDM waveform in the detection problems and proposed the patterns for changing subcarriers to have low interference [46]. Van Caekenberghe et al. presented an OFDM frequency scanning radar (FSR) concept to reduce the cost and size of an autonomous landing guidance (ALG) system [47]. Stralka and Meyer exploited the multi-carrier nature of the OFDM signal to propose a novel



digital phased-array architecture [48]. Recently, Sebt et al. proposed a least-squared approach for the ambiguity function synthesis of an OFDM signal [49], and Strum et al. developed an OFDM symbol-based processing to obtain superior range profiles [50].

### 1.3 Our Contributions

In this research, we employ an OFDM radar for target detection and tracking problems and adaptively design the OFDM signal to improve the system performance. In the following, we present a brief summary of our contributions.

#### **Waveform Design to Improve Wideband Ambiguity Function**

We propose an adaptive OFDM waveform design algorithm to improve the radar's wideband ambiguity function (WAF) [51] – [53]. Here we emphasize that the received signal depends on the scattering parameters of the target. Hence, the corresponding WAF at the output of the matched filter must include the target responses along with delay and Doppler. This approach enables us to propose a waveform design technique that adapts to the target parameters. We design the spectrum of the OFDM signal such that the volume of the corresponding WAF best approximates the volume of a desired ambiguity function over a region in the delay-Doppler plane. The designed waveform yields a better auto-correlation function (ACF), which results in an improved delay (range) resolution for the radar system.

## Target Detection in Multipath Scenarios

We develop methods for detecting a moving target in the presence of multipath reflections, which exist, for example, in urban environments [54], [55]. The multipath propagations increase the spatial diversity of the radar system by providing extra “looks” at the target and thus enabling target detection and tracking even beyond the line-of-sight (LOS) [56], [57]. We take advantage of the multipath propagation by exploiting the multiple Doppler shifts that correspond to the projections of the target velocity on each of the multipath components. We develop a parametric measurement model based on the OFDM signalling technique under the generalized multivariate analysis of variance (GMANOVA) framework [58], [59], and employ the generalized likelihood ratio (GLR) tests to detect the presence of a target in a particular range cell [60, Ch. 6]. In addition, we design the OFDM signal for the next coherent processing interval to maximize the expression of the noncentrality parameter, and thus to improve detection performance.

## Waveform Design Based on Multi-Objective Optimization

Exploiting the sparsity of multiple paths and the knowledge of the environment, we first transform the target-detection problem into the task of estimating the spectrum of a sparse signal [61], [62]. We employ a collection of multiple small Dantzig selectors (DS) [63] to estimate the sparse vector. Then, we analytically evaluate the performance characteristics and show that our decomposed DS has advantages over the standard DS, both in terms of computation and performance.

Next, we propose a criterion to optimally design the spectral parameters of the OFDM signal based on the multi-objective optimization (MOO) approach [64] – [67]. We observe that if the signal parameters are designed to minimize the upper bound on the sparse-estimation error, then the resultant waveform depends solely on the properties of the measurement matrix. However, to achieve a better performance, it is also essential that the signal parameters adapt to the operational scenario involving dynamic target states and nonstationary environmental conditions. Hence, in addition to minimizing the upper bound on the estimation error, we propose maximizing another utility function based on the squared Mahalanobis-distance [68], [69], one that depends on the target and noise parameters. Based on these arguments, we develop a constrained MOO problem to simultaneously optimize two objective functions: minimizing the upper bound on the estimation error to improve the efficiency of sparse-recovery and maximizing the squared Mahalanobis-distance to increase the performance of the underlying detection problem. We apply the well-known non-dominated sorting genetic algorithm II (NSGA-II) [70] to obtain the Pareto-optimal solutions [64] of our MOO problem.

## **Target Tracking in Low-Grazing Angle Scenarios**

We develop methods to track a single target in low-grazing angle (LGA) scenarios [71] – [76]. We consider the effects of the earth’s curvature and of the linear refractivity gradient of the horizontally stratified atmosphere while modeling the specular multipath signals. The randomly reflected returns (clutter), which also depend on the transmitted signal, are statistically modeled as a compound-Gaussian process [77], [78]. We employ a co-located multiple-input multiple-output (MIMO) radar configuration [79]. Additionally, we use polarization-sensitive transceivers to resolve

the multipath signals with small separation angles [80], [81]. To track the target, we use a sequential Monte Carlo method (particle filter) [82] – [84]. However, in contrast to the conventional open-loop tracker, we integrate the tracking procedure with an information theoretic waveform design algorithm. We propose to design the spectral parameters of the OFDM signal for the next pulse interval by maximizing the mutual information [85] between the state and measurement vectors.

## **Multi-Target Tracking Using Delay-Doppler Sparsity**

We exploit the inherent sparsity of targets on the delay-Doppler plane to develop an efficient multi-target tracking procedure [86], [87]. In our model, the nonzero entries of the sparse vector, which correspond to the target scattering coefficients at different OFDM subcarriers, appear in clusters (blocks). Such vectors are referred to as block-sparse [88], [89]. Therefore, to maximize accuracy in the sparse-recovery, we design the spectrum of the OFDM signal for the minimum block-coherence measure [90] and prove that the maximum accuracy is attainable by transmitting equal amounts of energy over all the OFDM subcarriers. In the tracking filter, we exploit the same block-sparsity property in developing a block version of the compressive sampling matching pursuit (CoSaMP) algorithm [91]. For computational efficiency, instead of using all the possible delay-Doppler grids for every pulse interval, we dynamically partitioned a small portion of the delay-Doppler plane around the predicted state parameters at a particular pulse interval.

## 1.4 Outline of the Dissertation

The rest of the dissertation is organized as follows. In Chapter 2, we present an adaptive OFDM waveform design algorithm to improve the radar's wideband ambiguity function. In Chapter 3, we propose methods for detecting a moving target in the presence of multipath reflections and design the OFDM signal to improve the detection performance. We transform the target-detection problem into a sparse estimation task in Chapter 4. In this context, we optimally design the OFDM signals using the multi-objective optimization approach. Chapters 5 and 6, respectively, describe our work on the tracking algorithms of a single target in LGA scenarios and multiple targets using delay-Doppler sparsity. Finally, in Chapter 7, we summarize our contributions and discuss some possible future work.

# Chapter 2

## Waveform Design to Improve Wideband Ambiguity Function<sup>1</sup>

In this chapter, we consider a multi-frequency radar that employs an OFDM signal, and compute its wideband ambiguity function (WAF) [51], [52], including the effects of the target response on the received signal. The motivation for employing multiple frequencies is that the different scattering centers of a target resonate differently at each frequency, and this also allows us to demonstrate the effects of the target-response on the WAF. Moreover, the use of a multi-carrier OFDM signal improves the delay-resolution by a factor equal to the number of subcarriers [12], [16, Ch. 11]. In addition, we devise an optimization procedure to design the spectrum of the transmitting OFDM signal such that the volume of the corresponding WAF best approximates the volume of a desired ambiguity function. The adaptive OFDM signal yields a better auto-correlation function that results in an improved range resolution for the radar system.

---

<sup>1</sup>Based on S. Sen and A. Nehorai, “Adaptive design of OFDM radar signal with improved wideband ambiguity function,” *IEEE Trans. Signal Process.*, vol. 58, no. 2, pp. 928–933, Feb. 2010. ©[2010] IEEE.

## 2.1 Introduction

The ambiguity function for radar was originally introduced by Ville [92]; however, it is generally referred to as Woodward's ambiguity function because of his popular work [93], [94]. According to Woodward, an ambiguity function is defined as a two-dimensional correlation between the transmitted narrowband signal and its time-delayed (related to target range) and frequency-shifted (related to target velocity) received version. Several articles interpret the ambiguity function as a matched filter response [1, Ch. 6.4], [95, Ch. 4], [96, Ch. 5], whereas a few others as a two-dimensional point-spread function [97], [98].

In the ideal case, an ambiguity function looks like a two-dimensional Dirac-delta function (as shown in Fig. 2.1(a)), consisting of a single peak of infinitesimal thickness at the origin and zero everywhere else on the delay-Doppler plane. However, an ambiguity function of this kind is not practical, because it does not have any ambiguity in either delay or Doppler estimation and because it can resolve any two targets no matter how close they are in terms of range and Doppler. Fig. 2.1(b) depicts a reasonable approximated version, namely the thumbtack ambiguity function, that has a narrow mainlobe and a nonzero pedestal (or sidelobes).

The general formulation of the ambiguity function either does not include a scattering coefficient of the target in the received signal model, or it assumes identical values for the scattering coefficients corresponding to different directions and/or frequencies. Additionally, Woodward's version of the ambiguity function does not hold for large-bandwidth signals, such as the OFDM signals. Target movements result in either expansion or compression in time for the wideband transmitted signal, and this effect can no longer be approximated by a simple "shift" in frequency. Therefore, in this

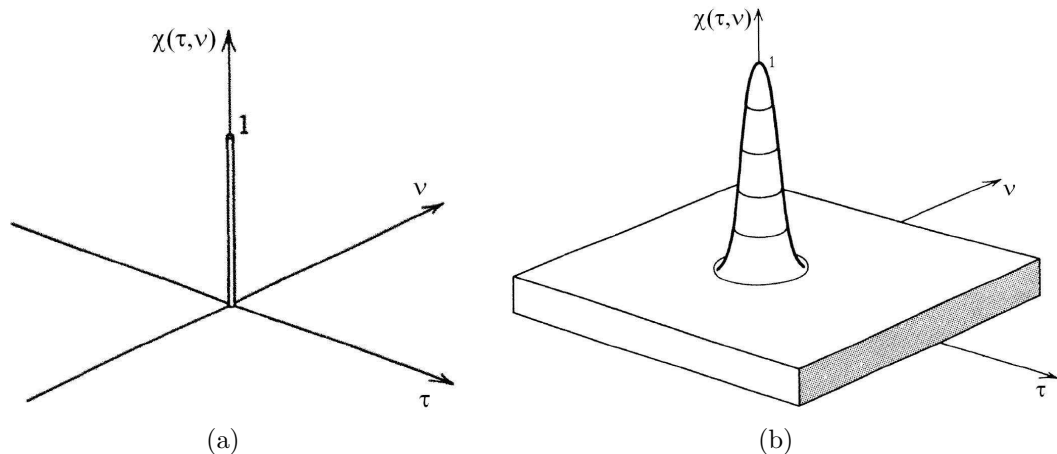


Figure 2.1: (a) Ideal and (b) thumbtack ambiguity functions.

work we follow the WAF introduced by Kelley-Wishner [51] and Speiser [52], but only after including the effect of different target responses at different frequencies. Different properties of the WAF, similar to those of its narrowband counterpart, can be found in [99] – [102].

## 2.2 Signal Model and Wideband Ambiguity Function

In this section, we first introduce the transmitted and received signal models of an OFDM signaling system. Along with the delay and Doppler effects, the received signal model also incorporates the scattering coefficients of the target at multiple frequencies. Then, we compute the expressions of WAF for a single pulse and a coherent pulse train.



### 2.2.1 Signal Model

We consider a monostatic radar employing an OFDM signaling system with  $L$  active subcarriers, a bandwidth of  $B$  Hz, and a pulse duration of  $T$  seconds. Let  $\mathbf{a} = [a_0, a_1, \dots, a_{L-1}]^T$  represent the complex weights transmitted over different subcarriers and satisfying  $\sum_{l=0}^{L-1} |a_l|^2 = 1$ . Then the complex envelope of a single pulse can be represented as

$$s(t) = \sum_{l=0}^{L-1} a_l \varphi_l(t) \quad \text{where } \varphi_l(t) = e^{j2\pi l\Delta f t}, \quad (2.1)$$

and  $\Delta f = B/(L+1) = 1/T$  denotes the subcarrier spacing. Let  $f_c$  be the carrier frequency of operation, the transmitted signal is given by

$$\tilde{s}(t) = 2 \operatorname{Re} \left\{ \sum_{l=0}^{L-1} a_l e^{j2\pi f_l t} \right\}, \quad (2.2)$$

where  $f_l = f_c + l\Delta f$  represents the  $l$ -th subcarrier frequency. Interchanging the real and summation operators, we can rewrite (2.2) as

$$\tilde{s}(t) = \sum_{l=0}^{L-1} \tilde{s}_l(t), \quad (2.3)$$

where

$$\tilde{s}_l(t) = 2 \operatorname{Re} \{ a_l e^{j2\pi f_l t} \} \quad (2.4)$$

represents the transmitted signal at the  $l$ -th subcarrier only.

Considering a far-field point target at distance  $r$  and relative velocity  $\mathbf{v}$  with respect to the radar, the received signal in a noise-free scenario can be written as

$$\tilde{y}_1(t) = \tilde{s}(\gamma(t - \tau)), \quad (2.5)$$

where  $\gamma = 1 + \beta$  accounts for the stretching or compressing in time of the reflected signal;  $\beta = (2/c)\langle \mathbf{u}, \mathbf{v} \rangle$  represents the Doppler spreading factor;  $\mathbf{u}$  is the unit DOA vector;  $\tau = 2r/c$  is the roundtrip delay between the radar and the target; and  $c$  is the speed of propagation. Substituting (2.2) into (2.5) we get

$$\begin{aligned} \tilde{y}_1(t) &= 2 \operatorname{Re} \left\{ \sum_{l=0}^{L-1} a_l e^{j 2\pi f_l \gamma (t-\tau)} \right\} \\ &= 2 \operatorname{Re} \left\{ \sum_{l=0}^{L-1} a_l e^{j 2\pi l \Delta f \gamma (t-\tau)} e^{j 2\pi f_c \gamma (t-\tau)} \right\} \\ &= 2 \operatorname{Re} \left\{ \sum_{l=0}^{L-1} a_l \phi_l(\gamma(t - \tau)) e^{-j 2\pi f_c \gamma \tau} e^{j 2\pi \nu t} e^{j 2\pi f_c t} \right\}, \end{aligned}$$

where  $\nu = f_c \beta$  represents the Doppler frequency. Hence, after demodulation the complex envelope of the received signal is

$$y_1(t) = \sum_{l=0}^{L-1} a_l \phi_l(\gamma(t - \tau)) e^{-j 2\pi f_c \gamma \tau} e^{j 2\pi \nu t}. \quad (2.6)$$

However, note that neither (2.5) nor (2.6) includes any parameter related to the target scattering coefficient. Therefore, denoting  $\mathbf{x} = [x_0, x_1, \dots, x_{L-1}]^T$  as a complex vector containing the scattering coefficients of the target at different subcarriers, we modify the expressions of the received signal as

$$\tilde{y}_2(t) = 2 \operatorname{Re} \left\{ \sum_{l=0}^{L-1} x_l a_l e^{j 2\pi f_l \gamma (t-\tau)} \right\}, \quad (2.7)$$

and the complex envelope as

$$y_2(t) = \sum_{l=0}^{L-1} x_l a_l \phi_l(\gamma(t - \tau)) e^{-j2\pi f_c \gamma \tau} e^{j2\pi \nu t}. \quad (2.8)$$

## 2.2.2 WAF of a Single Pulse

According to Kelley-Wishner [51], the wideband ambiguity function is defined as

$$\chi(\tau, \nu) \triangleq \sqrt{\gamma} \int_{-\infty}^{\infty} s_{\text{anl}}(t) s_{\text{anl}}^*(\gamma(t - \tau)) dt, \quad (2.9)$$

where  $s_{\text{anl}}(t)$  represents the analytic signal corresponding to  $s(t)$ . On the assumption that the complex envelope  $s(t)$  is perfectly bandlimited in comparison with the carrier frequency  $f_c$ , which is true for most radar signals [4], we can consider

$$s_{\text{anl}}(t) = s(t) e^{j2\pi f_c t}. \quad (2.10)$$

Therefore, (2.9) can be simplified to

$$\chi(\tau, \nu) = e^{j2\pi f_c \gamma \tau} \left[ \sqrt{\gamma} \int_{-\infty}^{\infty} s(t) s^*(\gamma(t - \tau)) e^{-j2\pi \nu t} dt \right]. \quad (2.11)$$

Sometimes the expression in (2.11) is referred to as the output of an optimum detector filter matched to zero delay and zero Doppler [98], with the term within the square bracket labeled only as the WAF [103]. Alternatively, in some other literature, the WAF is defined as the magnitude or magnitude-squared of the term within the square bracket in (2.11) [104].

Now, incorporating the effects of the target response in the received signal, we redefine the WAF at the output of the matched filter as

$$\begin{aligned}
& \chi_{\text{MF}}(\tau, \nu, \mathbf{a}, \mathbf{x}) \\
&= e^{j2\pi f_c \gamma \tau} \left[ \sqrt{\gamma} \int_{T_{\min}}^{T_{\max}} \left( \sum_{l_1=0}^{L-1} a_{l_1} \phi_{l_1}(t) \right) \left( \sum_{l_2=0}^{L-1} x_{l_2}^* a_{l_2}^* \phi_{l_2}^*(\gamma(t-\tau)) \right) e^{-j2\pi \nu t} dt \right], \\
&= \sum_{l_1=0}^{L-1} \sum_{l_2=0}^{L-1} a_{l_1} a_{l_2}^* x_{l_2}^* \chi_{\phi_{l_1} \phi_{l_2}}(\tau, \nu), \tag{2.12}
\end{aligned}$$

where

$$T_{\min} = \max(0, \tau), \quad T_{\max} = \min(T, T/\gamma + \tau),$$

and

$$\chi_{\phi_{l_1} \phi_{l_2}}(\tau, \nu) = e^{j2\pi f_c \gamma \tau} \left[ \sqrt{\gamma} \int_{T_{\min}}^{T_{\max}} \phi_{l_1}(t) \phi_{l_2}^*(\gamma(t-\tau)) e^{-j2\pi \nu t} dt \right] \tag{2.13}$$

denotes the cross-ambiguity function between  $\phi_{l_1}(t)$  and  $\phi_{l_2}(t)$ , having a similar form as (2.11). Note that in (2.12), we explicitly parametrize  $\chi_{\text{MF}}(\cdot)$  in terms of  $\mathbf{x}$  to emphasize that it depends on the scattering coefficients of the target. In addition,  $\chi_{\text{MF}}(\cdot)$  also depends on  $\mathbf{a}$ . This parametrization is realistic and also enables us to adaptively design the spectrum of the transmitted OFDM signal to improve the corresponding ambiguity profile, which will be discussed in Section 2.3. Using the definitions of  $f_l$ ,  $T_{\min}$ ,  $T_{\max}$ , and the following integration result

$$\int_{T_{\min}}^{T_{\max}} e^{-j2\pi f t} dt = T_{\text{diff}} \text{sinc}(f T_{\text{diff}}) e^{-j2\pi f T_{\text{avg}}}, \tag{2.14}$$

where

$$T_{\text{diff}} = T_{\text{max}} - T_{\text{min}}, \quad T_{\text{avg}} = \frac{T_{\text{max}} + T_{\text{min}}}{2}.$$

we can further simplify (2.12) to

$$\chi_{\text{MF}}(\tau, \nu, \mathbf{a}, \mathbf{x}) = \chi_{\text{MF}}^{(\text{ml})}(\tau, \nu, \mathbf{a}, \mathbf{x}) + \chi_{\text{MF}}^{(\text{sl})}(\tau, \nu, \mathbf{a}, \mathbf{x}), \quad (2.15)$$

and

$$\begin{aligned} \chi_{\text{MF}}^{(\text{ml})}(\tau, \nu, \mathbf{a}, \mathbf{x}) &\triangleq \sqrt{\gamma} T_{\text{diff}} \sum_{l=0}^{L-1} x_l^* |a_l|^2 \text{sinc}[f_l \beta T_{\text{diff}}] e^{j2\pi[f_l \gamma \tau - \beta f_l T_{\text{avg}}]}, \\ \chi_{\text{MF}}^{(\text{sl})}(\tau, \nu, \mathbf{a}, \mathbf{x}) &\triangleq \sqrt{\gamma} T_{\text{diff}} \sum_{l_1=0}^{L-1} \sum_{\substack{l_2=0 \\ l_2 \neq l_1}}^{L-1} x_{l_2}^* a_{l_1} a_{l_2}^* \text{sinc}[\{f_{l_2} \beta + (l_2 - l_1) \Delta f\} T_{\text{diff}}] \\ &\quad \cdot e^{j2\pi[f_{l_2} \gamma \tau - \{ \beta f_{l_2} + (l_2 - l_1) \Delta f \} T_{\text{avg}}]}. \end{aligned}$$

If we plot separately we can see that  $\chi_{\text{MF}}^{(\text{ml})}(\cdot)$  produces the mainlobe of the WAF, while  $\chi_{\text{MF}}^{(\text{sl})}(\cdot)$  produces the sidelobes.

*Special Case:* For a conventional radar employing a single carrier frequency  $f_c$ , (2.15) can be simplified to

$$\chi_{\text{MF}}(\tau, \nu, \mathbf{a}, \mathbf{x}) = \sqrt{\gamma} T_{\text{diff}} x^* |a|^2 \text{sinc}[f_c \beta T_{\text{diff}}] e^{j2\pi f_c (\gamma \tau - \beta T_{\text{avg}})},$$

and therefore, the expression of the normalized WAF,

$$\frac{\chi_{\text{MF}}(\tau, \nu, \mathbf{a}, \mathbf{x})}{\chi_{\text{MF}}(0, 0, \mathbf{a}, \mathbf{x})} = \frac{T_{\text{diff}}}{T_{\text{diff}}^{(0)}} \text{sinc}(\nu T_{\text{diff}}) e^{-j2\pi \nu T_{\text{avg}}}, \quad (2.16)$$

does not depend on the scattering coefficients of the target. Here  $T_{\text{diff}}^{(0)}$  is  $T_{\text{diff}}$  evaluated at  $\tau = 0$ .

### 2.2.3 WAF of a Pulse Train

The Doppler-resolution of the ambiguity function is improved when we transmit a coherent pulse train. The complex envelope of a train of  $N$  identical pulses can be described as

$$s_N(t) = \sum_{n=0}^{N-1} s(t - nT_p), \quad (2.17)$$

where  $T_p$  is the pulse repetition interval (PRI). Then, the transmitted signal is given by

$$\tilde{s}_N(t) = 2 \operatorname{Re} \left\{ s_N(t) e^{j2\pi f_c t} \right\} = 2 \operatorname{Re} \left\{ \sum_{n=0}^{N-1} s(t - nT_p) e^{j2\pi f_c t} \right\}. \quad (2.18)$$

Using the expression of the analytic signal corresponding to  $\tilde{s}_N(t)$  in (2.9), we can formulate the WAF of a coherent pulse train as follows:

$$\begin{aligned} \chi_N(\tau, \nu) &= \sqrt{\gamma} \int_{-\infty}^{\infty} \left[ \sum_{n_1=0}^{N-1} s(t - n_1 T_p) e^{j2\pi f_c t} \right] \left[ \sum_{n_2=0}^{N-1} s^*(\gamma(t - \tau) - n_2 T_p) e^{-j2\pi f_c \gamma(t - \tau)} \right] dt \\ &= \sum_{n_1=0}^{N-1} \sum_{n_2=0}^{N-1} \chi \left( \tau + \left( \frac{n_2}{\gamma} - n_1 \right) T_p, \nu \right) e^{-j2\pi f_c (n_2 - n_1) T_p}, \end{aligned} \quad (2.19)$$

where  $\chi(\cdot)$  is the WAF of a single pulse as defined in (2.11). See Appendix A for the derivation of (2.19).

Following a similar type of derivation, including the effects of the target response in the received signal, we can modify the expression of WAF for a coherent pulse train as

$$\begin{aligned}
& \chi_{\text{MF}_N}(\tau, \nu, \mathbf{a}, \mathbf{x}) \\
&= \sum_{n_1=0}^{N-1} \sum_{n_2=0}^{N-1} \chi_{\text{MF}}\left(\tau + \left(\frac{n_2}{\gamma} - n_1\right) T_P, \nu, \mathbf{a}, \mathbf{x}\right) e^{-j2\pi f_c(n_2-n_1)T_P}, \\
&= \sum_{n_1=0}^{N-1} \sum_{n_2=0}^{N-1} \left[ \sum_{l_1=0}^{L-1} \sum_{l_2=0}^{L-1} a_{l_1} a_{l_2}^* x_{l_2}^* \chi_{\phi_{l_1}\phi_{l_2}}\left(\tau + \left(\frac{n_2}{\gamma} - n_1\right) T_P, \nu\right) \right] e^{-j2\pi f_c(n_2-n_1)T_P}, \\
&= \sum_{l_1=0}^{L-1} \sum_{l_2=0}^{L-1} a_{l_1} a_{l_2}^* x_{l_2}^* \chi_{\phi_{l_1}\phi_{l_2N}}(\tau, \nu), \tag{2.20}
\end{aligned}$$

where

$$\chi_{\phi_{l_1}\phi_{l_2N}}(\tau, \nu) = \sum_{n_1=0}^{N-1} \sum_{n_2=0}^{N-1} \chi_{\phi_{l_1}\phi_{l_2}}\left(\tau + \left(\frac{n_2}{\gamma} - n_1\right) T_P, \nu\right) e^{-j2\pi f_c(n_2-n_1)T_P} \tag{2.21}$$

denotes the cross-ambiguity function between two coherent pulse trains of  $\phi_{l_1}(t)$  and  $\phi_{l_2}(t)$ . In the rest of the chapter, we will consider the magnitude squared of (2.20),  $|\chi_{\text{MF}_N}(\cdot)|^2$ , as the expression of WAF.

## 2.3 Adaptive Waveform Design

In this section, we describe an optimization approach to adaptively design the spectrum of an OFDM signal such that the volume of the corresponding WAF best approximates the volume of a desired ambiguity profile.

The problem of synthesizing a waveform to satisfy a desired ambiguity function has been addressed extensively over the years [49], [105] – [111]. Wilcox [105] and Sussman [106] approach this problem to approximate the desired ambiguity profile in the least-squared (LS) sense. Their optimization procedure stretches over the entire  $(\tau, \nu)$  plane, and hence the resultant waveform can produce an “all-purpose” ambiguity function that would be more or less suitable for any radar application [106]. However, in many situations, it is not necessary to have a certain ambiguity shape for all values of  $\tau$  and  $\nu$ . Recently, Gladkova et al. [110], [111] extended Wilcox’s LS approach, restricting the optimization procedure over some limited subregions in the  $(\tau, \nu)$  plane, particularly surrounding the mainlobe.

We seek to find an OFDM waveform, satisfying  $\sum_{l=0}^{L-1} |a_l|^2 = 1$ , such that the error between the volumes of the resulting WAF and a desired ambiguity function is minimized. Instead of covering the entire  $(\tau, \nu)$  plane, we also limit the volume computations over a subregion,  $\mathcal{R}$ , containing the origin. Denoting the desired ambiguity function as  $\chi_{\text{opt}}(\tau, \nu)$ , we can state the optimization problem as follows:

$$\begin{aligned} \mathbf{a}_{\text{opt}}(\mathbf{x}) &= \arg \min_{\mathbf{a} \in \mathbb{C}^L} \int_{\mathcal{R}} \left| |\chi_{\text{opt}}(\tau, \nu)|^2 - |\chi_{\text{MF}_N}(\tau, \nu, \mathbf{a}, \mathbf{x})|^2 \right| d\tau d\nu, \quad (2.22) \\ &\text{subject to } \sum_{l=0}^{L-1} |a_l|^2 = 1 \text{ and } |a_l|^2 > \epsilon \forall l, \end{aligned}$$

where  $\epsilon$  is a small positive quantity (close to zero) ensuring transmission over all  $L$  frequency channels. We use numerical methods to solve for the optimized variables,  $\mathbf{a}_{\text{opt}}$ , that depend on the scattering coefficients of the target and hence comply with the philosophy of “adaptive” design.



In some particular cases, when  $|\chi_{\text{opt}}(\cdot)|^2 < |\chi_{\text{MF}_N}(\cdot)|^2$  holds true over the entire subregion  $\mathcal{R}$  (e.g.,  $\chi_{\text{opt}}(\tau, \nu) = \delta(\tau, \nu)$ ), we can further simplify (2.22) to the following:

$$\begin{aligned} \mathbf{a}_{\text{opt}}(\mathbf{x}) &= \arg \min_{\mathbf{a} \in \mathbb{C}^L} \int_{\mathcal{R}} \left| \chi_{\text{MF}_N}(\tau, \nu, \mathbf{a}, \mathbf{x}) \right|^2 d\tau d\nu, \\ &= \arg \min_{\mathbf{a} \in \mathbb{C}^L} \sum_{l_1, l_2, l_3, l_4} a_{l_1} a_{l_2}^* a_{l_3}^* a_{l_4} x_{l_2}^* x_{l_4} \int_{\mathcal{R}} \chi_{\phi_{l_1} \phi_{l_2 N}}(\tau, \nu) \chi_{\phi_{l_3} \phi_{l_4 N}}^*(\tau, \nu) d\tau d\nu. \end{aligned}$$

Hence, this expression leads to a minimization procedure that has a fourth-order form similar to that presented in [111], but it incorporates the target-scattering coefficients. However, from a mathematical perspective, our method can be categorized as an  $\ell_1$ -minimization, while that of [111] is an  $\ell_2$ -minimization.

The convergence time of (2.22) strongly depends on the area of subregion  $\mathcal{R}$  and the shape of the desired ambiguity function  $\chi_{\text{opt}}(\tau, \nu)$ . If the knowledge of the target response is known a priori, we can use an offline computation of (2.22) extending over a larger area of  $\mathcal{R}$  and considering an impulse-shaped  $\chi_{\text{opt}}(\cdot)$ . In real-time processing, when we need to compute  $\mathbf{a}_{\text{opt}}$  based on the estimated value of  $\mathbf{x}$  from the previous radar dwell, it would be practical to restrict  $\mathcal{R}$  to a smaller region (e.g.,  $|\tau| \leq T, |\nu| \leq 1/(2T_p)$ ) and not to choose an “idealistic” shape of  $\chi_{\text{opt}}(\cdot)$ .

## 2.4 Numerical Results

We present simulation results to demonstrate an improved ambiguity profile due to the adaptive waveform design. We considered an OFDM radar operating with the following specifications: carrier frequency  $f_c = 1$  GHz; available bandwidth  $B = 125$  MHz; number of subcarriers  $L = 4$ ; subcarrier spacing  $\Delta f = B/(L + 1) = 25$  MHz;

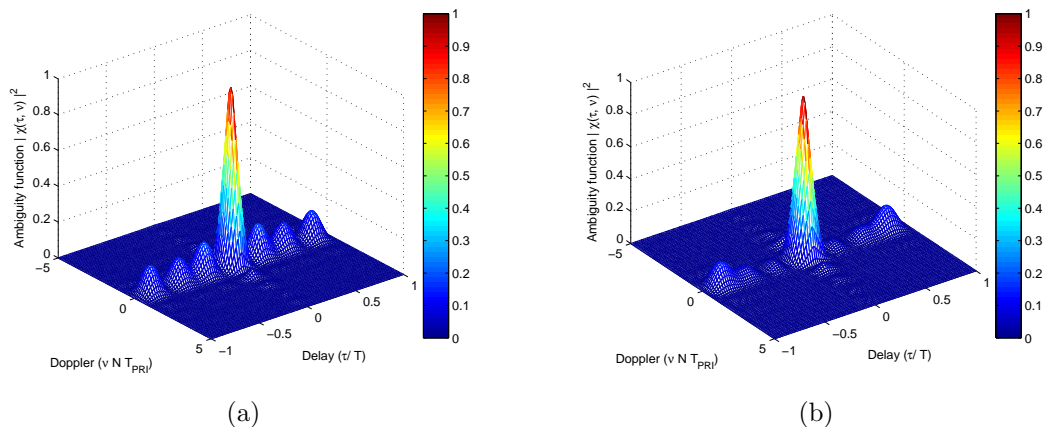


Figure 2.2: Plots of wideband ambiguity functions for (a) fixed and (b) adaptive waveforms over a region  $\mathcal{R} = \{|\tau| \leq T, |\nu| \leq 1/(2T_{\text{PRI}})\}$ .

pulse width  $T = 1/\Delta f = 40$  ns; pulse repetition interval  $T_p = 20$   $\mu$ s; and number of coherent pulses  $N = 10$ . To evaluate  $\mathbf{a}_{\text{opt}}$ , we used  $\mathcal{R} := \{|\tau| \leq T, |\nu| \leq 1/(2T_p)\}$  and an impulse-like  $\chi_{\text{opt}}(\tau, \nu)$  that has value 1 at the origin but zero everywhere else. We realized the entries of  $\mathbf{x}$  from a  $\mathcal{N}(0, 1)$  distribution. The results presented in Figs. 2.2 and 2.3 were obtained using the numerical optimization solver of MATLAB after averaging over 50 such independent realizations of  $\mathbf{x}$ . We compared this adaptively designed WAF with that obtained from a fixed waveform that employs  $a_l = 1/\sqrt{L} \forall l$ .

Fig. 2.2(b) depicts the WAF obtained from the optimized waveform following (2.22). This ambiguity function shows a considerable improvement compared to the one shown in Fig. 2.2(a), which was obtained from a fixed waveform. Numerically, the normalized volume under the ambiguity profile reduced from unity to 0.806. The zero-delay and zero-Doppler cut plots of these ambiguity profiles are shown in Fig. 2.3. From Fig. 2.3(a) it is quite evident that the adaptive waveform resulted in a much better auto-correlation function. The first sidelobe level of the ambiguity function

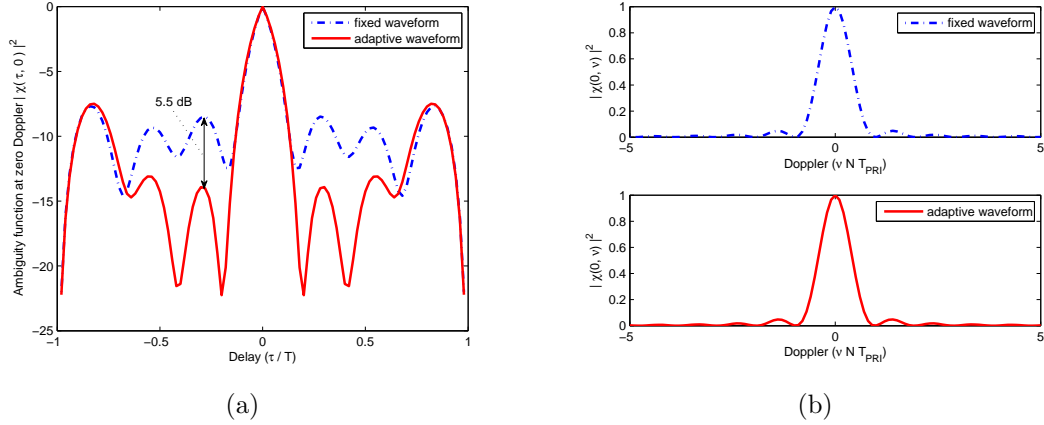


Figure 2.3: (a) Zero-Doppler cuts (auto-correlation functions) and (b) zero-delay cuts of the wideband ambiguity functions corresponding to the adaptive and fixed waveforms.

corresponding to the adaptive waveform is 5.5 dB down with respect to that of its counterpart for fixed waveform. The zero-delay cut plots in Fig. 2.3(b) suggest that there is no change in the Doppler resolution, as we expect, due to our adaptive waveform design.

For further insight into the optimization procedure, we looked into the energy distributions of the OFDM waveform and target response over different subcarriers both before and after the optimization. For example, as shown in Fig. 2.4, in a particular sample run we had  $|x_l| = \{6.42, 1.03, 4.23, 5.66\}$ , and the optimization algorithm (2.22) resulted in  $|a_l| = \{0.24, 0.80, 0.42, 0.29\}$  when initialized with  $a_l = 1/\sqrt{L} = 0.50 \forall l$ . Hence, we noticed that the sample variance of  $|a_l x_l|$  reduces from 1.06 to 0.13; i.e., the redistribution energy occurs with more signal energy to the subcarrier whose target response is weaker and with less signal energy to the subcarrier whose target response is already stronger.

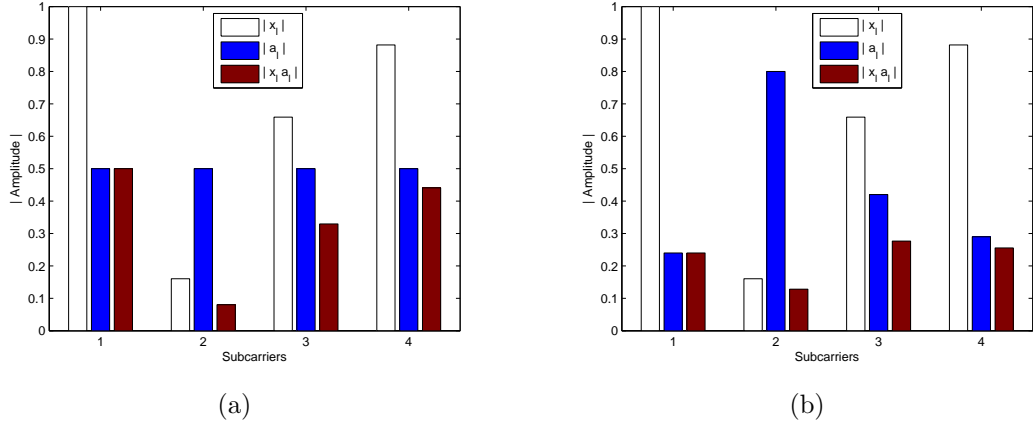


Figure 2.4: Distributions of signal energy and target response over different OFDM subcarriers (a) before and (b) after the optimization process.

## 2.5 Summary

We proposed an optimization algorithm to compute an adaptive OFDM radar waveform such that the volume of the corresponding wideband ambiguity function best approximates the volume of a desired ambiguity function over a region in the delay-Doppler plane. We emphasized that the expression of the wideband ambiguity function at the output of a matched filter must include the target response along with delay and Doppler. We numerically demonstrated the advantage of adaptive waveform design in obtaining much better auto-correlation function. This further motivates us to use adaptive OFDM waveform for specific radar problems, such as the detection and tracking of targets, which are described in the following chapters.

# Chapter 3

## Target Detection in Multipath Scenarios<sup>2</sup>

In this chapter, we develop methods for detecting a moving target in the presence of multipath reflections, particularly in urban environments. We take advantage of the multipath propagation that increases the spatial diversity of the radar system and provides different Doppler shifts over different paths. First, we develop an OFDM radar measurement model accounting for only a finite number of specularly reflected multipath signals. We formulate the detection problem as a statistical hypothesis test to decide about the presence of a moving target in a particular range cell. Then, we propose an algorithm to optimally design the spectral parameters of the OFDM transmitting waveform for the next coherent processing interval. In addition, we extend our models to consider the aspects of temporal correlations in the measurement noise.

---

<sup>2</sup>Based on S. Sen and A. Nehorai, “Adaptive OFDM radar for target detection in multipath scenarios,” *IEEE Trans. Signal Process.*, vol. 59, no. 1, pp. 78-90, Jan. 2011. ©[2010] IEEE.

## 3.1 Introduction

The problem of target-detection in multipath scenarios is becoming increasingly relevant and challenging to radar technologies. The multipath propagations increase the spatial diversity of the radar system by providing extra “looks” at the target and thus enabling target detection and tracking even beyond the LOS [56], [57] (see Fig. 3.1). We take advantage of the multipath propagation by exploiting multiple Doppler shifts corresponding to the projections of the target velocity on each of the multipath components. To resolve and exploit the multipath components, short pulse, multi-carrier wideband radar signals are commonly used. We consider the OFDM signalling scheme, which is one of the ways to accomplish the simultaneous use of several subcarriers. The use of an OFDM signal mitigates the possible fading, resolves the multipath reflections, and provides additional frequency diversity as different scattering centers of a target resonate at different frequencies.

First, we discuss a detection problem in which the radar has complete knowledge of the first-order (or single bounce) specularly reflected multipath signals. We assume that the clutter and measurement noise are temporally white. We develop the measurement model under the generalized multivariate analysis of variance (GMANOVA) framework [58], [59], to account for the different multipath components as well as for multiple Doppler shifts. We formulate the detection problem as a hypothesis test to decide about the presence of a target in a particular range cell. Due to the lack of knowledge of all the parameters in our models, we employ the generalized likelihood ratio (GLR) test [60, Ch. 6]. We present numerical results to evaluate the performance of these proposed detectors, as we do not have any analytical expressions to evaluate their performances.

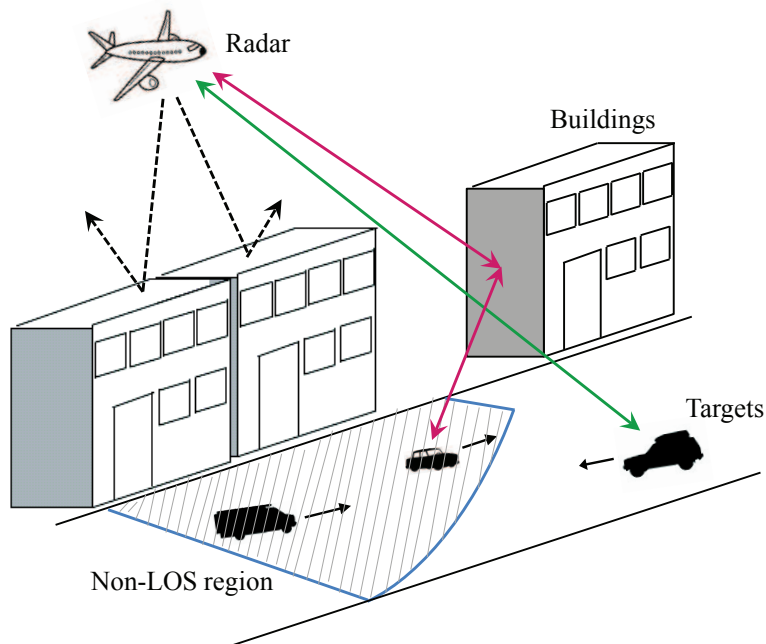


Figure 3.1: The exploitation of multipath propagations increases the spatial diversity.

Next, we propose a criterion to adaptively compute the spectral parameters of the next transmitting OFDM waveform. To construct such a criterion, we first look into the performance characteristics of the GLR test statistics, assuming that the target velocity is known. However, this analysis does not characterize the performance of our detectors, in which the target velocity is unknown. Our analysis with known target velocity shows that the GLR test asymptotically (i.e., with a large number of temporal samples) results in constant false alarm rate (CFAR) detectors, and the detection performances depend on the system parameters through the corresponding noncentrality parameters of the distributions under the alternate hypothesis. This implies that it is possible to improve the detection performance by maximizing the noncentrality parameter. We apply this idea to our problem and formulate the optimization algorithm to select the parameters of the next transmitting waveform by maximizing the same expression of the noncentrality parameter subject to a fixed

transmission-energy constraint. We show that the solution of this optimization problem results in an eigenvector corresponding to the largest eigenvalue of a matrix that depends on the target, clutter, and noise parameters.

Later in the chapter, we relax the assumption of temporal whiteness to study the effects of temporally correlated measurement noise processes on our models. Temporal correlations exist in certain radar applications, in particular at high pulse repetition frequencies (PRF) [112], [113]. To model the temporal correlation matrix, we look into a branch of statistics known as the nearest neighbor analysis [114], [115], and present the consequent detection tests.

## 3.2 Problem Description and Modeling

We consider a far-field point target moving with a constant relative velocity  $\mathbf{v}$ , with respect to the radar, in a multipath-rich environment. At the operating frequency, we assume that the reflecting surfaces produce only specular reflections of the radar signal. We assume that the radar has complete knowledge of the environment under surveillance. Hence, for every range cell the radar knows the number of possible multipaths ( $P$ ) between the radar and target and the DOA unit-vectors ( $\mathbf{u}_p$ ,  $p = 0, 1, \dots, P - 1$ ) along each such path.

Under this scenario, we first introduce the parametric measurement model for the OFDM signalling technique. Then, we discuss our statistical assumptions on clutter and noise.



### 3.2.1 Measurement Model

We consider an OFDM signalling system with  $\mathbf{a} = [a_0, a_1, \dots, a_{L-1}]^T$  representing the complex transmit-weights over the  $L$  subcarriers, as previously described in (2.1) – (2.4). Then, the received signal along the  $p$ -th path (represented by the DOA vector  $\mathbf{u}_p$ ) due to the transmission of only the  $l$ -th subcarrier can be written as

$$\tilde{y}_{lp}(t) = x_{lp} \tilde{s}_l(\gamma_p(t - \tau_p)) + \tilde{e}_{lp}(t), \quad (3.1)$$

where  $x_{lp}$  is a complex quantity representing the scattering coefficient of the target along the  $l$ -th subchannel and  $p$ -th path;  $\gamma_p = 1 + \beta_p$ , where  $\beta_p = 2\langle \mathbf{v}, \mathbf{u}_p \rangle / c$  is the relative Doppler shift along the  $p$ -th path, and  $c$  is the speed of propagation;  $\tau_p$  is the roundtrip delay between the radar and target along the  $p$ -th path; and  $\tilde{e}_{lp}$  represents the clutter and measurement noise along the  $l$ -th subchannel and  $p$ -th path. Therefore, the received signal over all  $P$  available paths due to the transmission of an  $L$ -carrier OFDM signal is given by

$$\begin{aligned} \tilde{y}(t) &= \sum_{l=0}^{L-1} \sum_{p=0}^{P-1} \tilde{y}_{lp}(t) = 2 \operatorname{Re} \left\{ \sum_{l=0}^{L-1} \sum_{p=0}^{P-1} a_l x_{lp} e^{j 2\pi f_l \gamma_p (t - \tau_p)} \right\} + \tilde{e}(t), \\ &= 2 \operatorname{Re} \left\{ \sum_{l=0}^{L-1} \sum_{p=0}^{P-1} a_l x_{lp} e^{j 2\pi f_l (1 + \beta_p) (t - \tau_p)} \right\} + \tilde{e}(t), \\ &= 2 \operatorname{Re} \left\{ \sum_{l=0}^{L-1} \sum_{p=0}^{P-1} a_l x_{lp} e^{-j 2\pi f_l (1 + \beta_p) \tau_p} e^{j 2\pi f_l \beta_p t} e^{j 2\pi f_l t} \right\} + \tilde{e}(t), \end{aligned} \quad (3.2)$$

and hence the corresponding complex envelope at the output of the  $l$ -th subchannel is given as

$$y_l(t) = \sum_{p=0}^{P-1} a_l x_{lp} e^{-j 2\pi f_l (1 + \beta_p) \tau_p} e^{j 2\pi f_l \beta_p t} + e_l(t). \quad (3.3)$$

Let us assume at this point that the relative time gaps between any two multipath signals are very small in comparison to the actual roundtrip delays, i.e.,  $\tau_p \approx \tau_0$  for  $p = 0, 1, \dots, P - 1$ . These assumptions can be justified in systems where the path lengths of multipath arrivals differ little (e.g., a narrow urban canyon where the range is much greater than the width). Further, let us denote  $\tau_0$  as the roundtrip delay corresponding to the range cell under consideration. Then, the information of the roundtrip delays are incorporated into (3.3) by substituting  $t = \tau_0 + nT_p, n = 0, 1, \dots, N - 1$ , where  $T_p$  is the PRI and  $N$  is the number of temporal measurements within a given coherent processing interval (CPI). Hence, corresponding to a specific range cell containing the target, the complex envelope of the received signal at the output of the  $l$ -th subchannel is

$$y_l(n) = \sum_{p=0}^{P-1} a_l x_{lp} \phi_{lp}(n, \mathbf{v}) + e_l(n), \quad \text{for } l = 0, 1, \dots, L - 1, \quad n = 0, 1, \dots, N - 1, \quad (3.4)$$

where

$$\phi_{lp}(n, \mathbf{v}) \triangleq e^{-j2\pi f_l \tau_0} e^{j2\pi f_l \beta_p n T_p}. \quad (3.5)$$

Stacking the measurements of all  $L$  subchannels into one column vector of length  $L$ , we get

$$\mathbf{y}(n) = \mathbf{A} \mathbf{X} \boldsymbol{\phi}(n, \mathbf{v}) + \mathbf{e}(n), \quad \text{for } n = 0, 1, \dots, N - 1, \quad (3.6)$$

where

$$\bullet \quad \mathbf{y}(n) = [y_0(n), y_1(n), \dots, y_{L-1}(n)]^T.$$

- $\mathbf{A} = \text{diag}(\mathbf{a})$  is an  $L \times L$  complex diagonal matrix that contains the transmitted weights  $\mathbf{a}$ .
- $\mathbf{X} = \text{blkdiag}(\mathbf{x}_0^T, \mathbf{x}_1^T, \dots, \mathbf{x}_{L-1}^T)$  is an  $L \times LP$  complex rectangular block-diagonal matrix where each nonzero block  $\mathbf{x}_l = [x_{l0}, x_{l1}, \dots, x_{lP-1}]^T$ ,  $l = 0, 1, \dots, L-1$ , represents the scattering coefficients of the target at the  $l$ -th subchannel over all  $P$  multipath.
- $\boldsymbol{\phi}(n, \mathbf{v}) = [\boldsymbol{\phi}_0(n, \mathbf{v})^T, \boldsymbol{\phi}_1(n, \mathbf{v})^T, \dots, \boldsymbol{\phi}_{L-1}(n, \mathbf{v})^T]^T$  is an  $LP \times 1$  complex vector where  $\boldsymbol{\phi}_l(n, \mathbf{v}) = [\phi_{l0}(n, \mathbf{v}), \phi_{l1}(n, \mathbf{v}), \dots, \phi_{lP-1}(n, \mathbf{v})]^T$ ,  $l = 0, 1, \dots, L-1$ , contains the Doppler information of the target at the  $l$ -th subchannel over all  $P$  multipath.
- $\mathbf{e}(n) = [e_0(n), e_1(n), \dots, e_{L-1}(n)]^T$  is an  $L \times 1$  vector of clutter returns, measurement noise, and co-channel interference.

Then, concatenating all the temporal data columnwise into an  $L \times N$  matrix, we obtain the OFDM measurement model as

$$\mathbf{Y} = \mathbf{A} \mathbf{X} \boldsymbol{\Phi}(\mathbf{v}) + \mathbf{E}, \quad (3.7)$$

where

- $\mathbf{Y} = [\mathbf{y}(0) \ \mathbf{y}(1) \ \dots \ \mathbf{y}(N-1)]$ .
- $\boldsymbol{\Phi}(\mathbf{v}) = [\boldsymbol{\phi}(0, \mathbf{v}) \ \boldsymbol{\phi}(1, \mathbf{v}) \ \dots \ \boldsymbol{\phi}(N-1, \mathbf{v})]$  is an  $LP \times N$  matrix containing the Doppler information of the target through the parameter  $\mathbf{v}$ .
- $\mathbf{E} = [\mathbf{e}(0) \ \mathbf{e}(1) \ \dots \ \mathbf{e}(N-1)]$  is an  $L \times N$  matrix comprising clutter returns, noise, and interference.

### 3.2.2 Statistical Assumptions

In this problem, any undesired reflections from the environment surrounding and/or behind the target, or any random multipath reflections from irregularities on a reflecting surface (e.g., windows and balconies) that cannot be modeled as specular components may contribute to the clutter. Therefore, we assume that the clutter and noise are temporally white and circularly symmetric zero-mean complex Gaussian process with unknown covariances. In (3.6), the noise vector  $\mathbf{e}(n)$  contains the clutter returns, noise, and co-channel interference at the output of  $L$  subchannels, which we assume to be correlated with an unknown positive definite covariance matrix  $\mathbf{\Sigma}$ . Hence, the OFDM measurements are distributed as

$$\mathbf{Y} \sim \mathbb{CN}_{L,N}(\mathbf{A} \mathbf{X} \Phi(\mathbf{v}), \mathbf{I}_N \otimes \mathbf{\Sigma}). \quad (3.8)$$

In this formulation, when the parameter  $\mathbf{v}$  is known, (3.7) complies with the GMANOVA structure [58], [116], which has been studied extensively in statistics and applied to a number of applications in signal processing [59].

## 3.3 Detection Test

In this section, we develop statistical detection tests for the OFDM measurement model presented in the previous section. Our goal is to decide whether a target is present or not in the range cell under consideration.

We construct the decision problem to choose between two possible hypotheses: the null hypothesis  $\mathcal{H}_0$  (target-free hypothesis) or the alternate hypothesis  $\mathcal{H}_1$  (target-present

hypothesis). The test can be expressed as

$$\begin{cases} \mathcal{H}_0 : \mathbf{X} = \mathbf{0}, \quad \Sigma \text{ unknown} \\ \mathcal{H}_1 : \mathbf{X} \neq \mathbf{0}, \quad \mathbf{v}, \Sigma \text{ unknown} \end{cases}. \quad (3.9)$$

Because of the lack of knowledge about  $\mathbf{v}$  and  $\Sigma$  we use the generalized likelihood ratio test [60, Ch. 6] in which the unknown parameters are replaced with their maximum likelihood estimates (MLE). This approach also provides the information about the unknown parameters since the first step is to find the MLEs.

Assuming that the parameter  $\mathbf{v}$  is known in (3.7), the GLR test for (3.9) compares the ratio of the likelihood functions under the two hypotheses with a threshold as follows [60, Ch. 6.4.2]:

$$\text{GLR}(\mathbf{v}) = \frac{f_{\mathcal{H}_1}(\mathbf{Y}; \mathbf{v}, \widehat{\mathbf{X}}, \widehat{\Sigma}_1)}{f_{\mathcal{H}_0}(\mathbf{Y}; \widehat{\Sigma}_0)} \underset{\mathcal{H}_1}{>} \underset{\mathcal{H}_0}{<} \gamma, \quad (3.10)$$

where  $f_{\mathcal{H}_0}$  and  $f_{\mathcal{H}_1}$  are the likelihood functions under  $\mathcal{H}_0$  and  $\mathcal{H}_1$ , respectively;  $\widehat{\Sigma}_0$  and  $\widehat{\Sigma}_1$  are the MLEs of  $\Sigma$  under  $\mathcal{H}_0$  and  $\mathcal{H}_1$ , respectively;  $\widehat{\mathbf{X}}$  is the MLE of  $\mathbf{X}$  under  $\mathcal{H}_1$ ; and  $\gamma$  is the detection threshold. After some algebraic manipulations, it can be shown that the test statistic of this problem is [59]

$$\text{GLR}(\mathbf{v}) = \frac{|\widehat{\Sigma}_0|}{|\widehat{\Sigma}_1|} = \frac{|(1/N)\mathbf{Y}\mathbf{Y}^H|}{\left| (1/N) \left( \mathbf{Y} - \mathbf{A} \widehat{\mathbf{X}} \Phi(\mathbf{v}) \right) \left( \mathbf{Y} - \mathbf{A} \widehat{\mathbf{X}} \Phi(\mathbf{v}) \right)^H \right|}. \quad (3.11)$$

However, having a block-diagonal structure, the scattering matrix  $\mathbf{X}$  does not yield a closed-form MLE expression [117]. So, in this work, we use an approximate ML

(AML) estimator for  $\mathbf{X}$ , defined as [117, Eqn. 28]

$$\hat{\mathbf{x}}_{\text{AML}} \triangleq \text{vecb}(\widehat{\mathbf{X}}) = (\mathbf{\Gamma}^H \mathbf{\Gamma})^{-1} \mathbf{\Gamma}^H \text{vec} \left( \mathbf{G}^{-\frac{1}{2}} \mathbf{Y} \mathbf{\Pi}_{\Phi} \right), \quad (3.12)$$

where

$$\mathbf{\Gamma} \triangleq \begin{bmatrix} \mathbf{\Phi}_1^T \otimes \mathbf{s}_1 & \mathbf{\Phi}_2^T \otimes \mathbf{s}_2 & \cdots & \mathbf{\Phi}_L^T \otimes \mathbf{s}_L \end{bmatrix}, \quad (3.13a)$$

$$\mathbf{G} \triangleq \mathbf{Y} \mathbf{\Pi}_{\Phi}^{\perp} \mathbf{Y}^H, \quad (3.13b)$$

$$\mathbf{\Pi}_{\Phi}^{\perp} \triangleq \mathbf{I}_N - \mathbf{\Pi}_{\Phi}, \quad (3.13c)$$

$$\mathbf{\Pi}_{\Phi} \triangleq \mathbf{\Phi}(\mathbf{v})^H (\mathbf{\Phi}(\mathbf{v}) \mathbf{\Phi}(\mathbf{v})^H)^{-1} \mathbf{\Phi}(\mathbf{v}), \quad (3.13d)$$

$$\mathbf{S} \triangleq \begin{bmatrix} \mathbf{s}_1 & \mathbf{s}_2 & \cdots & \mathbf{s}_L \end{bmatrix} = \mathbf{G}^{-\frac{1}{2}} \mathbf{A}, \quad (3.13e)$$

$$\mathbf{\Phi}(\mathbf{v}) \triangleq \begin{bmatrix} \mathbf{\Phi}_1^T & \mathbf{\Phi}_2^T & \cdots & \mathbf{\Phi}_L^T \end{bmatrix}^T, \quad (3.13f)$$

and  $\text{vecb}(\cdot)$  is a block-diagonal  $\text{vec}$  operator defined in [117, Eqn. 7]. Additionally, in (3.13e),  $\mathbf{s}_l$  is the  $l$ -th column of an  $L \times L$  matrix  $\mathbf{S} \triangleq \mathbf{G}^{-\frac{1}{2}} \mathbf{A}$ ; and in (3.13f),  $\mathbf{\Phi}_l$  is a  $P \times N$  matrix representing the  $l$ -th block of  $P$  rows of  $\mathbf{\Phi}(\mathbf{v})$ .

In our problem, however, the parameter  $\mathbf{v}$  is unknown, and therefore we compare the GLR test  $\max_{\mathbf{v}} \text{GLR}(\mathbf{v}) = \text{GLR}(\hat{\mathbf{v}})$  with a threshold.

### 3.4 Adaptive Waveform Design

In this section, we develop an adaptive OFDM waveform design technique to improve the target-detection performance. To derive a mathematical formulation for the waveform selection, we first create a utility function according to certain criteria

and then determine the parameters for the next transmitting waveform by optimizing this utility function. To construct such a utility function, we first study the detection performance assuming a known target velocity parameter  $\mathbf{v}$ . Then, we explicitly state the optimization problem and its solution.

### 3.4.1 Distributions of the Test Statistic for Known Target Velocity

In this subsection, we derive the distribution of  $\text{GLR}(\mathbf{v})$  when the target velocity is known. The motivation behind these derivations is to look for a criterion of adaptive waveform design; but not to analyze the detection performance with a known target velocity, because in our problem the target velocity is unknown.

When  $\mathbf{A}$  has full rank  $L$  and  $\mathbf{X}$  is a full matrix, (3.11) can be written in a concise form as

$$\frac{1}{\text{GLR}(\mathbf{v})} = \frac{|\mathbf{G}|}{|\mathbf{G} + \mathbf{H}|}, \quad (3.14)$$

where  $\mathbf{G} \triangleq \mathbf{Y}\mathbf{\Pi}_{\Phi}^{\perp}\mathbf{Y}$  and  $\mathbf{H} \triangleq \mathbf{Y}\mathbf{\Pi}_{\Phi}\mathbf{Y}^H$  are two projection matrices.

Under  $\mathcal{H}_0$ , our OFDM measurement model is  $\mathbf{Y} \sim \mathbb{C}\mathcal{N}_{L,N}(\mathbf{0}, \mathbf{I}_N \otimes \mathbf{\Sigma})$ . Therefore, provided that  $(N - r) \geq L$ ,  $\mathbf{G}$  is distributed as a complex Wishart matrix of order  $L$ , parameter  $\mathbf{\Sigma}$ , and  $(N - r)$  complex degrees of freedom. This is denoted as  $\mathbf{G} \sim \mathbb{C}\mathcal{W}_L(N - r, \mathbf{\Sigma})$ . Similarly, we get  $\mathbf{H} \sim \mathbb{C}\mathcal{W}_L(r, \mathbf{\Sigma})$  if  $r \geq L$ . Here  $r = \text{rank}(\mathbf{\Pi}_{\Phi}) = \text{rank}[\Phi(\mathbf{v})] \leq LP < N$ . Since  $\mathbf{\Pi}_{\Phi}^{\perp}$  and  $\mathbf{\Pi}_{\Phi}$  are orthogonal complements to each other, we know that  $\mathbf{\Pi}_{\Phi}^{\perp}\mathbf{\Pi}_{\Phi} = \mathbf{0}$ , and hence, following the Craig-Sakamoto theorem [118], [119],  $\mathbf{G}$  and  $\mathbf{H}$  are independently distributed. Then, the GLR test statistic is given

by [120, Th. 3.10], [121, Eqn. 4-33]

$$\frac{1}{\text{GLR}(\mathbf{v})} = \prod_{l=0}^{L-1} b_l, \quad (3.15)$$

where  $b_l$ s are mutually independent complex beta distributed random variables with  $((N - r) - (L - 1 - l))$  and  $r$  complex degrees of freedom, written as

$$b_l \sim \mathbb{CB}((N - r) - (L - 1 - l), r) \quad \text{for } l = 0, 1, \dots, L - 1. \quad (3.16)$$

This is similar to Wilks' lambda [122] for complex variables.

However, under  $\mathcal{H}_1$ , the distribution of  $\text{GLR}(\mathbf{v})$  does not have a closed-form expression in general. Under  $\mathcal{H}_1$ , we have  $\mathbf{Y} \sim \mathbb{CN}_{L,N}(\mathbf{M}, \mathbf{I}_N \otimes \Sigma)$ , where  $\mathbf{M} = \mathbf{A}\mathbf{X}\Phi(\mathbf{v})$ . Therefore, the random matrices  $\mathbf{G}$  and  $\mathbf{H}$  follow noncentral complex Wishart distributions, denoted as  $\mathbf{G} \sim \mathbb{CW}_L(N - r, \Sigma; \Theta_1)$  and  $\mathbf{H} \sim \mathbb{CW}_L(r, \Sigma; \Theta_2)$ , respectively; and  $\Theta_1 = \Sigma^{-1} \mathbf{M} \Pi_{\Phi}^{\perp} \mathbf{M}^H$ ,  $\Theta_2 = \Sigma^{-1} \mathbf{M} \Pi_{\Phi} \mathbf{M}^H$  are the noncentrality parameters [123, Th. 7.8.1, Cor. 7.8.1.1]. Since

$$\begin{aligned} \Theta_1 &= \Sigma^{-1} \mathbf{A}\mathbf{X}\Phi(\mathbf{v}) \left[ \mathbf{I}_N - \Phi(\mathbf{v})^H (\Phi(\mathbf{v})\Phi(\mathbf{v})^H)^{-1} \Phi(\mathbf{v}) \right] \Phi(\mathbf{v})^H \mathbf{X}^H \mathbf{A}^H, \\ &= \Sigma^{-1} \mathbf{A}\mathbf{X} \left[ \Phi(\mathbf{v})\Phi(\mathbf{v})^H - \Phi(\mathbf{v})\Phi(\mathbf{v})^H (\Phi(\mathbf{v})\Phi(\mathbf{v})^H)^{-1} \Phi(\mathbf{v})\Phi(\mathbf{v})^H \right] \mathbf{X}^H \mathbf{A}^H, \\ &= \mathbf{0}, \end{aligned} \quad (3.17)$$

$$\begin{aligned} \Theta_2 &= \Sigma^{-1} \mathbf{A}\mathbf{X}\Phi(\mathbf{v}) \left[ \Phi(\mathbf{v})^H (\Phi(\mathbf{v})\Phi(\mathbf{v})^H)^{-1} \Phi(\mathbf{v}) \right] \Phi(\mathbf{v})^H \mathbf{X}^H \mathbf{A}^H, \\ &= \Sigma^{-1} \mathbf{A}\mathbf{X}\Phi(\mathbf{v})\Phi(\mathbf{v})^H \mathbf{X}^H \mathbf{A}^H, \\ &= \Sigma^{-1} \mathbf{M}\mathbf{M}^H, \end{aligned} \quad (3.18)$$

we find that  $\mathbf{G}$  becomes a complex central Wishart matrix, denoted as  $\mathbf{G} \sim \mathbb{CW}_L(N - r, \Sigma)$ , whereas  $\mathbf{H}$  remains a complex noncentral Wishart matrix with  $\Sigma^{-1} \mathbf{M}\mathbf{M}^H$  as



the noncentrality parameter. But, we cannot simplify (3.14) any further such that it has a distribution with closed-form expression.

In a special case, when  $\text{rank}(\mathbf{M}) = 1$  (which is termed the “linear case” after Anderson [124], [125] in some statistical literature) the test statistic  $1/\text{GLR}(\mathbf{v})$  under  $\mathcal{H}_1$  can be written as a product of  $L$  independent complex beta random variables, where one of the beta variables is non-central [126], [127]. The noncentrality parameter is given as the single nonzero root of the equation  $|\mathbf{M}\mathbf{M}^H - \delta\mathbf{\Sigma}| = 0$ , which is same as  $\text{tr}(\mathbf{\Sigma}^{-1}\mathbf{M}\mathbf{M}^H)$ . Here we remark that to achieve  $\text{rank}(\mathbf{M}) = 1$  in our problem, we have to use a single frequency signal instead of a multi-frequency OFDM signal.

Since, the distribution of the GLR test statistic for the OFDM measurement model does not have a closed-form expression for a finite value of  $N$ , we explore the asymptotic performance characteristics of (3.11) assuming known target velocity. Following an analogous discussion on real Gaussian variables from [69, Ch. 8], [128] we find that as  $N \rightarrow \infty$ , under  $\mathcal{H}_0$ ,  $N \ln \text{GLR}(\mathbf{v})$  has a complex chi-square distribution with  $rL$  complex degrees of freedom, denoted as

$$N \ln \text{GLR}(\mathbf{v}) \sim \mathbb{C}\chi_{rL}^2. \quad (3.19)$$

Note that the expression of the chi-square distribution does not depend on the unknown covariance matrix  $\mathbf{\Sigma}$ . Thus, when  $\mathbf{v}$  is known, (3.11) corresponds to a CFAR test.

Under  $\mathcal{H}_1$ , the limiting distribution of  $N \ln \text{GLR}(\mathbf{v})$  is a complex noncentral distribution with  $rL$  complex degrees of freedom, denoted as

$$N \ln \text{GLR}(\mathbf{v}) \sim \mathbb{C}\chi_{rL}^2(\lambda), \quad (3.20)$$

where  $\lambda = \sum_{l=0}^{L-1} \delta_l$  is the noncentrality parameter and  $\delta_0, \delta_1, \dots, \delta_{L-1}$  are the roots of  $|\mathbf{M}\mathbf{M}^H - \delta\boldsymbol{\Sigma}| = 0$ . Obviously, another way to represent the same noncentrality parameter is  $\lambda = \text{tr}(\boldsymbol{\Sigma}^{-1}\mathbf{M}\mathbf{M}^H)$ . We may call the matrix  $\boldsymbol{\Sigma}^{-1}\mathbf{M}\mathbf{M}^H$  as the “signal-to-noise ratio matrix,” and hence the trace of it can be considered as a sum of squared Mahalanobis distances [68].

### 3.4.2 Waveform Design

From the discussion of the previous subsection, it is clear that the GLR test asymptotically results in a CFAR detector when the target velocity is known, and the detection performance depends on the system parameters through the noncentrality parameter  $\lambda$ . Therefore, it is possible to improve the detection performance by maximizing this noncentrality parameter.

However, in our problem the target velocity parameter  $\mathbf{v}$  is unknown. Moreover, in the OFDM measurement model the target scattering matrix  $\mathbf{X}$  is block diagonal. Still in our adaptive waveform design problem we maximize the same expression of the noncentrality parameter subject to a pre-defined energy constraint. Thus, we formulate the optimization problem as

$$\begin{aligned} \mathbf{a}_{\text{opt}} &= \arg \max_{\mathbf{a} \in \mathbb{C}^L} \text{tr}(\boldsymbol{\Sigma}^{-1}\mathbf{A}\mathbf{X}\Phi(\mathbf{v})\Phi(\mathbf{v})^H\mathbf{X}^H\mathbf{A}^H), \\ &\text{subject to } \mathbf{a}^H\mathbf{a} = 1. \end{aligned} \quad (3.21)$$

Applying the theorem of Appendix B, we can rewrite this problem as

$$\begin{aligned} \mathbf{a}_{\text{opt}} &= \arg \max_{\mathbf{a} \in \mathbb{C}^L} \mathbf{a}^H \left[ (\mathbf{X} \Phi(\mathbf{v}) \Phi(\mathbf{v})^H \mathbf{X}^H)^T \odot \Sigma^{-1} \right] \mathbf{a}, \\ &\text{subject to } \mathbf{a}^H \mathbf{a} = 1. \end{aligned} \quad (3.22)$$

Hence, our optimization problem reduces to a simple eigenvalue-eigenvector problem, and the optimal solution,  $\mathbf{a}_{\text{opt}}$ , is the eigenvector corresponding to the largest eigenvalue of  $\left[ (\mathbf{X} \Phi(\mathbf{v}) \Phi(\mathbf{v})^H \mathbf{X}^H)^T \odot \Sigma^{-1} \right]$ .

Note that in our problem  $\mathbf{v}$ ,  $\mathbf{X}$ , and  $\Sigma$  are not known. Hence, we use their estimated values to obtain  $\mathbf{a}_{\text{opt}}$  for the next CPI. First, a nonoptimal  $\mathbf{a}$  is transmitted and the corresponding measurements are stored over one particular CPI. Then, we estimate  $\hat{\mathbf{v}} = \arg \max_{\mathbf{v}} \text{GLR}(\mathbf{v})$ . Substituting  $\hat{\mathbf{v}}$  into (3.5), we compute  $\Phi(\hat{\mathbf{v}})$  and subsequently  $\hat{\mathbf{X}}$  using (3.12) and (3.13). Then, the estimate of  $\Sigma$  is evaluated as  $\hat{\Sigma} = (1/N) \left( \mathbf{Y} - \mathbf{A} \hat{\mathbf{X}} \Phi(\hat{\mathbf{v}}) \right) \left( \mathbf{Y} - \mathbf{A} \hat{\mathbf{X}} \Phi(\hat{\mathbf{v}}) \right)^H$ . Finally, we choose  $\mathbf{a}_{\text{opt}}$  as the eigenvector corresponding to the largest eigenvalue of  $\left[ \left( \hat{\mathbf{X}} \Phi(\hat{\mathbf{v}}) \Phi(\hat{\mathbf{v}})^H \hat{\mathbf{X}}^H \right)^T \odot \hat{\Sigma}^{-1} \right]$ .

### 3.5 Temporally Correlated Noise

In this section, we extend our model to include temporal correlation among the measurements. Recall that so far we have assumed that the clutter and measurement noise are the independent realizations of the same Gaussian random process from pulse to pulse. However, this assumption may not be valid at a high PRF [113]. In the following, we first present the statistical assumptions of temporally correlated noise for the OFDM measurement model, presented in (3.6), and then discuss the detection tests.

### 3.5.1 Statistical Assumptions

To develop a statistical model for the temporally correlated noise from pulse to pulse measurements, we look into a branch of statistics known as the nearest neighbor analysis [114], [115]. Instead of choosing any unstructured covariance matrix, we assume a Kronecker product structure of the form  $\mathbf{V} \otimes \mathbf{\Sigma}$ , where  $\mathbf{V}$  is an  $N \times N$  unknown positive definite temporal covariance matrix. Based on this assumption, the modified versions of (3.8) can be written as

$$\mathbf{Y} \sim \mathbb{C}\mathcal{N}_{L,N}(\mathbf{A} \mathbf{X} \Phi(\mathbf{v}), \mathbf{V} \otimes \mathbf{\Sigma}). \quad (3.23)$$

The matrix  $\mathbf{V}$  can have any structure or can even be unstructured. In the statistical literature, two structured covariance matrices are very common. These are the compound symmetric (CS) structure [129] and autoregressive structure of order 1 (AR(1)) [130]. The CS covariance structure assumes that all the temporal measurements are equicorrelated and do not depend on the duration between the two time points, i.e.,

$$[\mathbf{V}(\rho)]_{(i,j)} = \begin{cases} 1 & \text{when } i = j \\ \rho & \text{otherwise} \end{cases}, \quad \text{for } i, j = 0, 1, \dots, N-1, \quad (3.24)$$

where  $0 \leq \rho \leq 1$  is the coefficient of temporal correlation between two time points. In AR(1) covariance structure, the temporal measurements are assumed to be more highly correlated if they are close to each other in time duration, i.e.,

$$[\mathbf{V}(\rho)]_{(i,j)} = \rho^{|i-j|}, \quad \text{for } i, j = 0, 1, \dots, N-1. \quad (3.25)$$

In our work, we consider the AR(1) model as it is suitable for pulsed radar applications in which the measurements are collected at equispaced time intervals. Note that in (3.24) and (3.25) we explicitly write  $\mathbf{V}(\rho)$  to stress the fact that the temporal correlation matrix  $\mathbf{V}$  (and also its inverse) is completely characterized by a single parameter  $\rho$ .

### 3.5.2 Detection Test Under Temporal Correlations

We construct the decision problem in terms of two possible hypotheses  $\mathcal{H}_0$  and  $\mathcal{H}_1$ , to detect the presence of a target in the range cell under consideration, as

$$\begin{cases} \mathcal{H}_0 : \mathbf{X} = \mathbf{0}, \rho, \Sigma \text{ unknown} \\ \mathcal{H}_1 : \mathbf{X} \neq \mathbf{0}, \mathbf{v}, \rho, \Sigma \text{ unknown} \end{cases}. \quad (3.26)$$

As before, since the parameters  $\rho$ ,  $\mathbf{v}$ , and  $\Sigma$  are unknown, we apply the GLR test.

The test compares the ratio of the likelihood functions, maximized with respect to the unknown parameters, under the two hypotheses with a threshold  $\gamma'$  as follows:

$$\text{GLR}(\hat{\rho}, \hat{\mathbf{v}}) = \frac{\max_{\rho, \mathbf{v}} f_{\mathcal{H}_1}(\mathbf{Y}; \rho, \mathbf{v}, \hat{\mathbf{X}}, \hat{\Sigma}_1)}{\max_{\rho} f_{\mathcal{H}_0}(\mathbf{Y}; \rho, \hat{\Sigma}_0)} > \gamma', \quad (3.27)$$

where the MLEs of  $\mathbf{X}$  and  $\Sigma$  are computed by replacing  $\mathbf{Y}$  and  $\Phi(\mathbf{v})$  with  $\mathbf{Y}\mathbf{V}(\rho)^{-\frac{1}{2}}$  and  $\Phi(\mathbf{v})\mathbf{V}(\rho)^{-\frac{1}{2}}$ , respectively.

## 3.6 Numerical Results

In this section, we present the results of several numerical examples to illustrate the performance characteristics of our proposed detector, as the associated GLR test statistic with unknown target velocity does not have any closed-form analytical expression. For simplicity we considered a 2D scenario, where both the radar and target were in the same plane, as shown in Fig. 3.2. Our analyses can easily be extended to 3D scenarios. First, we provide a description of the simulation setup, and then discuss different numerical examples.

- Target and multipath parameters:
  - The target was moving with velocity  $\mathbf{v} = 7.07\hat{i} + 7.07\hat{j}$  m/s. This implies that  $\mathbf{v}_{\text{TRUE}} = [7.07, 7.07]^T$  m/s.
  - Throughout a given CPI, the target remained within a particular range cell. We simulated the situation of a range cell centered at 2 km North and 5m East with respect to the radar (positioned at the origin).
  - There were three different paths (i.e.,  $P = 3$ ) between that particular range cell and the radar: one direct path and two specular multipaths due to a couple of reflecting surfaces oriented along North-South direction at 10m East and 10m West.
  - The scattering coefficients of the target (i.e., the entries of  $\mathbf{X}$ ) were generated from a  $\mathbb{CN}(0, 1)$  distribution.
- Radar parameters:
  - Carrier frequency  $f_c = 1$  GHz.

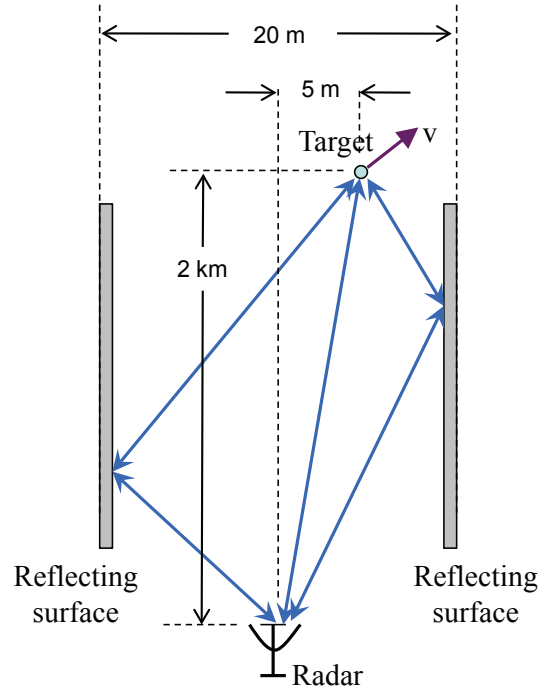


Figure 3.2: A schematic representation of the multipath scenario considered for numerical examples.

- Available bandwidth  $B = 100$  MHz.
- Number of subcarriers  $L = 4$ .
- Subcarrier spacing  $\Delta f = B/(L + 1) = 20$  MHz.
- Pulse width  $T = 1/\Delta f = 50$  ns.
- Pulse repetition interval  $T_p = 20 \mu\text{s}$ .
- All the transmit weights were equal, i.e.,  $\mathbf{a} = (1/\sqrt{L})\mathbf{1}_L$ .

We performed Monte Carlo simulations based on 20,000 independent trials to realize the following results. The entries of  $\Sigma^{1/2}$  were realized from the  $\mathcal{CN}(0, 1)$  distribution

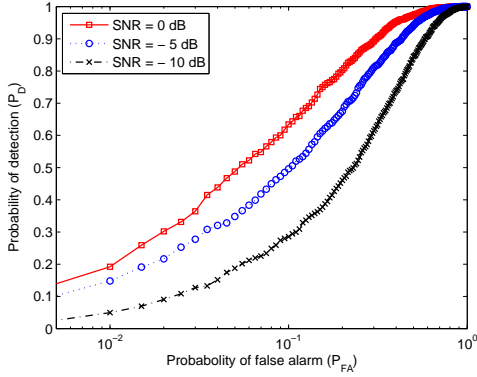


Figure 3.3: Effects of different SNR values on detection probability as a function of probability of false alarm.

and then were scaled to satisfy the required SNR, defined as

$$\text{SNR} = \frac{\left[ (1/N) \sum_{n=1}^N (\mathbf{A}\mathbf{X}\phi(n, \mathbf{v}_{\text{TRUE}}))^H \mathbf{A}\mathbf{X}\phi(n, \mathbf{v}_{\text{TRUE}}) \right]}{\text{tr}(\boldsymbol{\Sigma})}. \quad (3.28)$$

## Detector Performance

Fig. 3.3 depicts the variations of the probability of detection ( $P_D$ ) as a function of the probability of false alarm ( $P_{FA}$ ) at three different SNR values. As expected, the detection performance improved as SNR is increased. Being a wideband signal the OFDM could resolve the multipath and overcome fading. Additionally, it exploited the target responses at multiple frequencies.

To show the advantage of using a multi-frequency signalling system, we compared the detection performance at three different values of  $L$ , while keeping the SNR fixed at  $-5$  dB. The results are presented in Fig. 3.4. Hence, it is evident that the frequency diversity improved the target-detection performance in an OFDM system.



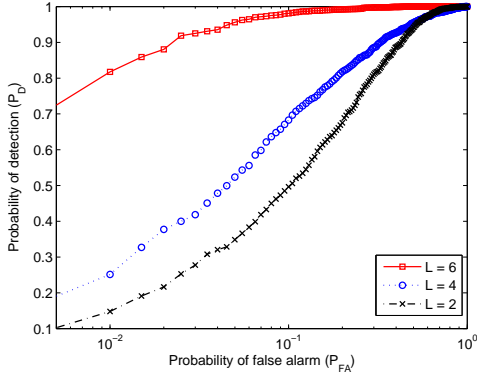


Figure 3.4: Effects of different number of subcarriers on detection probability as a function of probability of false alarm.

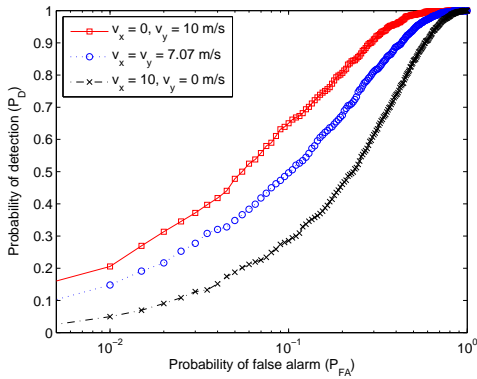


Figure 3.5: Effects of different directions of target velocity vector on detection probability as a function of probability of false alarm.

We also studied the effects of varying the directions of the velocity vector on the detection performance at three different conditions:  $\mathbf{v}_{\text{TRUE}}^T = [0, 10], [7.07, 7.07], [10, 0]$  m/s. The results are depicted in Fig. 3.5. For this simulation we kept the SNR fixed at  $-5$  dB. As the angle between the target velocity vector and radar LOS was increased, the performance of the OFDM detector deteriorated.

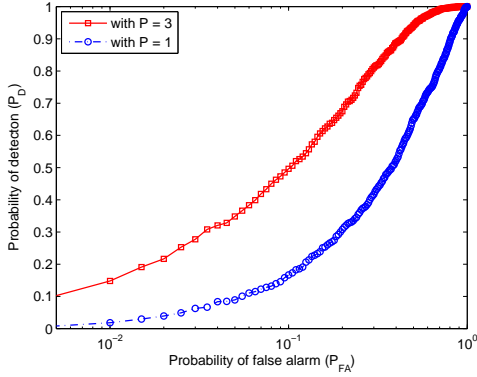


Figure 3.6: Effects of exploiting the multipath reflections on detection probability as a function of probability of false alarm.

## Importance of Multipath Modeling

To understand the importance of proper exploitation of multipath reflections, we devised the following simulations. We changed the velocity of the target such that it moved perpendicular to the LOS direction. Then, we compared the detection performances of the two systems: one of them considered all  $P$  ( $= 3$ ) multipath reflections, and the other considered only the LOS return. Fig. 3.6 shows the results at  $\text{SNR} = -5$  dB. The OFDM signal, being a wideband, could better exploit the multipath reflections to improve the detection performance.

A similar conclusion can also be drawn from Fig. 3.7. For this simulation, we generated the measurements for the OFDM signalling scheme in the presence of multipath using the same setup as described before. However, in the detector, we ignored the presence of multipaths in the tested range cell. This may happen when the radar does not have a knowledge of the possible multipath scenario. From Fig. 3.7, we see that the performance deteriorated when the detector in the OFDM model ignored the multipath reflections.

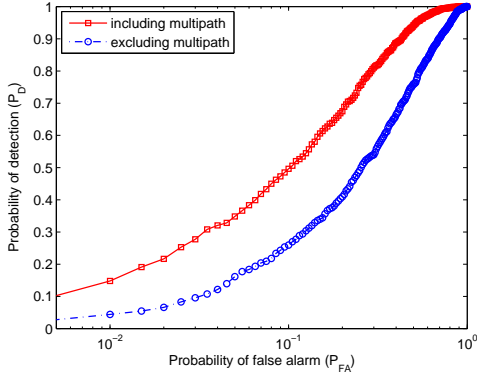


Figure 3.7: Effects of ignoring the multipath reflections at the detector on detection probability as a function of probability of false alarm.

## Adaptive OFDM Waveform Design

To study the improvement in target-detection performance due to the proposed adaptive waveform design technique, we devised a simple problem. We assumed a system in which we transmitted  $a_l = 1/\sqrt{L}\forall l$  in the first  $N$  pulses. Then, based on the corresponding measurements we solved (3.22) to compute the optimized values of  $a_l$ s for the next  $N$  pulses. We compared this system with another system in which both the two sets of  $N$  pulses transmitted  $a_l = 1/\sqrt{L}\forall l$ . We fixed the SNR at  $-5$  dB for this simulation. From Fig. 3.8 we observe that the detection performance of the adaptive system was considerably improved for the OFDM model.

## Under Temporal Correlation

Fig. 3.9 depicts the detection performance at three different values of the temporal correlation coefficient. We used the AR(1) covariance structure, described in (3.25), to introduce temporal correlation among the measurements. For this simulation we

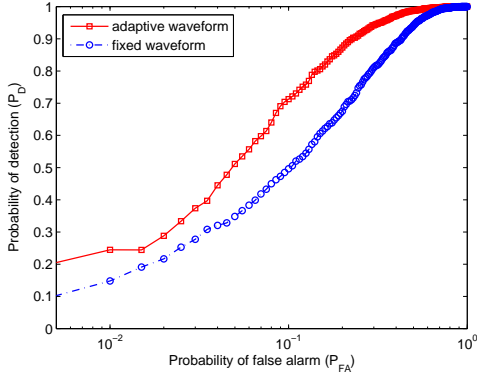


Figure 3.8: Gain due to adaptive waveform design of detection probability as a function of probability of false alarm.

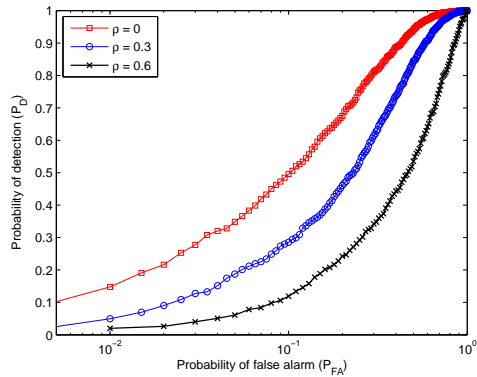


Figure 3.9: Effects of different temporal correlations on detection probability as a function of probability of false alarm.

kept the SNR fixed at  $-5$  dB. It is evident from this analysis that the target-detection performance deteriorated as the level of temporal correlation was increased.

## Detector Performance for Known Target Velocity

Finally, in Fig. 3.10 we show comparative performance results of the OFDM detector for known and unknown target velocity  $\mathbf{v}$ . We plot these results at two different

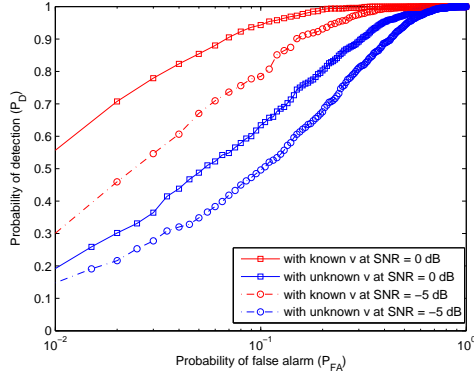


Figure 3.10: Loss due to the target-velocity estimation of detection probability as a function of probability of false alarm.

SNR values. The detection performance for known target velocity may be looked upon as a hypothetical scenario, because in the underlying detection problem we try to decide about the presence or absence of a target whose velocity is known beforehand. However, this analysis showed us quantitatively to what extent the detection performance (for unknown  $\mathbf{v}$ ) degraded due to the estimation of  $\mathbf{v}$ . For example, the value of  $P_D$  dropped from 0.56 to 0.3 at  $P_{FA} = 10^{-2}$  and SNR = 0 dB due to the velocity estimation process.

### 3.7 Summary

We addressed the problem of detecting a moving target by exploiting multipath reflections. We demonstrated that the target-detection capability can be significantly improved by utilizing multiple Doppler shifts corresponding to the projections of the target velocity on each of the multipath components. First, we developed an OFDM radar measurement model and formulated the detection problem as a statistical hypothesis test. Then, we proposed an algorithm to optimally design the

spectral parameters of the transmitting OFDM waveform for the next coherent processing interval. Our numerical examples illustrated the performance characteristics of the proposed detector and demonstrated the achieved performance improvement due to the adaptive OFDM waveform design. In the next chapter, we continue our discussion of the target-detection problem and propose an efficient sparse-signal recovery algorithm after transforming the detection problem into the task of estimating the spectrum of a sparse signal.

# Chapter 4

## Waveform Design Based on Multi-Objective Optimization<sup>3</sup>

In this chapter, we reformulate the target-detection problem as the task of sparse-signal spectrum estimation. At a particular range cell, we exploit the sparsity of multiple paths and the knowledge of the environment to estimate the path along which target responses are received. To estimate the sparse vector, we employ a collection of multiple small Dantzig selectors (DS) that utilizes more prior structures of the sparse vector than the standard DS. We use the  $\ell_1$ -constrained minimal singular value ( $\ell_1$ -CMSV) of the measurement matrix to analytically evaluate the reconstruction performance [131]. In addition, we propose a constrained multi-objective optimization (MOO) based algorithm [64] – [67] to adaptively design the spectral parameters of the OFDM waveform by simultaneously minimizing the upper bound on the estimation error to improve the efficiency of sparse-recovery and maximizing the squared Mahalanobis-distance [68] to increase the performance of the underlying detection problem.

---

<sup>3</sup>Based on S. Sen, G. Tang, and A. Nehorai, “Multi-objective optimization of OFDM radar waveform for target detection,” *IEEE Trans. Signal Process.*, vol. 59, no. 2, Feb. 2011. ©[2010] IEEE.

## 4.1 Introduction

For a target moving in a multipath-rich environment, we know that the radar receives the target information through an LOS, several reflected paths, or both. Therefore, using our knowledge of the geometry, we can determine all the possible paths, be they LOS or reflected, and the associated target locations corresponding to a particular range cell. Then, considering the presence of a single target, we can determine the paths along which the target response is received by solving a simple sparse recovery algorithm through a linear program, e.g.,  $\ell_1$ -minimization [132] or second-order cone programming (SOCP) [133], or through a greedy pursuit, e.g., orthogonal matching pursuit (OMP) [134] or compressive sampling matching pursuit (CoSaMP) [91]. Thus, we transform the target-detection problem into the task of estimating the spectrum of a sparse signal. Other recent applications of the sparsity-based (or compressive sensing based) signal processing algorithms to different radar problems can be found in [135] – [139].

First, we develop a parametric OFDM measurement model for a particular range cell, to detect a far-field point target moving in multipath scenarios. For simplicity, we consider only first-order (or single bounce) specularly reflected multipath signals. Then, we convert the model to a sparse model that accounts for the target returns over all possible signal paths and target velocities. The nonzero components of the sparse vector in our model correspond to the scattering coefficients of the target at different OFDM subcarriers. We assume that the clutter and measurement noise are temporally white.

To estimate the sparse vector, we propose a sparse-recovery algorithm based on a collection of multiple small Dantzig selectors [63]. The DS approach belongs to the



class of convex relaxation methods in which the  $\ell_0$  norm is replaced by the  $\ell_1$  norm that remains a measure of sparsity while being a convex function. Other examples of convex relaxation methods include the basis pursuit [132] and LASSO estimator [140]. Furthermore, we analytically evaluate the performance characteristics and show that our decomposed DS has advantages over the standard DS both in terms of computation and performance. To analyze the reconstruction performance, we consider the  $\ell_1$ -constrained minimal singular value ( $\ell_1$ -CMSV) of the measurement matrix [131]. Compared with the traditional restricted isometry constant (RIC) [141], [142], which is extremely difficult to compute for an arbitrarily given matrix, the  $\ell_1$ -CMSV is an easily computable measure and provides more intuition on the stability of sparse-signal recovery. More importantly, several algorithms to compute the  $\ell_1$ -CMSV of any given measurement matrix are already designed in [131].

Next, we propose a criterion to optimally design the spectral parameters of the transmitting OFDM waveform for the next coherent processing interval, based on the MOO approach [64] – [67]. We observe that if the signal parameters are designed to minimize the upper bound on the sparse-estimation error, then the resultant waveform depends solely on the properties of the measurement matrix. However, to achieve a better performance, it is also essential that the signal parameters are adaptive to the operational scenario involving dynamic target states and nonstationary environmental conditions. Hence, in addition to minimizing the upper bound on the estimation error, we propose maximizing another utility function based on the squared Mahalanobis-distance [68], [69], one that depends on the target and noise parameters. Based on these arguments, we develop a constrained MOO problem to simultaneously optimize two objective functions: to minimize the upper bound on the estimation error and to maximize the squared Mahalanobis-distance.

Often, a MOO problem does not have a single optimal solution but rather a set of solutions known as Pareto-optimal solutions [64]. This type of optimality was originally introduced by Francis Ysidro Edgeworth in 1881 [143] and later generalized by Vilfredo Pareto in 1896 [144]. All the solutions residing on the Pareto-front are superior to other solutions in the search space when all objectives are considered. The idea of finding as many Pareto-optimal solutions as possible motivates the use of evolutionary algorithms (EAs) that generate several solutions in a single run. Following the same motivation, we apply the well-known nondominated sorting genetic algorithm II (NSGA-II) [70] to solve our MOO problem. Previous work in the application of multi-objective evolutionary algorithms (MOEAs) for radar system design includes [145] – [149] and the references therein.

To illustrate the sparse-estimation performance for a target-detection problem and to demonstrate the performance improvement due to the adaptive OFDM waveform design, we present several numerical examples. We evaluate the performance characteristics in terms of the normalized root mean squared error (RMSE) and empirical receiver operating characteristic (ROC). From the results of the adaptive design, we observe that the solution of the MOO-based design in general produces the best performance. Assuming that the noise powers over different subcarriers are the same, we infer that the solution of the MOO distributes the energy of the optimal waveform across different subcarriers in proportion to the distribution of the target energy; i.e., it puts more signal energy to that particular subcarrier in which the target response is stronger.

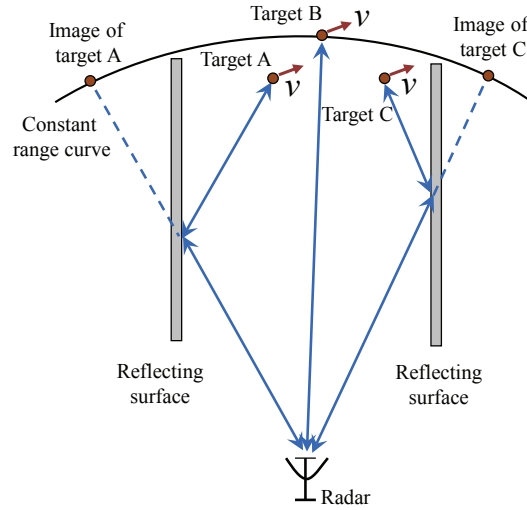


Figure 4.1: A schematic representation of the multipath scenario.

## 4.2 Problem Description and Modeling

Fig. 4.1 presents a schematic representation of the problem scenario. As before, we consider a far-field point target in a multipath-rich environment, moving with a constant relative velocity  $\mathbf{v}$  with respect to the radar. At the operating frequency we assume that the reflecting surfaces produce only specular reflections of the radar signal, and for simplicity we consider only the first-order reflections. We further assume that the radar has complete knowledge of the environment under surveillance. This assumption implies that for a particular range cell (shown as the curved line in Fig. 4.1) the radar knows all the possible paths, be they LOS or reflected. Now, any target (e.g., Target B) or any image of a target (e.g., Target A or C) residing on the constant-range curved line has the same roundtrip delay and produces returns in the same range cell. Our goal here is to decide whether a target is present (out of all possible paths) at the range cell under test and to determine the corresponding location of the target by using knowledge of the environment.

### 4.2.1 Sparse Measurement Model

We consider an OFDM signalling system with  $\mathbf{a} = [a_0, a_1, \dots, a_{L-1}]^T$  representing the complex transmit-weights over the  $L$  subcarriers, as described previously in (2.1) – (2.4). Then, similar to (3.1), the complex envelope of the received signal along the  $p$ -th path due to only the  $l$ -th subcarrier and corresponding to a specific range cell (denoted by the roundtrip delay  $\tau$ ) can be written as

$$\tilde{y}_{lp}(t) = x_{lp} \tilde{s}_l(\gamma_p(t - \tau)) + \tilde{e}_{lp}(t), \quad (4.1)$$

where all the notations have the same interpretations as described in reference to (3.1). Following a similar approach as in Section 3.2.1 and incorporating the information of the known range cell as  $t = \tau + nT_p, n = 0, 1, \dots, N - 1$ , we can write the complex envelope of the received signal at the output of the  $l$ -th subchannel as

$$y_{lp}(n) = a_l x_{lp} \phi_l(n, p, \mathbf{v}) + e_{lp}(n), \quad \text{for } l = 0, 1, \dots, L - 1, n = 0, 1, \dots, N - 1, \quad (4.2)$$

where

$$\phi_l(n, p, \mathbf{v}) \triangleq e^{-j2\pi f_l \tau} e^{j2\pi f_l \beta_p n T_p} \quad (4.3)$$

is a function of the unknown path index  $p$  through which the radar receives the information about the target, the unknown target-velocity  $\mathbf{v}$ , and the known target-delay  $\tau$ .

Next, we discretize the possible signal paths and target velocities into  $P$  and  $V$  grid points, respectively. In general, the values of  $P$  and  $V$  could be very large. However, restricting our operation to a narrow region of interest (e.g., an urban

canyon where the range is much greater than the width) and a few class of targets that have comparable velocities (e.g., cars/trucks within a city environment), we can restrict the values of  $P$  and  $V$  to smaller numbers. Then, considering all possible combinations of  $(p_i, \mathbf{v}_j), i = 1, 2, \dots, P, j = 1, 2, \dots, V$ , we can write the complex envelope of the received signal at the output of the  $l$ -th subchannel as

$$y_l(n) = a_l \boldsymbol{\phi}_l(n)^T \mathbf{x}_l + e_l(n), \quad (4.4)$$

where

- $\boldsymbol{\phi}_l(n) = [\phi_l(n, p_1, \mathbf{v}_1), \dots, \phi_l(n, p_1, \mathbf{v}_V), \phi_l(n, p_2, \mathbf{v}_1), \dots, \phi_l(n, p_P, \mathbf{v}_V)]^T$ .
- $\mathbf{x}_l$  is a  $PV \times 1$  sparse-vector, having only  $k_l$  nonzero entries corresponding to the true signal paths and target velocity; i.e.,

$$\begin{aligned} k_l &= |\mathcal{I}_l|, \quad \text{where} & (4.5) \\ \mathcal{I}_l &= \left\{ \tilde{i} \in [1, P] : \text{target information is received along the } p_{\tilde{i}}\text{-th path} \right\}. \end{aligned}$$

Stacking the measurements of all subchannels into an  $L \times 1$  vector, we get

$$\mathbf{y}(n) = \mathbf{A} \boldsymbol{\Phi}(n) \mathbf{x} + \mathbf{e}(n), \quad (4.6)$$

where

- $\mathbf{y}(n) = [y_0(n), y_1(n), \dots, y_{L-1}(n)]^T$ .
- $\mathbf{A} = \text{diag}(\mathbf{a})$  is an  $L \times L$  complex diagonal matrix that contains the transmitted weights  $\mathbf{a}$ .

- $\Phi(n) = \text{blkdiag}(\phi_0(n)^T, \phi_2(n)^T, \dots, \phi_{L-1}(n)^T)$  is an  $L \times LPV$  complex rectangular block-diagonal matrix.
- $\mathbf{x} = [\mathbf{x}_0^T, \mathbf{x}_1^T, \dots, \mathbf{x}_{L-1}^T]^T$  is an  $LPV \times 1$  sparse-vector that has  $k = \sum_{l=0}^{L-1} k_l$  nonzero entries representing the scattering coefficients of the target along the received paths.
- $\mathbf{e}(n) = [e_0(n), e_1(n), \dots, e_{L-1}(n)]^T$  is an  $L \times 1$  vector of clutter returns, measurement noise, and co-channel interference.

Then, concatenating all the temporal data columnwise into an  $LN \times 1$  vector, we obtain a sparse measurement model as follows:

$$\mathbf{y} = \Phi \mathbf{x} + \mathbf{e}, \quad (4.7)$$

where

- $\mathbf{y} = [\mathbf{y}(0)^T, \mathbf{y}(1)^T, \dots, \mathbf{y}(N-1)^T]^T$ .
- $\Phi = [(\mathbf{A}\Phi(0))^T \dots (\mathbf{A}\Phi(N-1))^T]^T$  is an  $LN \times LPV$  matrix containing all possible combinations of signal path and target velocity.
- $\mathbf{e} = [\mathbf{e}(0)^T, \mathbf{e}(1)^T, \dots, \mathbf{e}(N-1)^T]^T$  is an  $LN \times 1$  vector comprising clutter returns, noise, and interference.

## 4.2.2 Statistical Assumptions

We consider the same statistical assumptions as described in Section 3.2.2; i.e., we assume that  $\mathbf{e}(n)$  is a temporally white and circularly symmetric zero-mean complex Gaussian vector, correlated between different subchannels with positive definite covariance matrix  $\Sigma$ . Hence, the OFDM measurements in (4.7) are distributed as

$$\mathbf{y} \sim \mathcal{CN}_{LN}(\Phi \mathbf{x}, \mathbf{I}_N \otimes \Sigma). \quad (4.8)$$

## 4.3 Sparse Recovery and Performance Analysis

In this section, we first develop a sparse recovery algorithm for the measurement model presented in the previous section. Then, we analytically evaluate its performance characteristics in terms of an upper bound on the  $\ell_2$ -norm of the sparse-estimation error.

### 4.3.1 Sparse Recovery

Sparsity-based signal processing recently has received significant attention in many fields. The basic theory tells us that under certain conditions an unknown sparse vector  $\mathbf{x}$ , which has only a few nonzero entries (denoted as  $k = \|\mathbf{x}\|_0$ ), can be recovered exactly with high probability from  $\mathbf{y} = \Phi \mathbf{x}$ , even if the measurement matrix  $\Phi$  has far fewer rows than columns [150] – [152]. One of the most popular approaches of sparse signal recovery is the Dantzig selector. It provides an estimate of  $\mathbf{x}$  as a solution to

the following  $\ell_1$ -regularization problem:

$$\min_{\mathbf{z} \in \mathbb{C}^{LPV}} \|\mathbf{z}\|_1 \quad \text{subject to} \quad \|\Phi^H (\mathbf{y} - \Phi \mathbf{z})\|_\infty \leq \lambda \cdot \sigma, \quad (4.9)$$

where  $\lambda = \sqrt{2 \log(LPV)}$  is a control parameter that ensures that the residual  $(\mathbf{y} - \Phi \mathbf{z})$  is within the noise level and  $\sigma = \sqrt{\text{tr}(\Sigma)/L}$ .

However, from the construction of  $\mathbf{x}$  in (4.4) and (4.6), we observe an additional structure, described as follows:

$$\mathbf{x} = [\mathbf{x}_0^T, \mathbf{x}_1^T, \dots, \mathbf{x}_{L-1}^T]^T, \quad (4.10)$$

where each  $\mathbf{x}_l$ ,  $l = 0, 1, \dots, L - 1$ , is sparse with sparsity level  $k_l = \|\mathbf{x}_l\|_0$ , and  $k = \sum_{l=0}^{L-1} k_l$ . Furthermore, the system matrix  $\Phi$  in (4.7) can also be expressed as

$$\Phi = [\Phi_0 \quad \Phi_1 \quad \dots \quad \Phi_{L-1}], \quad (4.11)$$

where each block-matrix of dimension  $LN \times PV$ , defined as

$$\Phi_l = [\mathbf{0} \cdots \mathbf{0} \quad \underbrace{a_l \phi_l(0)}_{\text{index } =l} \quad \mathbf{0} \cdots \mathbf{0} \quad \underbrace{a_l \phi_l(1)}_{\text{index } =l+L} \quad \mathbf{0} \cdots \mathbf{0} \quad \underbrace{a_l \phi_l(N-1)}_{\text{index } =l+(N-1)L} \quad \mathbf{0} \cdots \mathbf{0}]^T, \quad (4.12)$$

is orthogonal to any other block-matrix; i.e.,  $\Phi_{l_1}^H \Phi_{l_2} = \mathbf{0}$  for  $l_1 \neq l_2$ . Here  $\phi_l(\cdot)$  is the same as the one defined in relation to (4.4). Note also the difference in notation between  $\Phi_l$  (which is a columnwise block-matrix) and  $\Phi(n)$  (which is a rowwise block-matrix), defined in (4.6).



To exploit this additional structure in the sparse-recovery algorithm, we propose a better reconstruction algorithm that solves  $L$  small Dantzig selectors:

$$\min_{\mathbf{z}_l \in \mathbb{C}^{PV}} \|\mathbf{z}_l\|_1 \quad \text{subject to} \quad \|\Phi_l^H (\mathbf{y} - \Phi_l \mathbf{z}_l)\|_\infty \leq \lambda_l \cdot \sigma \quad \text{for } l = 0, \dots, L-1, \quad (4.13)$$

where  $\lambda_l = \sqrt{2 \log(PV)}$ . We show in the next subsection that (4.13) has advantages over (4.9) both in terms of computation and performance, because more prior structures of the sparse vector are exploited.

### 4.3.2 Performance Analysis

Many functions of the system matrix  $\Phi$  have been proposed to analyze the performance of methods used to recover  $\mathbf{x}$  from  $\mathbf{y}$ , the most popular measure being the restricted isometry constant (RIC). However, for an arbitrarily given matrix, the computation of RIC is extremely difficult. Therefore, to assess the reconstruction performance of an  $\ell_1$ -based algorithm we use a new, easily computable measure,  $\ell_1$ -constrained minimal singular value ( $\ell_1$ -CMSV) of  $\Phi$  [131]. According to [131, Def. 4], we define the  $\ell_1$ -CMSV of  $\Phi$  as

$$\rho_s(\Phi) = \min_{\mathbf{x} \neq \mathbf{0}, s_1(\mathbf{x}) \leq s} \frac{\|\Phi \mathbf{x}\|_2}{\|\mathbf{x}\|_2}, \quad \text{for any } s \in [1, LPV], \quad (4.14)$$

and

$$s_1(\mathbf{x}) \triangleq \frac{\|\mathbf{x}\|_1^2}{\|\mathbf{x}\|_2^2} \leq k, \quad \text{when } k = \|\mathbf{x}\|_0. \quad (4.15)$$

Then, the performance of our decomposed DS in (4.13) is given by the following theorem:

**Theorem 1.** Suppose  $\mathbf{x} \in \mathbb{C}^{LPV}$  is a  $k$ -sparse vector having an additional structure as presented in (4.10), with each  $\mathbf{x}_l \in \mathbb{C}^{PV}$  being a  $k_l$ -sparse vector, and (4.7) is the measurement model. Choose  $\lambda_l = \sqrt{2 \log(PV)}$  in (4.13). Then, with high probability,  $\hat{\mathbf{x}}$  satisfies

$$\|\hat{\mathbf{x}} - \mathbf{x}\|_2 \leq 4 \sqrt{\sum_{l=0}^{L-1} \frac{\lambda_l^2 k_l \sigma^2}{\rho_{4k_l}^4(\Phi_l)}}, \quad (4.16)$$

where the concentrated solution  $\hat{\mathbf{x}} = [\hat{\mathbf{x}}_0^T, \hat{\mathbf{x}}_1^T, \dots, \hat{\mathbf{x}}_{L-1}^T]^T$  is obtained by using the individual solutions,  $\hat{\mathbf{x}}_l$ , of (4.13). More specifically, if  $\lambda_l = \sqrt{2(1+q) \log(PV)}$  for each  $q \geq 0$  is used in (4.13), then the bound holds with probability greater than  $1 - L \left( \sqrt{\pi(1+q) \log(PV)} \cdot (PV)^q \right)^{-1}$ .

*Proof.* Let us define the unobserved measurements  $\mathbf{y}_l = \Phi_l \mathbf{x}_l + \mathbf{e}$ . Note that due to the orthogonality of  $\Phi_l$ s,

$$\begin{aligned} \Phi_l^H (\mathbf{y} - \Phi_l \mathbf{z}_l) &= \Phi_l^H \left( \sum_{l'=0}^{L-1} \Phi_{l'} \mathbf{x}_{l'} + \mathbf{e} - \Phi_l \mathbf{z}_l \right), \\ &= \Phi_l^T (\Phi_l \mathbf{x}_l + \mathbf{e} - \Phi_l \mathbf{z}_l), \\ &= \Phi_l^T (\mathbf{y}_l - \Phi_l \mathbf{z}_l). \end{aligned} \quad (4.17)$$

As a consequence, the  $L$  small Dantzig selectors in (4.13) are equivalent with

$$\min_{\mathbf{z}_l \in \mathbb{C}^{PV}} \|\mathbf{z}_l\|_1 \quad \text{subject to} \quad \|\Phi_l^H (\mathbf{y}_l - \Phi_l \mathbf{z}_l)\|_\infty \leq \lambda_l \cdot \sigma \quad \text{for } l = 0, 1, \dots, L-1 \quad (4.18)$$

Then, denoting the individual solutions of (4.13) as  $\hat{\mathbf{x}}_l$  and assuming  $\|\Phi_l^H \mathbf{e}\|_\infty \leq \lambda_l$ , from [131, Th. 2] we have

$$\|\hat{\mathbf{x}}_l - \mathbf{x}_l\|_2 \leq 4 \frac{\lambda_l \sqrt{k_l} \sigma}{\rho_{4k_l}^2(\Phi_l)}. \quad (4.19)$$

Hence, defining the concatenated estimate as  $\hat{\mathbf{x}} = [\hat{\mathbf{x}}_0^T, \hat{\mathbf{x}}_1^T, \dots, \hat{\mathbf{x}}_{L-1}^T]^T$ , we get

$$\|\hat{\mathbf{x}} - \mathbf{x}\|_2 = \sqrt{\sum_{l=0}^{L-1} \|\hat{\mathbf{x}}_l - \mathbf{x}_l\|_2^2} \leq 4 \sqrt{\sum_{l=0}^{L-1} \frac{\lambda_l^2 k_l \sigma^2}{\rho_{4k_l}^4(\Phi_l)}}. \quad (4.20)$$

□

On the contrary, if we use the original DS in (4.9) to obtain an estimate  $\hat{\mathbf{x}}_{\text{DS}}$ , then using [131, Th. 2] we get

$$\|\hat{\mathbf{x}}_{\text{DS}} - \mathbf{x}\|_2 \leq 4 \frac{\lambda \sqrt{k} \sigma}{\rho_{4k}^2(\Phi)}, \quad (4.21)$$

where  $k = \sum_{l=0}^{L-1} k_l$  and  $\|\Phi^H \mathbf{e}\|_\infty \leq \lambda = \sqrt{2 \log(LPV)}$ . We now have the following theorem:

**Theorem 2.** *The collection of  $L$  small Dantzig selectors in (4.13) performs better than the original Dantzig selector in (4.9) as it has a smaller upper bound on the  $\ell_2$ -norm of the sparse-estimation error:*

$$4 \sqrt{\sum_{l=0}^{L-1} \frac{\lambda_l^2 k_l \sigma^2}{\rho_{4k_l}^4(\Phi_l)}} \leq 4 \frac{\lambda \sqrt{k} \sigma}{\rho_{4k}^2(\Phi)}. \quad (4.22)$$

*Proof.* See Appendix C. □

## 4.4 Adaptive Waveform Design

In this section, we develop an adaptive waveform design technique, based on a multi-objective optimization approach, to improve the detection and estimation performance. From the discussion of the previous section, it follows that we can adaptively design the spectral parameters,  $a_l$ , to minimize the upper bound on the estimation error. Note here that the upper bound on the sparse-estimation error depends solely on the properties of the system matrix  $\Phi$ . However, to achieve better performance it is also essential that the signal parameters adapt to the operational scenario involving dynamic target states and nonstationary environmental conditions. Hence, in addition to minimizing the upper bound on the estimation error, we propose maximizing another utility function based on the squared Mahalanobis-distance, which depends on the target and noise parameters ( $\mathbf{x}$  and  $\Sigma$ ). In the following, we first describe these two single-objective optimization problems and their respective solutions. Then, we discuss the multi-objective optimization method.

### 4.4.1 Minimizing the Error Bound

From (4.11), we first notice that each  $\Phi_l$  can be written as  $\Phi_l = a_l \tilde{\Phi}_l$ , and therefore we have  $\rho_{4k_l}^4(\Phi_l) = a_l^4 \rho_{4k_l}^4(\tilde{\Phi}_l)$ . Then, to minimize the upper bound on the sparse-estimation error, we construct an optimization problem as

$$\mathbf{a}^{(1)} = \arg \min_{\mathbf{a} \in \mathbb{C}^L} \sum_{l=0}^{L-1} \frac{\lambda_l^2 k_l \sigma^2}{a_l^4 \rho_{4k_l}^4(\tilde{\Phi}_l)} \quad \text{subject to } \mathbf{a}^H \mathbf{a} = 1. \quad (4.23)$$

Using the Lagrange-multiplier approach, we can obtain the solution of (4.23) as

$$a_l^{(1)} = \sqrt{\frac{(2\alpha_l)^{1/3}}{\sum_{l=0}^{L-1} (2\alpha_l)^{1/3}}}, \quad \text{for } l = 0, 1, \dots, L-1, \quad (4.24)$$

where  $\alpha_l = \frac{\lambda_l^2 k_l \sigma^2}{\rho_{4k_l}^4(\tilde{\Phi}_l)}$ . However, the computation of  $\rho_{4k_l}(\tilde{\Phi}_l)$  is difficult with the complex variables. Therefore, we use a computable lower bound on  $\rho_{4k_l}(\tilde{\Phi}_l)$ , defined as

$$\rho_{8k_l}(\tilde{\Psi}) \leq \rho_{4k_l}(\tilde{\Phi}_l), \quad (4.25)$$

where

$$\tilde{\Psi}^T \tilde{\Psi} = \begin{bmatrix} \Psi_1^T \Psi_1 + \Psi_2^T \Psi_2 & \mathbf{0} \\ \mathbf{0} & \Psi_1^T \Psi_1 + \Psi_2^T \Psi_2 \end{bmatrix}, \quad \Psi_1 = \text{Re } \tilde{\Phi}_l, \quad \Psi_2 = \text{Im } \tilde{\Phi}_l \quad (4.26)$$

See Appendix D for the details of (4.25). Then, similar to (4.24), we can obtain the adaptive OFDM spectral parameters as

$$a_l^{(1)} = \sqrt{\frac{(2\tilde{\alpha}_l)^{1/3}}{\sum_{l=0}^{L-1} (2\tilde{\alpha}_l)^{1/3}}}, \quad \text{for } l = 0, 1, \dots, L-1, \quad (4.27)$$

where  $\tilde{\alpha}_l = \frac{\lambda_l^2 k_l \sigma^2}{\rho_{8k_l}^4(\tilde{\Psi})}$ .

#### 4.4.2 Maximizing the Mahalanobis-Distance

To decide whether a target is present or not in the range cell under test, the standard procedure is to construct a decision problem to choose between two possible hypotheses: the null hypothesis  $\mathcal{H}_0$  (target-free hypothesis) or the alternate hypothesis  $\mathcal{H}_1$

(target-present hypothesis). The problem can be expressed as

$$\begin{cases} \mathcal{H}_0 : \mathbf{y} = \mathbf{e} \\ \mathcal{H}_1 : \mathbf{y} = \Phi \mathbf{x} + \mathbf{e} \end{cases}. \quad (4.28)$$

Hence, the measurement  $\mathbf{y}$  is distributed as  $\mathbb{C}\mathcal{N}_{LN}(\mathbf{0}, \mathbf{I}_N \otimes \Sigma)$  or  $\mathbb{C}\mathcal{N}_{LN}(\Phi \mathbf{x}, \mathbf{I}_N \otimes \Sigma)$ .

To distinguish between these two distributions, one standard measure is the squared Mahalanobis-distance, defined as

$$\begin{aligned} d^2 &= \mathbf{x}^H \Phi^H (\mathbf{I}_N \otimes \Sigma)^{-1} \Phi \mathbf{x}, \\ &= \sum_{n=0}^{N-1} \mathbf{x}^H \Phi(n)^H \mathbf{A}^H \Sigma^{-1} \mathbf{A} \Phi(n) \mathbf{x}. \end{aligned} \quad (4.29)$$

Then, to maximize the detection performance, we can formulate an optimization problem as

$$\begin{aligned} \mathbf{a}^{(2)} &= \arg \max_{\mathbf{a} \in \mathbb{C}^L} \left[ \sum_{n=0}^{N-1} \mathbf{x}^H \Phi(n)^H \mathbf{A}^H \Sigma^{-1} \mathbf{A} \Phi(n) \mathbf{x} \right], \\ &\text{subject to } \mathbf{a}^H \mathbf{a} = 1. \end{aligned} \quad (4.30)$$

Since

$$\begin{aligned} \mathbf{x}^H \Phi(n)^H \mathbf{A}^H \Sigma^{-1} \mathbf{A} \Phi(n) \mathbf{x} &= \text{tr}(\mathbf{x}^H \Phi(n)^H \mathbf{A}^H \Sigma^{-1} \mathbf{A} \Phi(n) \mathbf{x}), \\ &= \text{tr}(\Sigma^{-1} \mathbf{A} \Phi(n) \mathbf{x} \mathbf{x}^H \Phi(n)^H \mathbf{A}^H), \end{aligned}$$

we can apply the theorem of Appendix B to rewrite the optimization problem as

$$\begin{aligned} \mathbf{a}^{(2)} &= \arg \max_{\mathbf{a} \in \mathbb{C}^L} \mathbf{a}^H \left[ \sum_{n=0}^{N-1} (\Phi(n) \mathbf{x} \mathbf{x}^H \Phi(n)^H)^T \odot \Sigma^{-1} \right] \mathbf{a}, \\ &\text{subject to } \mathbf{a}^H \mathbf{a} = 1. \end{aligned} \quad (4.31)$$

Hence, the optimization problem reduces to a simple eigenvalue-eigenvector problem, and the solution of (4.31) is the eigenvector corresponding to the largest eigenvalue of  $\left[ \sum_{n=0}^{N-1} (\Phi(n) \mathbf{x} \mathbf{x}^H \Phi(n)^H)^T \odot \Sigma^{-1} \right]$ .

### 4.4.3 Multi-Objective Optimization

From the discussions of previous subsections, we notice that if the solution of (4.27) is used one would achieve an efficient sparse-estimation result. Alternatively, solving (4.31) we might get improved performance of the underlying detection problem. Hence, based on these arguments, we devise a constrained MOO problem to design the spectral parameters of the OFDM waveform,  $a_l$ , such that the upper bound on the sparse-estimation error is minimized and the squared Mahalanobis-distance of the detection problem is simultaneously maximized. Mathematically, this is represented as

$$\mathbf{a}_{\text{opt}} = \left\{ \begin{array}{l} \arg \min_{\mathbf{a} \in \mathbb{C}^L} \sum_{l=0}^{L-1} \frac{\lambda_l^2 k_l \sigma^2}{a_l^4 \rho_{8k_l}^4(\tilde{\Psi})}, \\ \arg \max_{\mathbf{a} \in \mathbb{C}^L} \mathbf{a}^H \left[ \sum_{n=0}^{N-1} (\Phi(n) \mathbf{x} \mathbf{x}^H \Phi(n)^H)^T \odot \Sigma^{-1} \right] \mathbf{a} \end{array} \right\}, (4.32)$$

subject to  $\mathbf{a}^H \mathbf{a} = 1$ .

We employ the standard nondominated sorting genetic algorithm II (NSGA-II) [70] to solve our MOO problem, imposing a restriction on the solutions to satisfy the constraint  $\mathbf{a}^H \mathbf{a} = 1$ . The use of NSGA-II provides us with multiple Pareto-optimal solutions in a single run.

## 4.5 Numerical Results

In this section, we present the results of several numerical examples to illustrate the sparse-estimation performance for a target-detection problem and to demonstrate the performance improvement due to the adaptive OFDM waveform design technique. First, we provide a description of the simulation setup and then discuss different numerical examples.

Fig. 4.2 schematically describes a scenario that we used in the simulations. For simplicity, we again considered a 2D scenario, where both the radar and target were in the same plane. Our analyses can easily be extended to 3D scenarios. The details of the target and radar parameters are as follows:

- Target and multipath parameters:
  - Throughout a given CPI, the target remained within a particular range cell. We simulated the situation of a range cell at a distance of 3 km from the radar (positioned at the origin).
  - The target was 13.5 m east from the center line, moving with velocity  $\mathbf{v} = (35/\sqrt{2})(\hat{i} + \hat{j})$  m/s.
  - There were two different paths between the target and radar: one direct and one reflected, subtending angles of  $0.26^\circ$  and  $0.51^\circ$ , respectively, with respect to the radar.
  
- Radar parameters:
  - Carrier frequency  $f_c = 1$  GHz.
  - Available bandwidth  $B = 100$  MHz.



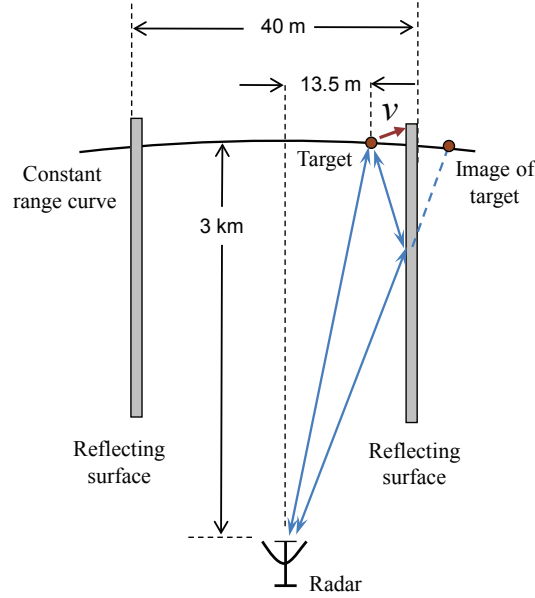


Figure 4.2: A schematic representation of the multipath scenario considered in the numerical examples.

- Number of OFDM subcarriers  $L = 3$ .
- Subcarrier spacing of  $\Delta f = B/(L + 1) = 25$  MHz.
- Pulse width  $T = 1/\Delta f = 40$  ns.
- Pulse repetition interval  $T_p = 4$  ms.
- Number of coherent pulses  $N = 20$ .
- All the transmit OFDM weights were equal; i.e.,  $a_l = 1/\sqrt{L} \forall l$ .

To apply a sparse estimation approach, we partitioned the signal paths and target velocities into  $P = 5$  and  $V = 3$  uniform grid points. We considered signal paths that subtended angles of  $\{-0.5^\circ, -0.25^\circ, 0^\circ, 0.25^\circ, 0.5^\circ\}$  with respect to the radar and target velocities of  $\{25, 35, 45\}$  m/s. Hence, according to our description in Section 4.2.1, we had  $k_l = 2 \forall l$  and  $k = 6$ . We generated the noise samples from a  $\mathcal{CN}(0, 1)$  distribution, and then scaled the samples to satisfy the required target to

clutter-plus-noise ratio (TCNR), defined as

$$\text{TCNR} = \frac{\mathbf{x}^H \mathbf{x}}{N L \sigma_0^2}. \quad (4.33)$$

Here we kept the clutter-plus-noise power same across all the subcarriers by considering  $\Sigma = \sigma_0^2 \mathbf{I}_L$ . The scattering coefficients of the target,  $\mathbf{x}$ , were varied to simulate different operational scenarios, the details of which are described later.

We analyzed the performance characteristics of our proposed technique in terms of the following two measures:

- Root mean squared error (RMSE): Since we applied a sparse estimation approach, the standard performance measure is given by the RMSE of the estimated vector with respect to the true sparse vector, i.e.,  $\|\hat{\mathbf{x}} - \mathbf{x}\|_2$ . We performed Monte Carlo simulations of 100 independent trials and averaged the results to obtain the RMSE values.
- Empirical ROC: Since the underlying task was a target-detection problem, we also computed an empirical ROC to characterize our method. In our simulations, out of the total  $LPV = 45$  grid points,  $k = 6$  grid points contained the target responses, and the remaining  $(LPV - k) = 39$  grid points did not have target responses. After each Monte Carlo run, we noted the number of grid points,  $n_T$ , that corresponds to the estimated target response. Out of these  $n_T$  grid points, if  $n_D$  grid points lie within the set of true 6 grid points and if  $n_{FA} = (n_T - n_D)$  lie within the remaining 39 grid points, then we can define the empirical probabilities of false alarm ( $P_{FA}$ ) and detection ( $P_D$ ) as

$$P_{FA} = \frac{n_{FA}}{LPV - k}, \quad P_D = \frac{n_D}{k}. \quad (4.34)$$

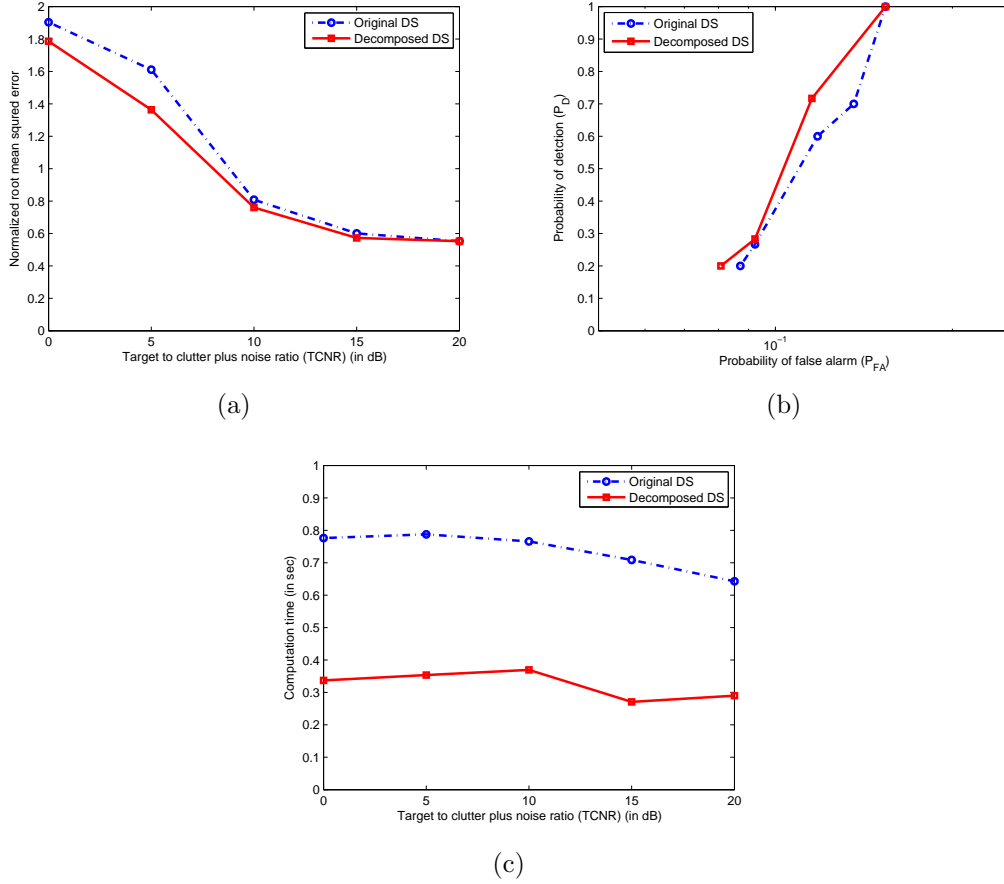


Figure 4.3: Comparison of performances of the standard Dantzig selector and decomposed Dantzig selector to detect Target 1 in terms of the (a) normalized RMSE, (b) empirical ROC, and (c) computation time with respect to the target to clutter-plus-noise ratio.

Finally, we averaged the results over 100 independent Monte Carlo runs to plot the empirical ROC.

## Estimation and Detection Performance

We considered two different targets in our simulations. Target 1 had equal scattering responses across all the subcarriers; i.e.,  $x_{i,d}^{(1)} = [1, 1, 1]^T$  and  $x_{i,r}^{(1)} = [0.5, 0.5, 0.5]^T$  were

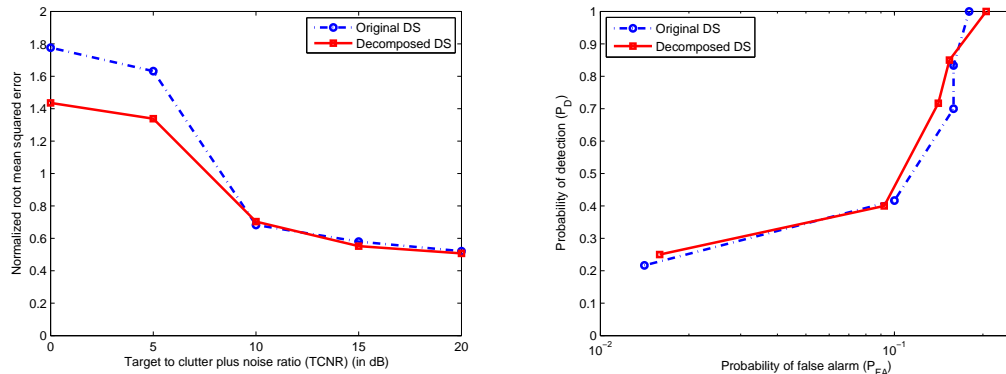
the scattering coefficients of Target 1 along the direct and reflected paths, respectively. For Target 2, we considered varying responses over different subcarriers; i.e.,  $x_{l,d}^{(2)} = [4, 1, 2]^T$  and  $x_{l,r}^{(2)} = [2, 0.5, 2]^T$ . Figs. 4.3 and 4.4 show the performance characteristics of Target 1 and Target 2, respectively, at different TCNR values. We employed both the standard DS of (4.9) and our decomposed DS of (4.13) to reconstruct the sparse vector. We noticed that the decomposed DS performs better than the standard DS both in terms of normalized RMSE and empirical ROC, although the improvement is not huge, apart from the low TCNR conditions. However, we got a drastic reduction in computation time (less than half of that required by the standard DS) when we used the decomposed DS.

## Adaptive Waveform Design

To study the improvement in performance due to the adaptive waveform design techniques, we separately considered both the single-objective optimization problems in (4.27) and (4.31), and the multi-objective optimization method in (4.32) for two different targets.

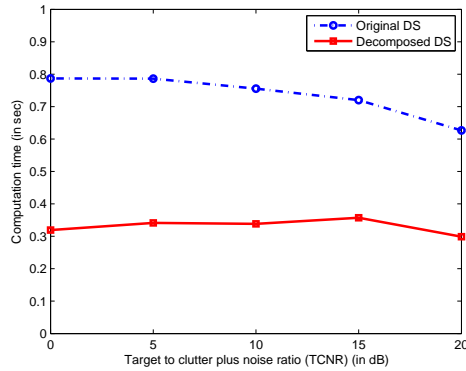
Minimizing the upper bound on the sparse-estimation error, i.e., as a solution of (4.27), yielded  $\mathbf{a}^{(1)} = [0.54, 0.16, 0.83]$ . This solution depends only on the properties of the system matrix  $\Phi$ . It implies that we can expect an improved performance due to the use of this  $\mathbf{a}^{(1)}$  irrespective of the target and noise parameters, which is evident from Figs. 4.7 and 4.8 for Targets 1 and 2, respectively.

In (4.31), the matrix  $\left[ \sum_{n=0}^{N-1} (\Phi(n) \mathbf{x} \mathbf{x}^H \Phi(n)^H)^T \odot \Sigma^{-1} \right]$  became diagonal due to the choice of  $\Sigma = \sigma_0^2 \mathbf{I}_L$ . Therefore, the eigenvector corresponding to the largest eigenvalue had only one entry equal to 1 with all others 0. For example, in the



(a)

(b)



(c)

Figure 4.4: Comparison of performances of the standard Dantzig selector and decomposed Dantzig selector to detect Target 2 in terms of the (a) normalized RMSE, (b) empirical ROC, and (c) computation time with respect to the target to clutter-plus-noise ratio.

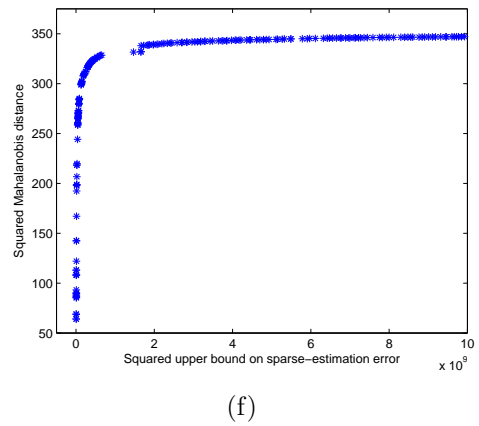
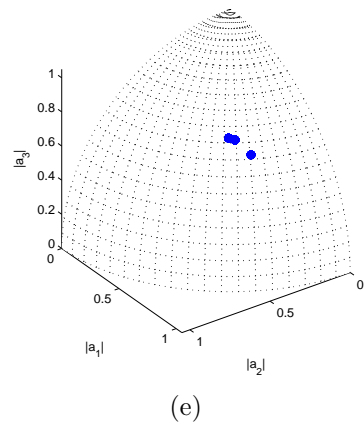
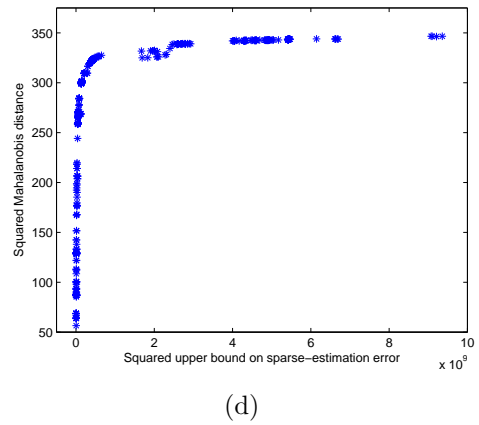
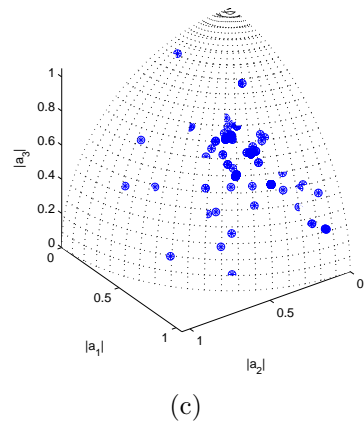
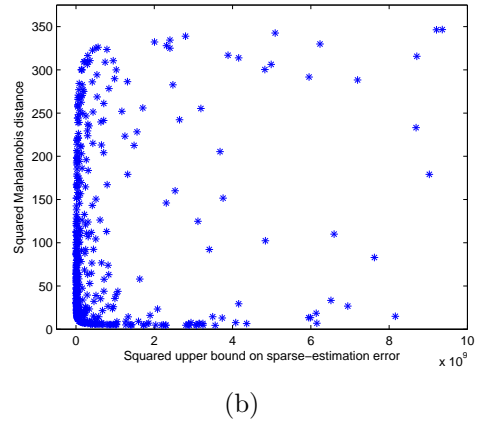
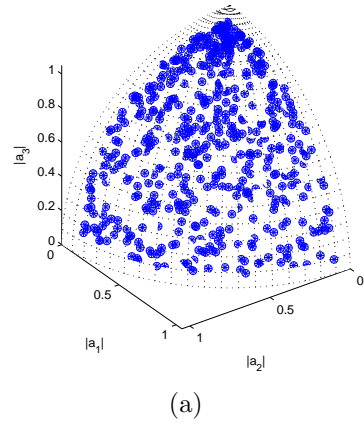


Figure 4.5: Results of the NSGA-II for Target 1: (a), (b) optimal solutions and values of the objective functions at the 0-th generation; (c), (d) optimal solutions and values of the objective functions at the 5-th generation; and (e), (f) optimal solutions and values of the objective functions at the 50-th generation.

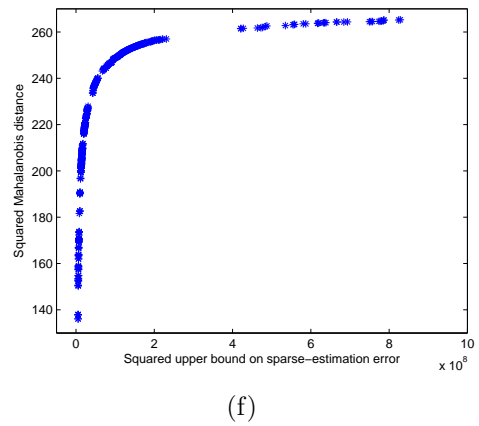
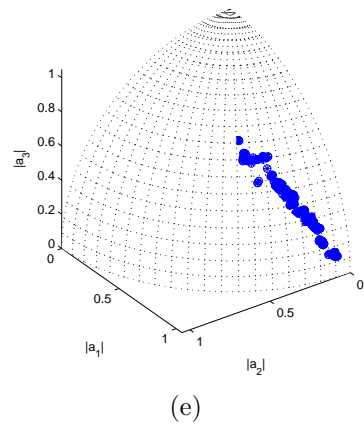
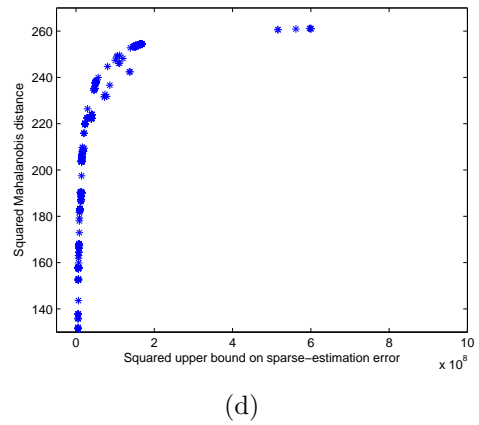
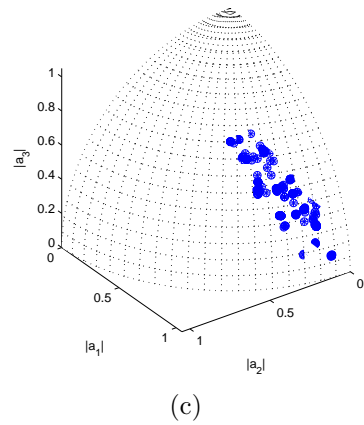
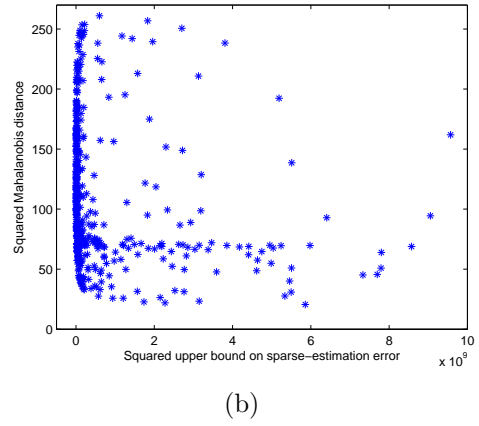
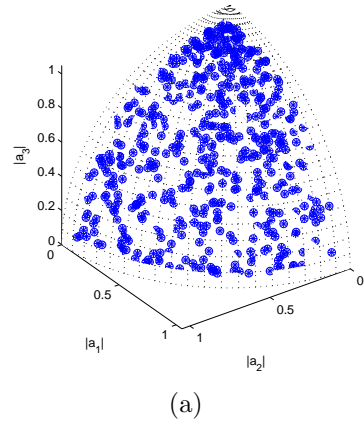


Figure 4.6: Results of the NSGA-II for Target 2: (a), (b) optimal solutions and values of the objective functions at the 0-th generation; (c), (d) optimal solutions and values of the objective functions at the 5-th generation; and (e), (f) optimal solutions and values of the objective functions at the 50-th generation.

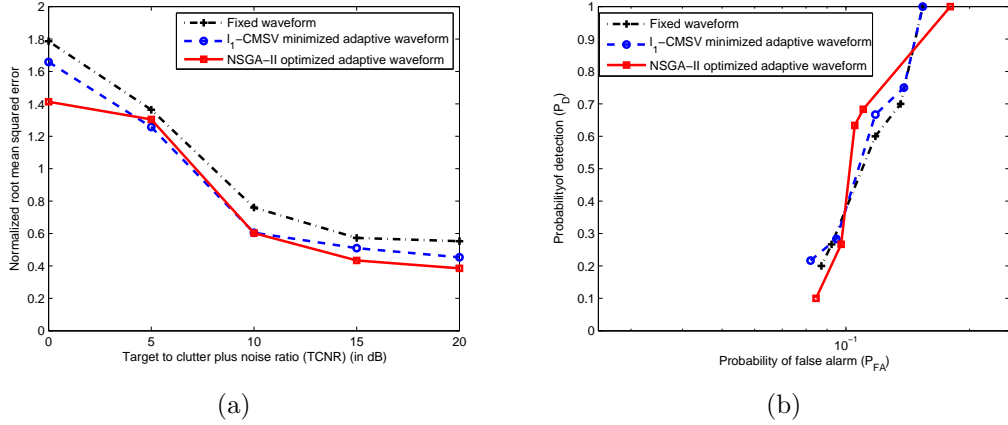


Figure 4.7: Comparison of performances due to the fixed and adaptive waveforms to detect Target 1 in terms of the (a) normalized RMSE and (b) empirical ROC with respect to the target to clutter-plus-noise ratio.

case of Target 1, all the diagonal entries were equal, and so the solution of (4.31) could be either  $\mathbf{a}^{(2)} = [1, 0, 0]^T$  or  $[0, 1, 0]^T$  or  $[0, 0, 1]^T$ . For Target 2, which had a stronger reflection along the first subcarrier, the solution of (4.31) was  $\mathbf{a}^{(2)} = [1, 0, 0]^T$ . To check whether the solution of (4.31) puts all the transmitted energy along the subcarrier that has the strongest target reflection energy, we devised Target 3 to have reflection coefficients  $x_{l,d}^{(3)} = [1, 10, 1]^T$  and  $x_{l,r}^{(3)} = [0.5, 5, 0.5]^T$ , and found the optimal solution to be  $\mathbf{a}^{(2)} = [0, 1, 0]^T$ . Hence, we concluded that the maximization of the Mahalanobis distance provided an adaptive waveform with all the signal energy transmitted over a single subcarrier that had the strongest target response. However, while doing so, we were effectively using a single-carrier waveform that could not provide any frequency diversity. Therefore, we did not analyze the performance of our system with this type of adaptive waveform.

To solve the MOO problem (4.32), we employed the NSGA-II with the following parameters: population size = 500, number of generations = 50, crossover probability = 0.9, and mutation probability = 0.1. We applied the constraint  $\mathbf{a}^H \mathbf{a} = 1$



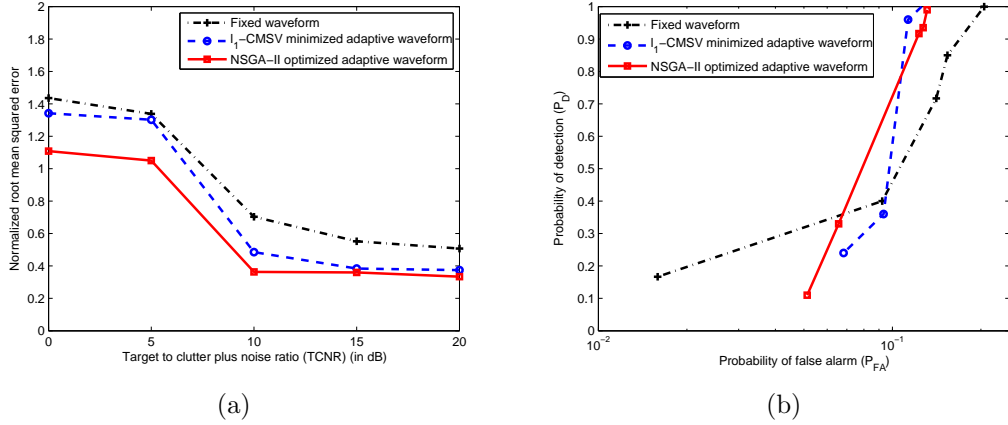


Figure 4.8: Comparison of performances due to the fixed and adaptive waveforms to detect Target 2 in terms of the (a) normalized RMSE and (b) empirical ROC with respect to the target to clutter-plus-noise ratio.

in a relaxed way by ensuring that the solutions satisfy  $0.999 \leq \mathbf{a}^H \mathbf{a} \leq 1.001$ . We plotted the results of the optimal solutions and corresponding values of the two objective functions (at three different generations) in Figs. 4.5 and 4.6 for Targets 1 and 2, respectively. The constraint  $\mathbf{a}^H \mathbf{a} = 1$  ensured that all the solutions could be represented on the surface of a sphere, restricted to the first octant, when  $|a_{1_{\text{opt}}}|$ ,  $|a_{2_{\text{opt}}}|$ , and  $|a_{3_{\text{opt}}}|$  constitute the axes in Cartesian coordinates. We further noticed that the solutions reached the optimal Pareto-front very quickly. By the end of the 5-th generation, almost all the solutions resided on or close to the Pareto-front. We took one of the solutions from the Pareto front after the 50-th generation (e.g.,  $\mathbf{a}_{\text{opt}} = [0.60, 0.40, 0.70]^T$  for Target 1 and  $\mathbf{a}_{\text{opt}} = [0.98, 0.11, 0.17]^T$  for Target 2) and evaluated the performance characteristics of our system. The results are shown in Figs. 4.7 and 4.8 for Targets 1 and 2, respectively. We observed that due to its dependence on the target parameters the NSGA-II optimized waveform,  $\mathbf{a}_{\text{opt}}$ , performed better than both the  $\ell_1$ -CMSV-based adaptive waveform,  $\mathbf{a}^{(1)}$ , and a fixed waveform having  $a_l = 1/\sqrt{L} \forall l$ .

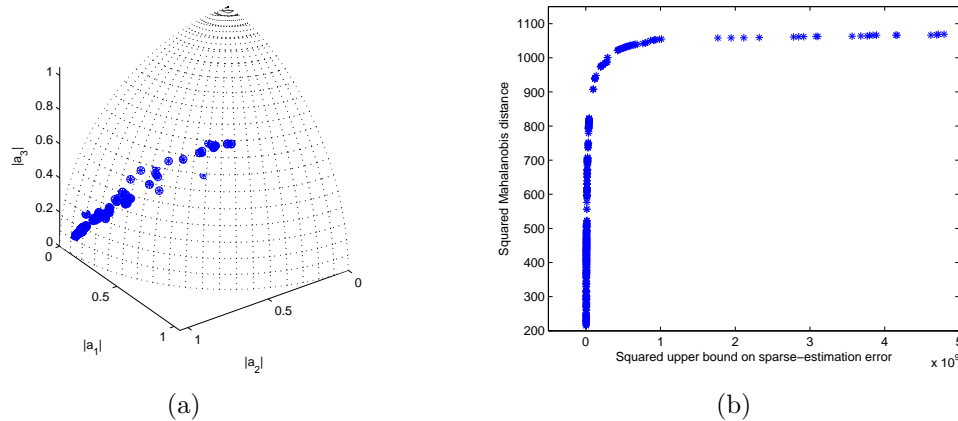


Figure 4.9: Results of the NSGA-II for Target 3: (a), (b) optimal solutions and values of the objective functions at the 50-th generation.

From the results of the MOO problem, we could also understand that there is some relationship between the energy distribution of the optimal waveform,  $\mathbf{a}_{\text{opt}}$ , and that of the target response,  $\mathbf{x}$ , along different subcarriers. To investigate further, we took the average over the whole population of 500 solutions and found  $\mathbf{a}_{\text{opt,avg}} = [0.61, 0.39, 0.68]^T$  for Target 1 and  $\mathbf{a}_{\text{opt,avg}} = [0.88, 0.20, 0.36]^T$  for Target 2. Though it was not clear for Target 1, from the results of Target 2 we observed that the averaged energy-distribution of the optimal waveform across different subcarriers were in proportion to the energy-distribution of the target. As further confirmation, we ran the NSGA-II for Target 3 as well. Fig. 4.9 depicts the optimal solutions and corresponding values of the objective functions at the end of the 50-th generation. In this case, the average over all 500 solutions was  $\mathbf{a}_{\text{opt,avg}} = [0.13, 0.96, 0.15]^T$ . Hence, in general, we can conclude that the solution of the MOO distributes the energy of the optimal waveform across different subcarriers in proportion to the distribution of the target energy; i.e., it puts more signal energy into that particular subcarrier in which the target response is stronger. Since in our simulation we kept the noise power fixed and varied only the target energies over different subcarriers, we can extend our

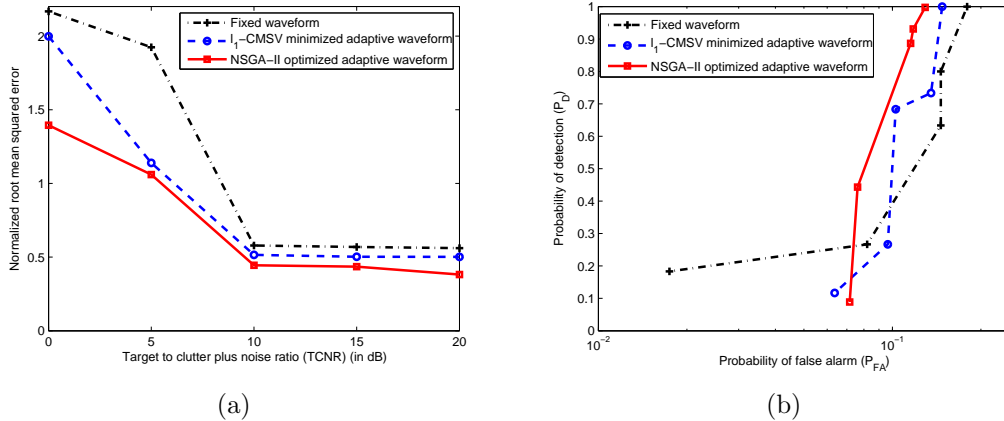


Figure 4.10: Comparison of performances due to the fixed and adaptive waveforms to detect Target 3 in terms of the (a) normalized RMSE and (b) empirical ROC with respect to the target to clutter-plus-noise ratio.

conclusion by drawing synonymity between the target energy and TCNR value. In Fig. 4.10, we also demonstrated the performance of our system for Target 3 using fixed and adaptive waveforms.

## 4.6 Summary

We proposed a multi-objective optimization technique to design the spectral parameters of the OFDM signal for detecting a moving target in the presence of multipath reflections. We first developed a sparse measurement model that accounts for the target returns over all possible signal paths and target velocities. To estimate the sparse vector, we employed a collection of multiple small Dantzig selectors that exploit more prior structures of the sparse vector than the standard DS. Then, we proposed a criterion to optimally design the spectral parameters of the transmitting

OFDM waveform by solving a constrained MOO problem, which simultaneously optimizes two objective functions: minimizing the upper bound on the estimation error to improve the efficiency of sparse-recovery and maximizing the squared Mahalanobis-distance to increase the performance of the underlying detection problem. When the noise powers over different subcarriers were the same, we inferred that the solution of the MOO distributes the energy of the optimal waveform across different subcarriers in proportion to the distribution of the target energy.

In the next chapters, we study the usage of an adaptive OFDM radar for tracking problems: single-target tracking in low-grazing angle scenarios and multi-target tracking by exploiting the inherent delay-Doppler sparsity.

# Chapter 5

## Target Tracking in Low-Grazing Angle Scenarios<sup>4</sup>

In this chapter, we propose an information theoretic waveform design algorithm for target tracking in a low-grazing angle (LGA) scenario [71] – [73]. To develop an accurate tracking method, we incorporate realistic physical and statistical effects, such as the earth’s curvature, vertical refractivity gradient of the lower atmosphere, and compound-Gaussian characteristics of sea-clutter, into our model. We employ a co-located multiple-input multiple-output (MIMO) radar configuration [79] using a wideband OFDM signalling scheme. Additionally, we use polarization-sensitive transceivers to resolve the multipath signals with small separation angles [80], [81]. We apply a sequential Monte Carlo method (particle filter) to track the target. Our tracker works in a closed-loop fashion with an integrated optimal waveform design technique based on maximum mutual information criterion [85].

---

<sup>4</sup>Based on S. Sen and A. Nehorai, “OFDM MIMO radar with mutual-information waveform design for low-grazing angle tracking,” *IEEE Trans. Signal Process.*, vol. 58, no. 6, pp. 3152-3162, Jun. 2010. ©[2010] IEEE.

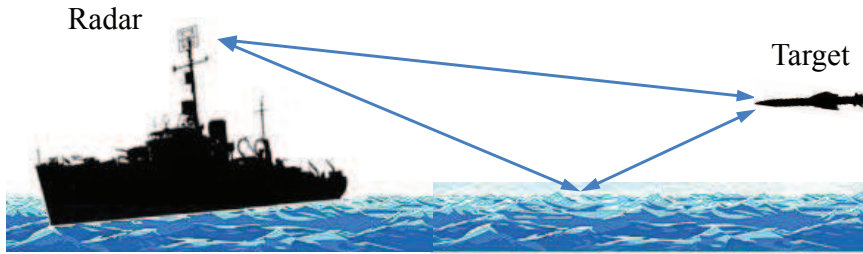


Figure 5.1: Low-grazing angle tracking is a challenging problem in maritime applications.

## 5.1 Introduction

Tracking targets in an LGA scenario [71] – [73] is one of the most challenging problems in radar. To develop an accurate tracking method, it is important to incorporate the underlying physical phenomena. In an LGA scenario, the radar measurements are affected by many factors [153] – [155], such as the ever-changing meteorological conditions in the troposphere (the lowest portion of earth’s atmosphere), curved surface of the earth, roughness of the sea-surface, etc. Therefore, the challenge is to consider these complex physical behaviors as realistically as possible, yet keep the model amenable to signal processing. In this work, we consider the effects of both the earth’s curvature and linear refractivity gradient of the horizontally stratified atmosphere [153] while modeling specular multipath signals. The randomly reflected returns (clutter), which also depend on the transmitted signal [113], are statistically modeled as a compound-Gaussian process [77], [78].

Furthermore, to resolve the specular multipath components, it is useful to use short pulse, multi-carrier wideband radar signals [71], [156], [157]. Therefore, we employ an OFDM signalling scheme, which is one of the ways to accomplish simultaneous use of

several subcarriers. The frequency diversity of OFDM also provides richer information about the target. To achieve such waveform diversity, we employ a co-located MIMO radar configuration [79], with each transmitter operating at one of the OFDM subcarrier frequencies. Additionally, in [80], [81], it is shown that polarization allows identification of correlated source signals (e.g., multipath) with small separation angles. Hence, we include polarization-sensitive transceivers in this work.

To track the target we use a sequential Monte Carlo method (particle filter) [82] – [84], which is known to be effective for solving nonlinear and non-Gaussian Bayesian inference problems. In addition to target position and velocities, we also track the polarimetric parameters of the target at different frequencies. However, in contrast to the conventional open-loop tracker, we integrate the tracking procedure with an information theoretic waveform design algorithm. The idea of combining a waveform design procedure into a radar tracking system was first introduced in [158]. This type of integration (closed-loop system) enables us to achieve better tracking performance by matching the waveform with the operational scenario involving dynamic target states and nonstationary environmental conditions.

We propose the waveform design criterion based on mutual information (MI) [85] between the state and measurement vectors. The choice of MI criterion provides a computationally more efficient approach than the posterior Cramér-Rao bound based waveform design technique [113]. We select the optimal OFDM waveform at the  $k$ -th pulse interval to maximize the MI between the state and measurement vectors at the  $(k + 1)$ -th pulse interval, utilizing all the measurement history up to  $k$ -th pulse. Furthermore, the computation of our MI criterion does not depend on the specific value of the measurement at the  $(k + 1)$ -th pulse duration; see also [159], [160]. This makes our algorithm more practical. Our numerical examples demonstrate

the importance of realistic physical modeling, effects of frequency diversity through the OFDM MIMO configuration, and achieved performance improvements due to adaptive OFDM waveform design.

## 5.2 Tropospheric Propagation Models

In vacuum or free space, the refractive index  $n$  of the medium remains constant, and therefore the rays traced by electromagnetic (EM) waves travel in straight lines. This type of situation may happen only under very stable atmospheric conditions and at sufficiently high altitude. However, in LGA scenarios, both the curvature of the earth and variability of the refractive index affect the EM propagation. According to [153], for frequencies less than 10 GHz, the variation of the refractive index with other physical parameters of the atmosphere can be represented as

$$N = 10^6(n - 1) = 77.6 \frac{P}{T} + (3.73 \times 10^5) \frac{e}{T^2}, \quad (5.1)$$

where  $N$  is called the radio refractivity;  $P$  and  $e$  are the total atmospheric pressure and partial pressure of the water vapor in millibars; and  $T$  is the absolute temperature in degrees Kelvin. Since these atmospheric effects take place at the molecular scale, it is noted that  $N$  remains independent of frequency and polarization up to at least 15 GHz [155].

In normal atmospheric conditions, the pressure decreases exponentially with height, which primarily causes a reduction in the value of  $N$  with respect to height  $h$ . For the *standard* atmosphere, the gradient of such variation is considered to be  $-79 \leq dN/dh \leq 0$   $N$ -units/km [154]. Under this condition, a radio ray will diffract



downward, but with a curvature less than earth's radius. Apart from this standard (normal) atmosphere, there are *substandard* (worse than normal) and *superstandard* (better than normal) propagation conditions corresponding to  $dN/dh \geq 0$  and  $-157 \leq dN/dh \leq -79$  N-units/km, respectively [154, Table 1].

Furthermore, in a maritime environment, due to the strong humidity gradients immediately above (within first few meters) the air-sea boundary, one may find an *evaporation duct*, in which  $dN/dh \leq -157$  N-units/km [154]. This makes a radio ray bend downward with a curvature more than earth's radius and ultimately creates a trapping layer like a waveguide. Therefore, only certain modes of EM waves satisfying the required boundary conditions can propagate through such layers even beyond the radio horizon. The frequencies of such modes depend strongly on the existing duct height, with a practical lower limit of about 3 GHz [161]. The evaporation duct heights are in turn highly variable in space and time, depending on a number of factors including the temperature difference between the air and sea, and the wind speed [162], [163]. Various other effects and experimental results related to the evaporation duct on radar and communication have been discussed in [164] – [168].

In addition to these atmospheric effects, LGA propagations are affected also by the fact that the earth is curved. The curvature of the earth decreases the path length difference between the direct and reflected waves, and it also reduces the amplitude of the reflected waves [169]. The classical way to deal with this problem is to replace the actual earth with radius  $a = 6378.1$  km with an imaginary flat earth with equivalent radius

$$a_e = a \left( 1 + a \frac{dN}{dh} 10^{-6} \right)^{-1}. \quad (5.2)$$

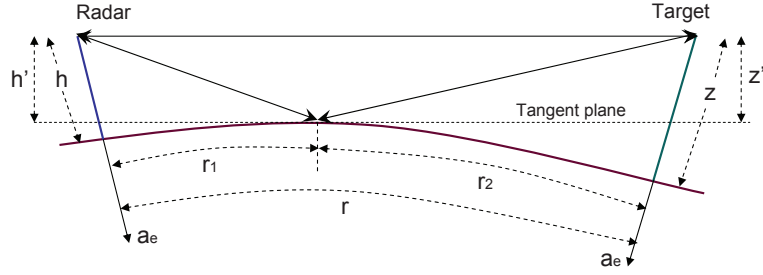


Figure 5.2: Equivalent representations of curved and flat earth models.

Then, for any two points at heights  $h$  and  $z$  and separated from each other by ground distance  $r$ , as shown in Fig. 5.2, we can write an equivalent version of the modified heights over the flat-earth model as [169], [170]

$$h' \simeq h - \frac{r_1^2}{2a_e}, \quad (5.3)$$

$$z' \simeq z - \frac{(r - r_1)^2}{2a_e}, \quad (5.4)$$

where the point of reflection  $r_1$  is evaluated by solving the following cubic equation [153]

$$2r_1^3 - 3rr_1^2 + [r^2 - 2a_e(h + z)]r_1 + 2a_ehr = 0. \quad (5.5)$$

Here, if  $h$  denotes the height of a radar, then from (5.3) we can also compute the radar horizon,  $r_h$ , by equating  $h'$  to zero [153], [169]; i.e.,

$$r_h = \sqrt{2a_e h}. \quad (5.6)$$

In the rest of the chapter, whenever we mention  $h'$  and  $z'$  we implicitly mean that we use the equivalent flat-earth transformations given in (5.3) and (5.4).

## 5.3 Problem Description and Modeling

In this section, we first present a dynamic state model for target tracking. In the state vector we include target position, velocity, and scattering coefficients at different frequencies. Then, we develop an OFDM MIMO radar signal model accounting for polarimetric measurements over multiple frequencies.

### 5.3.1 Dynamic State Model

We consider the position, velocity, and scattering parameters at different frequencies of the target into our state model. The scattering matrix of the target at a particular frequency can be represented as

$$\mathbf{X}_l^t = \begin{bmatrix} x_l^{\text{hh}} & x_l^{\text{hv}} \\ x_l^{\text{vh}} & x_l^{\text{vv}} \end{bmatrix}, \quad (5.7)$$

where  $x_l^{\text{hv}}$  is the complex scattering coefficient of the target in the horizontally polarized component of the received signal due to the vertically polarized component of the transmitted signal at the  $l$ -th frequency; similarly for the other quantities. From Huynen's work [171], we also know that

$$\mathbf{X}_l^t \triangleq \mathbf{U}_l^* \mathbf{D}_l \mathbf{U}_l^H, \quad (5.8)$$

where

- $\mathbf{U}_l$  is a unitary matrix

$$\mathbf{U}_l = \begin{bmatrix} \cos \vartheta_l & -\sin \vartheta_l \\ \sin \vartheta_l & \cos \vartheta_l \end{bmatrix} \begin{bmatrix} \cos \varepsilon_l & j \sin \varepsilon_l \\ j \sin \varepsilon_l & \cos \varepsilon_l \end{bmatrix}, \quad (5.9)$$

where  $\vartheta_l$  is the orientation angle of the target ellipse at the  $l$ -th frequency with respect to line of sight and relative to the radar ( $-90^\circ \leq \vartheta_l \leq 90^\circ$ );  $\varepsilon_l$  is the ellipticity of the target at the  $l$ -th frequency ( $-45^\circ \leq \varepsilon_l \leq 45^\circ$ ) [172].

- $\mathbf{D}_l$  is a diagonal matrix

$$\mathbf{D}_l = m_l e^{j\varrho_l} \begin{bmatrix} e^{j\varsigma_l} & 0 \\ 0 & e^{-j\varsigma_l} \tan^2 \varpi_l \end{bmatrix}, \quad (5.10)$$

where  $m_l$  is the maximum target amplitude at the  $l$ -th frequency (representing an overall measure of target RCS);  $\varrho_l$  is the absolute phase of the scattering matrix at the  $l$ -th frequency ( $-180^\circ \leq \varrho_l \leq 180^\circ$ );  $\varsigma_l$  is called the target skip angle at the  $l$ -th frequency ( $-45^\circ \leq \varsigma_l \leq 45^\circ$ ); and  $\varpi_l$  is called the target characteristic angle at the  $l$ -th frequency ( $0^\circ \leq \varpi_l \leq 45^\circ$ ) [172].

In general, all of these six target variables  $\vartheta_l$ ,  $\varepsilon_l$ ,  $m_l$ ,  $\varrho_l$ ,  $\varsigma_l$ , and  $\varpi_l$  are functions of frequency and aspect direction [171].

Considering a target at position  $(x, y, z)$  and moving with velocity  $\mathbf{v} (= \dot{x}\hat{i} + \dot{y}\hat{j} + \dot{z}\hat{k})$ , we construct the state vector as follows:

$$\boldsymbol{\zeta} = [x, y, z, \dot{x}, \dot{y}, \dot{z}, \boldsymbol{\vartheta}^T, \boldsymbol{\varepsilon}^T, \mathbf{m}^T, \boldsymbol{\varrho}^T, \boldsymbol{\varsigma}^T, \boldsymbol{\varpi}^T]^T, \quad (5.11)$$

where  $\boldsymbol{\vartheta} = [\vartheta_1, \dots, \vartheta_L]^T$ ,  $\boldsymbol{\varepsilon} = [\varepsilon_1, \dots, \varepsilon_L]^T$ ,  $\mathbf{m} = [m_1, \dots, m_L]^T$ ,  $\boldsymbol{\varrho} = [\varrho_1, \dots, \varrho_L]^T$ ,  $\boldsymbol{\varsigma} = [\varsigma_1, \dots, \varsigma_L]^T$ , and  $\boldsymbol{\varpi} = [\varpi_1, \dots, \varpi_L]^T$ .

Assuming constant velocity movement, we obtain a linear dynamic state equation at the  $k$ -th pulse duration as

$$\boldsymbol{\zeta}_k = \begin{bmatrix} \begin{bmatrix} \mathbf{I}_3 & T_p \mathbf{I}_3 \\ \mathbf{0} & \mathbf{I}_3 \end{bmatrix} & \mathbf{0} \\ \mathbf{0} & \mathbf{I}_{6L} \end{bmatrix} \boldsymbol{\zeta}_{k-1} + \mathbf{w}_k, \quad \text{for } k = 1, 2, \dots, \quad (5.12)$$

where  $T_p$  denotes the PRI and  $\mathbf{w}$  represents the state noise. In this model, we consider that the scattering coefficients of the target are almost constant temporally. This is true, for example, when the target is far away from the radar. We assume  $\mathbf{w}$  to be a zero-mean Gaussian distributed random vector with covariance matrix [173, Ch. 6.2.2]

$$\boldsymbol{\Sigma}_{\mathbf{w}} = \begin{bmatrix} q_{pv} \begin{bmatrix} \frac{T_p^3}{3} \mathbf{I}_3 & \frac{T_p^2}{2} \mathbf{I}_3 \\ \frac{T_p^2}{2} \mathbf{I}_3 & T_p \mathbf{I}_3 \end{bmatrix} & \mathbf{0} \\ \mathbf{0} & q_{scat} \mathbf{I}_{6L} \end{bmatrix},$$

where  $q_{pv}$  and  $q_{scat}$  are constants. Hence, the position and velocity of the target are statistically independent of the scattering coefficients.

### 5.3.2 Measurement Model

We consider a linear array of  $L$  transceivers forming an  $L \times L$  co-located MIMO configuration. Each of the transceivers is positioned at  $(0, 0, h_l)$ ,  $l = 0, 1, \dots, L - 1$ , and transmits a carrier frequency  $f_l$  forming an OFDM signal. Each of the transceivers

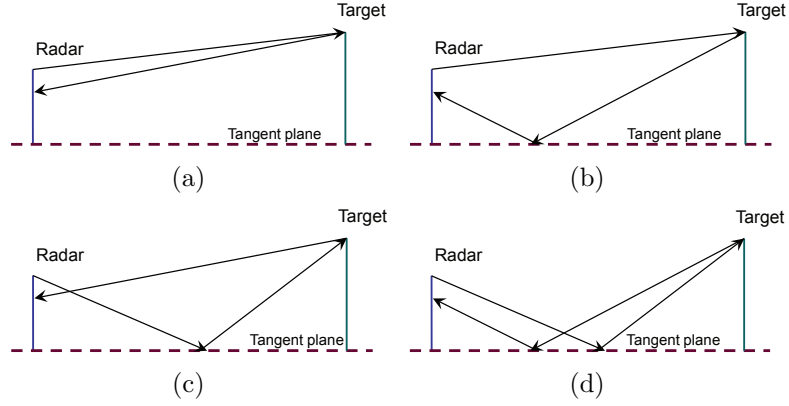


Figure 5.3: (a) Direct-direct, (b) direct-reflected, (c) reflected-direct, and (d) reflected-reflected signal paths.

is capable of transmitting and receiving polarized signals. We formulate the complex envelope of the signal at the  $j$ -th receiver due to the  $i$ -th transmitter during the  $k$ -th pulse duration as a summation of three terms:

$$\mathbf{y}_{ij}(t, \boldsymbol{\zeta}_k) = \boldsymbol{\mu}_{ij}(t, \boldsymbol{\zeta}_k) + \mathbf{c}_{ij}(t) + \mathbf{e}_{ij}(t), \text{ for } i, j = 0, \dots, L - 1, t = 0, \dots, N - 1 \quad (5.13)$$

where  $\boldsymbol{\mu}_{ij}(t, \boldsymbol{\zeta}_k)$  represents a coherent sum of the direct and specularly reflected signals (see Fig. 5.3), and it depends on the target state vector  $\boldsymbol{\zeta}_k$ ;  $\mathbf{c}_{ij}(t)$  represents the clutter, comprising of any randomly reflected returns within the time-span of interest;  $\mathbf{e}_{ij}(t)$  is the thermal noise; and  $N$  is the number of temporal samples per pulse. Observe that to simplify the notations we omit the dependence of  $\mathbf{c}_{ij}(t)$  and  $\mathbf{e}_{ij}(t)$  on  $k$  in (5.13). This is justified because the dependence on  $k$  will not play a role in our statistical analysis of Section 5.3.4, since we will assume that the statistical properties of the clutter return and measurement noise are temporally white. Furthermore, though the mathematical notation of the number of temporal samples is inconsistent with that of the electrical refractivity, the exact meaning can always be understood from the context.

From Fig. 5.3, we can represent  $\boldsymbol{\mu}_{ij}(t, \boldsymbol{\zeta}_k)$  as

$$\boldsymbol{\mu}_{ij}(t, \boldsymbol{\zeta}_k) = \boldsymbol{\mu}_{ij}^{\text{dd}}(t, \boldsymbol{\zeta}_k) + \boldsymbol{\mu}_{ij}^{\text{dr}}(t, \boldsymbol{\zeta}_k) + \boldsymbol{\mu}_{ij}^{\text{rd}}(t, \boldsymbol{\zeta}_k) + \boldsymbol{\mu}_{ij}^{\text{rr}}(t, \boldsymbol{\zeta}_k), \quad (5.14)$$

where

$$\begin{aligned} \boldsymbol{\mu}_{ij}^{\text{dd}}(t, \boldsymbol{\zeta}_k) &= \mathbf{B}(\theta_j^{\text{d}}, \phi) \mathbf{X}_i^{\text{t}} \boldsymbol{\xi}(\tau_{ij}^{\text{dd}}, f_{\text{D}ij}^{\text{dd}}), \\ \boldsymbol{\mu}_{ij}^{\text{dr}}(t, \boldsymbol{\zeta}_k) &= \mathbf{B}(\theta_j^{\text{r}}, \phi) \Gamma_j \mathbf{X}_i^{\text{t}} \boldsymbol{\xi}(\tau_{ij}^{\text{dr}}, f_{\text{D}ij}^{\text{dr}}), \\ \boldsymbol{\mu}_{ij}^{\text{rd}}(t, \boldsymbol{\zeta}_k) &= \mathbf{B}(\theta_j^{\text{d}}, \phi) \mathbf{X}_i^{\text{t}} \Gamma_i \boldsymbol{\xi}(\tau_{ij}^{\text{rd}}, f_{\text{D}ij}^{\text{rd}}), \\ \boldsymbol{\mu}_{ij}^{\text{rr}}(t, \boldsymbol{\zeta}_k) &= \mathbf{B}(\theta_j^{\text{r}}, \phi) \Gamma_j \mathbf{X}_i^{\text{t}} \Gamma_i \boldsymbol{\xi}(\tau_{ij}^{\text{rr}}, f_{\text{D}ij}^{\text{rr}}), \end{aligned}$$

with

$$\boldsymbol{\xi}(\tau, f_{\text{D}}) \triangleq \mathbf{p}(\alpha_i, \beta_i), a_i e^{-j2\pi(f_i + f_{\text{D}})\tau} e^{j2\pi f_{\text{D}} t}, \quad (5.15)$$

and

- $\phi = \arctan(y/x)$ ,  $\theta_j^{\text{d}} = \arctan((z' - h'_j)/\sqrt{x^2 + y^2})$ ,  $\theta_j^{\text{r}} = \arctan((z' + h'_j)/\sqrt{x^2 + y^2})$ .
- $\mathbf{B}(\theta, \phi)$  denotes the array factor for a two-dimensional polarimetric sensor, defined as [80]

$$\mathbf{B}(\theta, \phi) = \begin{bmatrix} -\sin \phi & -\cos \phi \sin \theta \\ 0 & \cos \theta \end{bmatrix}. \quad (5.16)$$

- $\mathbf{X}_i^{\text{t}}$  is the scattering matrix of the target. Here we consider same  $\mathbf{X}_i^{\text{t}}$  for both the direct and reflected paths, assuming that their angular separation is not large for every receiver in a co-located MIMO setup.

- The reflection matrix due to the reflecting surface is given as

$$\mathbf{\Gamma}_j = \begin{bmatrix} \gamma_j^h & 0 \\ 0 & \gamma_j^v \end{bmatrix}, \quad (5.17)$$

where

$$\begin{aligned} \gamma_j^h &\triangleq \frac{\sin \theta_j^r - \sqrt{\epsilon_0 - \cos^2 \theta_j^r}}{\sin \theta_j^r + \sqrt{\epsilon_0 - \cos^2 \theta_j^r}} \approx -1 \quad \text{when } \theta_j^r \approx 0^\circ, \\ \gamma_j^v &\triangleq \frac{\epsilon_0 \sin \theta_j^r - \sqrt{\epsilon_0 - \cos^2 \theta_j^r}}{\epsilon_0 \sin \theta_j^r + \sqrt{\epsilon_0 - \cos^2 \theta_j^r}} \approx -1 \quad \text{when } \theta_j^r \approx 0^\circ, \end{aligned}$$

and  $\epsilon_0$  is the relative permittivity at the reflecting surface.

- The transmitting polarization vector is given as [80]

$$\mathbf{p}(\alpha_i, \beta_i) \triangleq \begin{bmatrix} \cos \alpha_i & \sin \alpha_i \\ -\sin \alpha_i & \cos \alpha_i \end{bmatrix} \begin{bmatrix} \cos \beta_i \\ j \sin \beta_i \end{bmatrix}, \quad (5.18)$$

with  $\alpha_i$  and  $\beta_i$  are the orientation and ellipticity of the  $i$ -th polarization ellipse.

- $\mathbf{a} \triangleq [a_0, a_1, \dots, a_{L-1}]^T$  represents the complex weights transmitted over  $L$  transmitters (and also subcarriers).
- The delays and Doppler frequencies are expressed as

$$\begin{aligned} \tau_{ij}^{\text{dd}} &= \tau(h'_i) + \tau(h'_j), & \tau_{ij}^{\text{dr}} &= \tau(h'_i) + \tau(-h'_j), \\ \tau_{ij}^{\text{rd}} &= \tau(-h'_i) + \tau(h'_j), & \tau_{ij}^{\text{rr}} &= \tau(-h'_i) + \tau(-h'_j), \\ f_{\text{D}ij}^{\text{dd}} &= f_{\text{D}}(h'_i) + f_{\text{D}}(h'_j), & f_{\text{D}ij}^{\text{dr}} &= f_{\text{D}}(h'_i) + f_{\text{D}}(-h'_j), \\ f_{\text{D}ij}^{\text{rd}} &= f_{\text{D}}(-h'_i) + f_{\text{D}}(h'_j), & f_{\text{D}ij}^{\text{rr}} &= f_{\text{D}}(-h'_i) + f_{\text{D}}(-h'_j), \end{aligned}$$



where

$$\begin{aligned}\tau(h) &\triangleq \frac{1}{c} \left[ \sqrt{x^2 + y^2 + (z' - h)^2} \right], \\ f_D(h) &\triangleq \frac{f_i}{c} \left[ \frac{x\dot{x} + y\dot{y} + (z' - h)\dot{z}'}{\sqrt{x^2 + y^2 + (z' - h)^2}} \right],\end{aligned}$$

and  $f_i = f_c + i \Delta f$  denotes the  $i$ -th transmitting frequency.

Stacking the measurements of all  $L \times L$  transmitter-receiver pairs and  $N$  temporal instants into a  $2L^2N \times 1$  column vector we get

$$\mathbf{y}_k = \boldsymbol{\mu}(\boldsymbol{\zeta}_k) + \mathbf{c} + \mathbf{e}, \quad (5.19)$$

where  $\mathbf{y}(t_n, \boldsymbol{\zeta}_k) = [\mathbf{y}_{00}(t_n, \boldsymbol{\zeta}_k)^T, \dots, \mathbf{y}_{0L-1}(t_n, \boldsymbol{\zeta}_k)^T, \dots, \mathbf{y}_{L-1L-1}(t_n, \boldsymbol{\zeta}_k)^T]^T$  and  $\mathbf{y}_k = [\mathbf{y}(t_0, \boldsymbol{\zeta}_k)^T, \mathbf{y}(t_1, \boldsymbol{\zeta}_k)^T, \dots, \mathbf{y}(t_{N-1}, \boldsymbol{\zeta}_k)^T]^T$ ; similarly for  $\boldsymbol{\mu}$ ,  $\mathbf{c}$ , and  $\mathbf{e}$ .

### 5.3.3 Clutter Model

We model the clutter component, which also depends on the transmitted signal [113], as follows:

$$\mathbf{c}_{ij}(t) = \mathbf{B}(\theta_j^c, \phi) \mathbf{X}_i^c(t) \boldsymbol{\xi}(\tau_{ij}^c, 0), \quad (5.20)$$

where  $\theta^c$  indicates the direction of the radar beam;  $\mathbf{X}_i^c(t)$  is the scattering matrix of the clutter;  $\tau_{ij}^c$  is the corresponding average clutter delay;  $\boldsymbol{\xi}(\cdot)$  is defined in (5.15). Here we assume that the clutter does not introduce any Doppler shift. Following [174],

we define

$$\mathbf{x}_i^c(t) \triangleq \left[ x_i^{\text{hh,c}}, x_i^{\text{vv,c}}, x_i^{\text{hv,c}}, x_i^{\text{vh,c}} \right]^T, \quad (5.21)$$

$$\tilde{\mathbf{P}}_{ij}^c \triangleq \begin{bmatrix} \tilde{p}_1^c & 0 & \tilde{p}_2^c & 0 \\ 0 & \tilde{p}_2^c & 0 & \tilde{p}_1^c \end{bmatrix}, \quad (5.22)$$

$$[\tilde{p}_1^c, \tilde{p}_2^c]^T \triangleq \boldsymbol{\xi}(\tau_{ij}^c, 0) = \mathbf{p}(\alpha_i, \beta_i) a_i e^{-j2\pi f_i \tau_{ij}^c}. \quad (5.23)$$

Hence, we can rearrange (5.20) to express the clutter scattering coefficients in a vector form as

$$\mathbf{c}_{ij}(t) = \mathbf{B}(\theta_j^c, \phi) \tilde{\mathbf{P}}_{ij}^c \mathbf{x}_i^c(t). \quad (5.24)$$

### 5.3.4 Statistical Assumptions

In LGA scenarios, it is known that the clutter from the sea surface produces spikes or higher amplitude returns, and therefore the probability density function of the complex envelope of the sea-clutter returns exhibits heavy tails, which is significantly deviated from a standard Gaussian model [112], [175], [176]. Hence from the physical mechanism, a two-scale sea-surface scattering model, termed compound-Gaussian model, is developed [77], [78]. According to this model, the complex envelope of the sea-clutter returns can be written as a product of two components

$$\mathbf{x}_i^c(t) = \sqrt{u(t)} \boldsymbol{\chi}(t), \quad (5.25)$$

where  $u(t)$ , referred to as *texture*, is a slow-changing component that describes the underlying mean power level, and  $\boldsymbol{\chi}(t)$ , referred to as *speckle*, is a fast-changing

component that accounts for local backscattering. Various distributions are used to appropriately characterize the texture component [112]. We model the texture component as an inverse gamma random variable, since this distribution fits well with the real sea-clutter data [177]. The speckle component is assumed to be a stationary complex Gaussian process with zero mean and covariance  $\Sigma^c$ , which is parameterized as [174]

$$\Sigma^c = \begin{bmatrix} \sigma_p^2 \mathbf{p}(\alpha^c, \beta^c) \mathbf{p}(\alpha^c, \beta^c)^H + \sigma_u^2 \mathbf{I}_2 & \mathbf{0} \\ \mathbf{0} & p_x \mathbf{I}_2 \end{bmatrix}, \quad (5.26)$$

where  $\sigma_p^2$  and  $\sigma_u^2$  are the power of the polarized and unpolarized components of the clutter, respectively;  $\alpha^c$  and  $\beta^c$  are the orientation and ellipticity of the clutter polarization ellipse, respectively; the polarization vector  $\mathbf{p}(\cdot)$  is defined in (5.18); and  $p_x$  is the power of the cross-polarized clutter components.

We assume that the thermal noise component,  $\mathbf{e}_{ij}$ , is a complex Gaussian vector with zero mean and covariance  $\sigma_e^2 \mathbf{I}_2$ , and it is uncorrelated with the clutter return. We further assume that the clutter and noise responses are uncorrelated among different frequency channels, and are spatially and temporally white. Under these assumptions, we can write the conditional distribution of the measurement vector as

$$\mathbf{y}_k | u, \boldsymbol{\mu}(\boldsymbol{\zeta}_k) \sim \mathbb{CN}_{2L^2N}(\boldsymbol{\mu}(\boldsymbol{\zeta}_k), \boldsymbol{\Sigma}), \quad (5.27)$$

where

$$\begin{aligned} \boldsymbol{\Sigma} &= \mathbf{I}_N \otimes (\mathbf{Q} (\mathbf{I}_{L^2} \otimes u \boldsymbol{\Sigma}_c) \mathbf{Q}^H + \sigma_e^2 \mathbf{I}_{2L^2}), \\ \mathbf{Q} &\triangleq \text{blkdiag} \left( \mathbf{B}(\theta_0^c, \phi) \tilde{\mathbf{P}}_{00}^c, \dots, \mathbf{B}(\theta_{L-1}^c, \phi) \tilde{\mathbf{P}}_{L-1L-1}^c \right). \end{aligned}$$

## 5.4 Tracking Filter

We employ a sequential Monte Carlo method [82] – [84], which is known to be powerful for solving nonlinear and non-Gaussian Bayesian inference problems. In this approach the key idea is to represent the posterior density function by a set of random sample points with associated weights and to compute the required estimates based on these samples and weights.

Let  $\zeta_k^{(i)}, i = 1, 2, \dots, N_\zeta$ , denote the sample points with associated weights  $w_k^{(i)}, i = 1, 2, \dots, N_\zeta$ , that characterize the posterior density function at the  $k$ -th time instant. Mathematically

$$p(\zeta_k | \mathbf{y}_k) \approx \sum_{i=1}^{N_\zeta} w_k^{(i)} \delta(\zeta_k - \zeta_k^{(i)}). \quad (5.28)$$

However, in practice the samples  $\zeta_k^{(i)}, i = 1, 2, \dots, N_\zeta$ , are generated from a proposal (or importance) density function  $q(\zeta_k^{(i)} | \zeta_{k-1}^{(i)}, \mathbf{y}_k)$ , which is easier to sample from. Then, the corresponding weights are updated as [82]

$$w_k^{(i)} \propto w_{k-1}^{(i)} \frac{p(\mathbf{y}_k | \zeta_k^{(i)}) p(\zeta_k^{(i)} | \zeta_{k-1}^{(i)})}{q(\zeta_k^{(i)} | \zeta_{k-1}^{(i)}, \mathbf{y}_k)}. \quad (5.29)$$

In this work, we use the transitional prior,  $p(\zeta_k^{(i)} | \zeta_{k-1}^{(i)})$ ,  $i = 1, 2, \dots, N_\zeta$ , as the importance density function. Since we include the target position, velocity, and scattering coefficients into the state vector, the dimension of our state space is very large. So we apply the Gibbs sampling technique [178] to draw samples from  $p(\zeta_k^{(i)} | \zeta_{k-1}^{(i)})$ . We partition our state vector into seven parts as  $\zeta = [\tilde{\zeta}^T, \boldsymbol{\vartheta}^T, \boldsymbol{\varepsilon}^T, \mathbf{m}^T, \boldsymbol{\rho}^T, \boldsymbol{\varsigma}^T, \boldsymbol{\varpi}^T]^T$ ,

where  $\tilde{\zeta}$  includes only the target position and velocity. This partitioning is done following the statistical independence of each part with others. Then, we draw the corresponding seven sets of particles as  $\tilde{\zeta}_k^{(i)} \sim p(\tilde{\zeta}_k | \tilde{\zeta}_{k-1}^{(i)})$ ,  $\boldsymbol{\vartheta}_k^{(i)} \sim p(\boldsymbol{\vartheta}_k | \boldsymbol{\vartheta}_{k-1}^{(i)})$ , and so on to obtain  $\zeta_k^{(i)} = [(\tilde{\zeta}_k^{(i)})^T, (\boldsymbol{\vartheta}_k^{(i)})^T, (\boldsymbol{\varepsilon}_k^{(i)})^T, (\boldsymbol{m}_k^{(i)})^T, (\boldsymbol{\rho}_k^{(i)})^T, (\boldsymbol{\varsigma}_k^{(i)})^T, (\boldsymbol{\varpi}_k^{(i)})^T]^T$ . The importance weights are realized as  $w_k^{(i)} \propto w_{k-1}^{(i)} p(\mathbf{y}_k | \zeta_k^{(i)})$ . However, since our likelihood function does not have a closed-form expression, we use the generalized Gauss-Laguerre quadrature formula [179, Ch. 5.3] to numerically evaluate

$$p(\mathbf{y}_k | \zeta_k^{(i)}) = \int_{\mathcal{U}} p(\mathbf{y}_k | u, \zeta_k^{(i)}) p(u) du \approx \sum_{g=1}^G \tilde{w}_g p(\mathbf{y}_k | u_g, \zeta_k^{(i)}), \quad (5.30)$$

where  $G$  is the quadrature order, and  $u_g$  and  $\tilde{w}_g$  are the abscissas and weights of the generalized Gauss-Laguerre quadrature. The key steps of this tracking algorithm is explained using a flowchart in Fig. 5.4.

## 5.5 Adaptive Waveform Design

In this section, we propose an information theoretic waveform design technique for improved tracking performance. Previous work in the application of information theoretic criteria for radar waveform design includes [180] – [184] and the references therein. Our approach is to mathematically formulate a utility function based on mutual information of the target state and measurement vectors, and then to determine the parameters of the next pulse by maximizing this utility function.

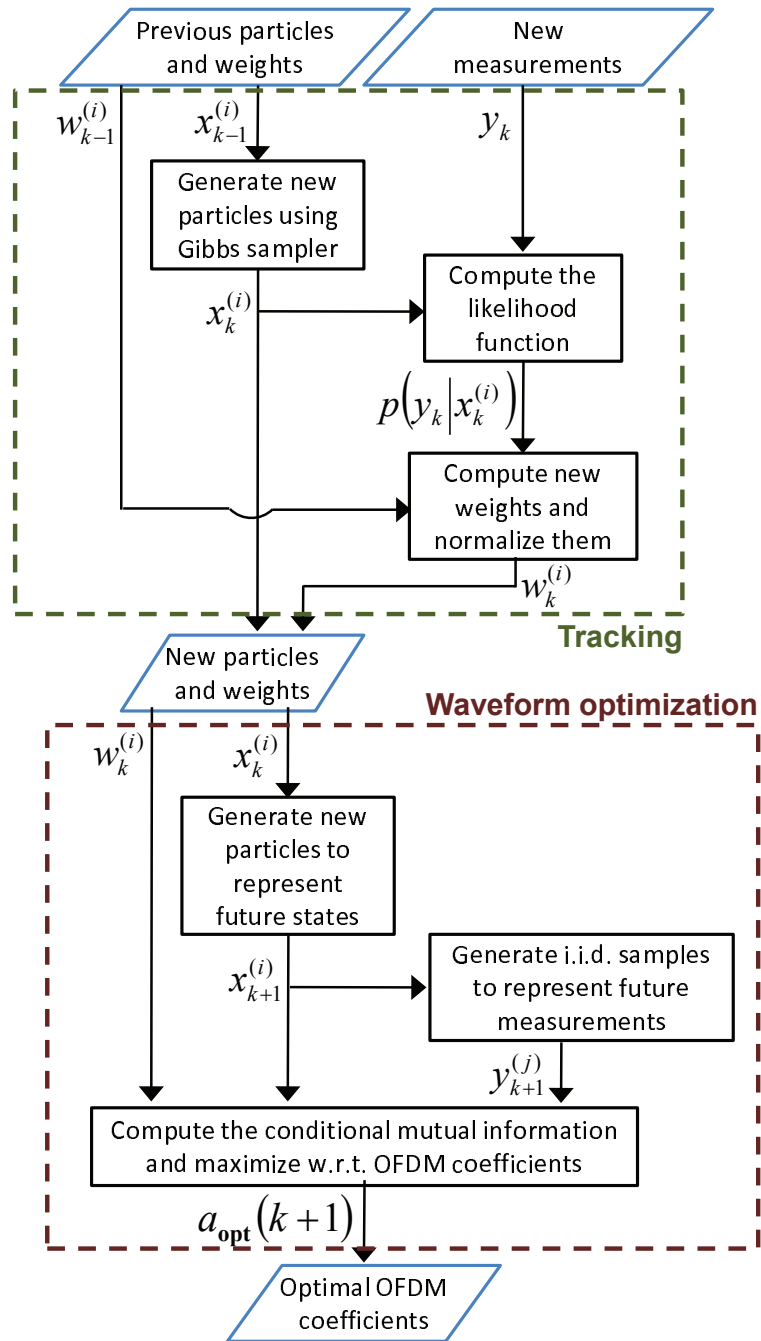


Figure 5.4: Flowchart of the key steps involved in the tracking and waveform design procedure.

### 5.5.1 Mutual Information

In probability theory and information theory, the mutual information of two random variables is a quantity that measures the mutual dependence of the two variables. Mathematically, the mutual information of two random variables  $X$  and  $Y$  is defined as [85]

$$I(X; Y) = E_{X,Y} \left[ \log \frac{p(X, Y)}{p(X)p(Y)} \right], \quad (5.31)$$

where  $p(X, Y)$  is the joint probability distribution function and  $p(X)$ ,  $p(Y)$  are the marginal probability distribution functions of  $X$  and  $Y$ , respectively. Intuitively, mutual information measures the information that  $X$  and  $Y$  share. For example, if  $X$  and  $Y$  are independent, then their mutual information is zero, so knowing  $X$  does not give any information about  $Y$  and vice versa. At the other extreme, if  $X$  and  $Y$  are identical, then all information conveyed by  $X$  is shared with  $Y$ , i.e., knowing  $X$  determines the value of  $Y$  and vice versa. We can get more insight about mutual information from the following relationship

$$I(X; Y) = H(X) - H(X|Y), \quad (5.32)$$

where  $H(X)$  is the marginal entropy of  $X$  and  $H(X|Y)$  is the conditional entropy of  $X$  given  $Y$ .  $H(X)$  quantifies the amount of uncertainty in  $X$ , and  $H(X|Y)$  gives the measure of the uncertainty remaining in  $X$  after  $Y$  is known. Thus, the difference of these two quantities corroborates the intuitive meaning of mutual information as the reduction of uncertainty (i.e., amount of information) in  $X$  after knowing  $Y$ . Furthermore, from the notion of Bayesian inference, the mutual information can also be expressed as the expectation (over the measurements  $Y$ ) of the Kullback-Leibler

(KL) divergence [185] between the posterior and prior distributions, i.e.,

$$I(X; Y) = \mathbb{E}_Y [D_{\text{KL}}(p(X|Y) || p(X))]. \quad (5.33)$$

The more different the posterior and prior distributions, the greater is the information gain due to the measurements.

### 5.5.2 Waveform Design

We develop a criterion that selects the optimal waveform at the  $k$ -th pulse duration such that the mutual information between the state and measurement vectors at the  $(k + 1)$ -th pulse duration is maximized. However, because of their availability we must also exploit the measurement history  $\mathbf{y}_{1:k} = \{\mathbf{y}_1, \mathbf{y}_2, \dots, \mathbf{y}_k\}$  to improve our optimization procedure. Hence, we formulate a utility function in terms of conditional mutual information as follows:

$$\tilde{I}(\boldsymbol{\zeta}_{k+1}; \mathbf{y}_{k+1} | \mathbf{y}_{1:k}) = \mathbb{E}_{\boldsymbol{\zeta}_{k+1}, \mathbf{y}_{k+1} | \mathbf{y}_{1:k}} \left[ \log \frac{p(\mathbf{y}_{k+1} | \boldsymbol{\zeta}_{k+1}, \mathbf{y}_{1:k})}{p(\mathbf{y}_{k+1} | \mathbf{y}_{1:k})} \right]. \quad (5.34)$$

Defining

$$\begin{aligned} \Lambda(\boldsymbol{\zeta}_{k+1}, \mathbf{y}_{k+1}) &\triangleq \log \frac{p(\mathbf{y}_{k+1} | \boldsymbol{\zeta}_{k+1}, \mathbf{y}_{1:k})}{p(\mathbf{y}_{k+1} | \mathbf{y}_{1:k})}, \\ &= \log \frac{p(\mathbf{y}_{k+1} | \boldsymbol{\zeta}_{k+1})}{\int_{\boldsymbol{\zeta}} p(\mathbf{y}_{k+1} | \boldsymbol{\zeta}_{k+1}) p(\boldsymbol{\zeta}_{k+1} | \mathbf{y}_{1:k}) d\boldsymbol{\zeta}_{k+1}}, \end{aligned} \quad (5.35)$$

we can explicitly write (5.34) as

$$\tilde{I}(\boldsymbol{\zeta}_{k+1}; \mathbf{y}_{k+1} | \mathbf{y}_{1:k}) = \int_{\boldsymbol{\zeta}} \left[ \int_{\mathbf{y}} \Lambda(\boldsymbol{\zeta}_{k+1}, \mathbf{y}_{k+1}) p(\mathbf{y}_{k+1} | \boldsymbol{\zeta}_{k+1}) d\mathbf{y}_{k+1} \right] p(\boldsymbol{\zeta}_{k+1} | \mathbf{y}_{1:k}) d\boldsymbol{\zeta}_{k+1}. \quad (5.36)$$



We use Monte Carlo integration to compute this integral. To calculate the outer integral we need samples of the state  $\zeta_{k+1}$ . From the posterior density function at the  $k$ -th time step,  $p(\zeta_k|\mathbf{y}_{1:k})$ , we obtain  $N_\zeta$  samples  $\zeta_k^{(i)}$  and associated weights  $w_k^{(i)}$ . Then, the corresponding samples and weights at the  $(k+1)$ -th time instant are given as  $\zeta_{k+1}^{(i)}$  and  $w_k^{(i)}$ , where  $\zeta_{k+1}^{(i)} \sim p(\zeta_{k+1}|\zeta_k^{(i)})$  [113]. To calculate the inner integral, we need samples of the measurement  $\mathbf{y}_{k+1}$ . We draw  $N_y$  independent and identically distributed samples for each  $\zeta_{k+1}^{(i)}$  from the likelihood function  $p(\mathbf{y}_{k+1}|\zeta_{k+1}^{(i)})$ . Then we approximate (5.36) as

$$\tilde{I}(\zeta_{k+1}; \mathbf{y}_{k+1}|\mathbf{y}_{1:k}) \approx \frac{1}{N_y} \sum_{i=1}^{N_\zeta} \sum_{j=1}^{N_y} w_k^i \Lambda(\zeta_{k+1}^{(i)}, \mathbf{y}_{k+1}^{(j)}), \quad (5.37)$$

where

$$\Lambda(\zeta_{k+1}^{(i)}, \mathbf{y}_{k+1}^{(j)}) = \log \frac{p(\mathbf{y}_{k+1}^{(j)}|\zeta_{k+1}^{(i)})}{\sum_{l=1}^{N_\zeta} w_k^{(l)} p(\mathbf{y}_{k+1}^{(j)}|\zeta_{k+1}^{(l)})},$$

and obtain the optimal waveform to be transmitted at the  $(k+1)$ -th time instant as

$$\mathbf{a}_{\text{opt}}(k+1) = \arg \max_{\mathbf{a} \in \mathbb{C}^L} \tilde{I}(\zeta_{k+1}; \mathbf{y}_{k+1}|\mathbf{y}_{1:k}), \quad \text{subject to } \mathbf{a}^H \mathbf{a} = 1, \quad (5.38)$$

where the constraint  $\mathbf{a}^H \mathbf{a} = 1$  ensures constant energy transmission. The lower block of the flowchart in Fig. 5.4 describes the key steps involved in this waveform design algorithm.

## 5.6 Numerical Results

We present the results of several numerical examples to demonstrate the performance of our tracker due to the incorporation of the realistic physical effects, frequency diversity of the OFDM signalling through MIMO configuration, and proposed adaptive waveform design technique. First, we provide a description of the simulation setup and then discuss different numerical examples.

- Target and clutter parameters:
  - The target started at a position  $(x, y, z) = (17.32 \text{ km}, 10 \text{ km}, 20 \text{ m})$  and was moving with velocity of  $1000 (= 1000 \cos(\pi/9)\hat{i} + 1000 \sin(\pi/9)\hat{j})$  m/s.
  - The scattering parameters of the target were considered to be partially known ( $\vartheta_l = 45^\circ$ ,  $\varepsilon_l = 36^\circ$ ,  $\varrho_l = 0^\circ$ ,  $\nu_l = 0^\circ$ ,  $\varpi_l = 0^\circ$ , for  $l = 0, \dots, L-1$ ) except for  $\mathbf{m}$ . Hence, the unknown state parameters that we tracked were  $[x, y, z, \dot{x}, \dot{y}, \dot{z}, m_0, m_1, \dots, m_{L-1}]^T$ .
  - In the target state model, we used  $q_{\text{pv}} = 4.5 \times 10^{-3}$  and  $q_{\text{scat}} = 4 \times 10^{-5}$ .
  - The parameters of the clutter covariance matrix were assumed to be already estimated ( $\alpha^c = 85^\circ$ ,  $\beta^c = 5^\circ$ ,  $\sigma_p^2 = 0.6$ ,  $\sigma_u^2 = 0.3$ ,  $p_x = 0.1$ , and the shape parameter of the inverse-gamma texture distribution = 4) and then scaled to satisfy the required TCR and CNR, defined as

$$\text{TCR} \triangleq \frac{(1/N) \boldsymbol{\mu}^H \boldsymbol{\mu}}{\text{tr} \{ \mathbf{Q} (\mathbf{I}_{L^2} \otimes u \boldsymbol{\Sigma}_c) \mathbf{Q}^H \}}, \quad (5.39)$$

$$\text{CNR} \triangleq \frac{\text{tr} \{ \mathbf{Q} (\mathbf{I}_{L^2} \otimes u \boldsymbol{\Sigma}_c) \mathbf{Q}^H \}}{2L^2 \sigma_e^2}. \quad (5.40)$$

In our simulations, we used TCR = 5 dB and CNR = 10 dB.

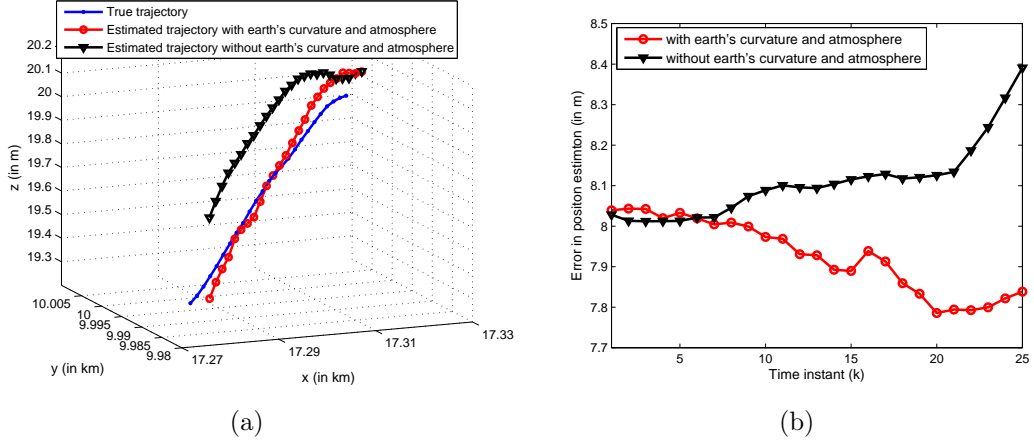


Figure 5.5: Comparison of the (a) true and estimated trajectories and (b) associated errors in position estimation due to the earth's curvature and standard lower atmosphere modeling.

- Radar parameters:
  - Carrier frequency  $f_c = 1$  GHz.
  - Total bandwidth  $B = 100$  MHz.
  - Number of OFDM subcarriers  $L = 3$ .
  - Subcarrier spacing  $\Delta f = B/(L + 1) = 25$  MHz.
  - All the transmit weights were equal, i.e.,  $a_l = 1/\sqrt{L} \forall l$ .
  - Pulse width  $T = 1/\Delta f = 40$  ns.
  - Pulse repetition interval  $T_p = 2$  ms.
  - Number of temporal samples per pulse  $N = 5$ .
  - Number of transceivers  $L = 3$  (forming a  $3 \times 3$  co-located MIMO configuration).
  - Positions of the transceivers were  $(0, 0, 40)$ ,  $(0, 0, 40.15)$ , and  $(0, 0, 40.3)$  m, maintaining an inter-sensor spacing of  $\lambda_c/2$ .
  - Transmission polarization ellipses had  $\alpha_l = 0$ ,  $\beta_l = 45^\circ \forall l$ .

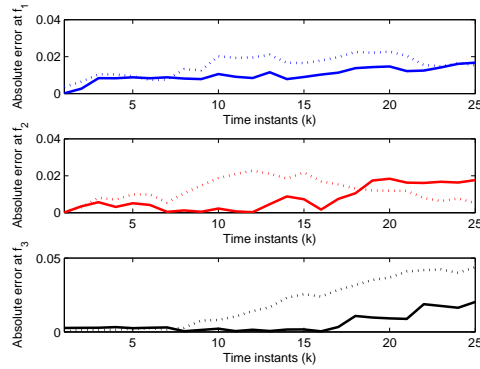


Figure 5.6: Absolute error in scattering coefficients at three different frequencies with (solid lines) and without (dotted lines) considering earth’s curvature and standard lower atmosphere modeling.

## Importance of Realistic Modeling

Fig. 5.5 depicts the tracking performance and associated errors in position estimation with and without considering the effects of the earth’s curvature and standard lower atmosphere (having  $dN/dh = -39$   $N$ -units/km) modeling. The plot with the trajectories are typical, i.e., based on a single realization of the noise processes; whereas the results on the position error estimation were averaged over 50 independent realizations (with the same initial condition mentioned under the target parameters but different realizations of the noise processes), and hence imply RMSE. In this simulation, we did not consider the presence of any evaporation duct. In Fig. 5.6, we plot the resultant absolute error associated with the target scattering coefficients ( $\mathbf{m}$ ) at three different frequencies. It is evident from these plots that we achieved better tracking accuracy, both for the target trajectory and scattering coefficients, by incorporating the underlying physical effects.

We also studied the effects of an evaporation duct on the tracking performance and the results are shown in Figs. 5.7 and 5.8. We changed the carrier frequency to 10 GHz,

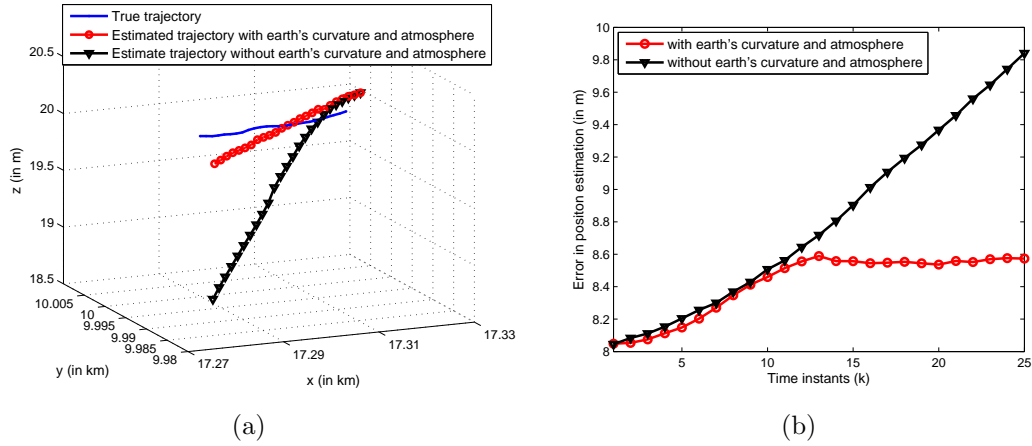


Figure 5.7: Comparison of the (a) true and estimated trajectories and (b) associated errors in position estimation due to the earth's curvature and evaporating duct modeling.

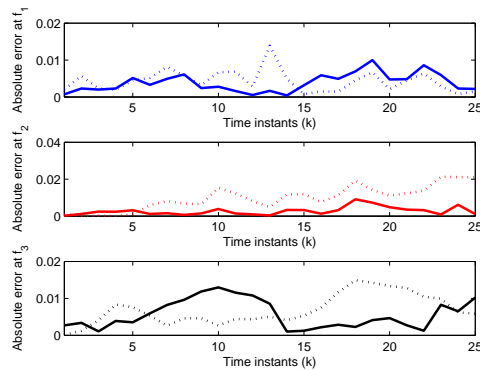


Figure 5.8: Absolute error in scattering coefficients at three different frequencies with (solid lines) and without (dotted lines) considering earth's curvature and evaporation duct modeling.

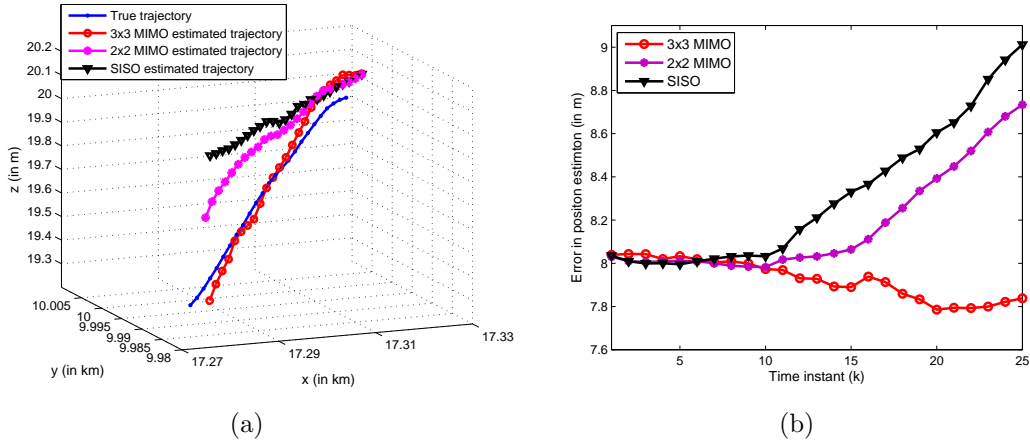


Figure 5.9: Comparison of the (a) true and estimated trajectories and (b) associated errors in position estimation due to the OFDM MIMO configurations.

and considered a trapping layer with  $dN/dh = -393$   $N$ -units/km [155, Table 2.1] and with height enough to cover both the radar and target within it. Comparing Figs. 5.5 and 5.7 we noticed that the tracker, which ignored the effects of the earth’s curvature and atmosphere, committed larger errors in estimating the target trajectory under the presence of an evaporation duct compared to that in a standard atmosphere.

## Effect of OFDM MIMO Configuration

In Fig. 5.9, we plot the estimated target trajectories along with the true trajectory and associated position errors for two MIMO and one single-input-single-output (SISO) configurations. We varied the power per transmitter accordingly to ensure that all of these three configurations transmitted the same amount of power per pulse. We simulated this under a standard atmospheric condition with  $dN/dh = -39$   $N$ -units/km and zero evaporation duct height. The results clearly demonstrated the improvement gained due to the frequency diversity of the OFDM signalling through the MIMO configuration.

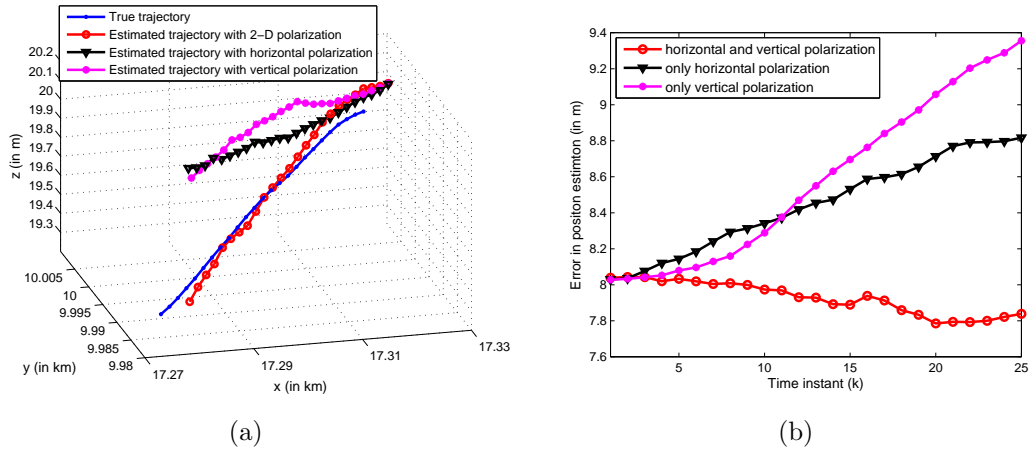


Figure 5.10: Comparison of the (a) true and estimated trajectories and (b) associated errors in position estimation due to the polarization-sensitive transceivers.

## Effect of Polarization

To understand the importance of polarimetric measurements, in Fig. 5.10(a) we show a comparative plot of the estimated target trajectories along with the true trajectory while considering only horizontal, then only vertical, and then jointly horizontal and vertical polarizations. Fig. 5.10(b) depicts the associated position errors for these three scenarios. While simulating with only horizontal or only vertical polarization, we increased the power per transmitter by two so that all three setups employed the same amount of power per pulse. We considered a standard atmospheric condition with  $dN/dh = -39$  N-units/km and zero evaporation duct height. The results clearly demonstrated the improvement gained due to the polarization diversity.

## Effect of Adaptive Waveform Design

Figs. 5.11 and 5.12 demonstrate the improvement in tracking performance due to the adaptive waveform design in comparison with a fixed waveform. The adaptive

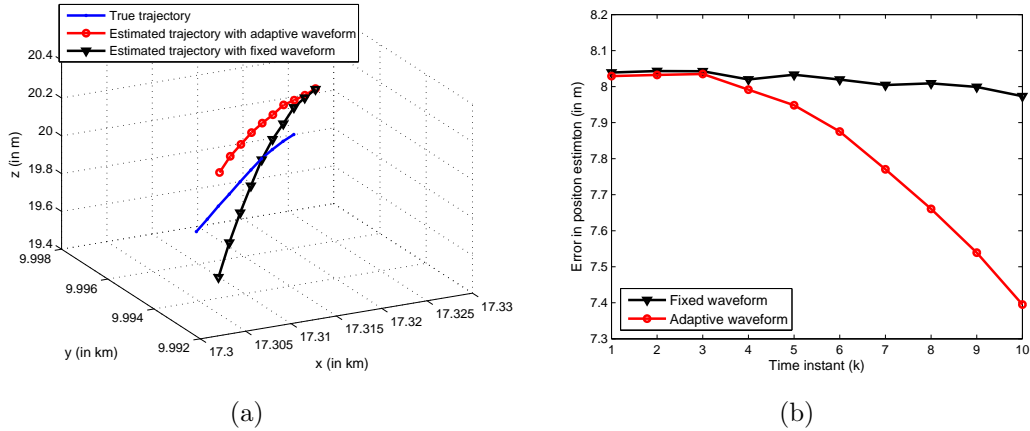


Figure 5.11: Comparison of the (a) true and estimated trajectories and (b) associated errors in position estimation due to the fixed and adaptive waveforms.

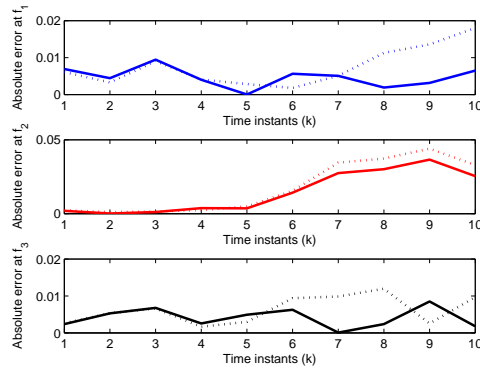


Figure 5.12: Absolute error in scattering coefficients at three different frequencies with fixed (dotted lines) and adaptive (solid lines) waveforms.

radar transmitted  $a_l = \{0.3568, 0.4982, 0.7902\}$ , which were computed using (5.38), whereas the fixed radar used  $a_l = 1/\sqrt{L} = 0.5774 \forall l$ . The constraint  $\mathbf{a}^H \mathbf{a} = 1$  in (5.38) ensured that both the adaptive and fixed radars transmitted the same amount of power per pulse. For this simulation too we considered a standard atmospheric condition with  $dN/dh = -39$  N-units/km and zero evaporation duct height.



## 5.7 Summary

We developed an OFDM MIMO adaptive waveform design algorithm for low-grazing angle target tracking based on mutual information criterion. We incorporated into the model complex physical behaviors and statistical characteristics as realistically as possible, yet kept the model amenable to signal processing. We developed the parametric measurement model of an OFDM MIMO radar system employing polarization-sensitive transceivers. Based on the state and measurement models, we employed a particle filter in a closed-loop fashion by integrating the adaptive waveform design procedure with it. We selected the optimal OFDM waveform by maximizing the mutual information between the state and measurement vectors for one time-step ahead. In the next chapter, we extend our work on tracking for multiple targets. However, for simplicity, we do not consider any effects of multipath reflections.

# Chapter 6

## Multi-Target Tracking Using Delay-Doppler Sparsity<sup>5</sup>

In this chapter, we propose a sparsity-based approach to track multiple targets in a region of interest using an OFDM radar. We observe that in a particular pulse interval the targets lie at a few points on the delay-Doppler plane, and hence we exploit that inherent sparsity to develop a tracking procedure. The use of an OFDM signal not only increases the frequency diversity of our system, but also decreases the block-coherence measure [90] of the equivalent sparse model. To maximize the accuracy in the sparse-recovery we design the OFDM signal for the minimum block-coherence measure. In the tracking filter, we used the same block-sparsity property to propose a block version of the CoSaMP algorithm [91].

### 6.1 Introduction

For a number of years, the problem of simultaneous tracking of multiple targets has been one of the most relevant and challenging issues in a wide variety of military

---

<sup>5</sup>Based on S. Sen and A. Nehorai, “Sparsity-based multi-target tracking using OFDM radar,” *IEEE Trans. Signal Process.*, to appear. ©[2010] IEEE.

and civilian systems [186], [187]. Multi-target tracking is of primary interest in many applications, such as radar tracking of airborne or ground moving vehicles, sonar tracking of submarines, tracking of people for security purposes, and mobile robotics. The situation becomes even more complicated when the tracks of two targets cross.

A large number of algorithms have been proposed in the literature to tackle the multi-target tracking problem. The probabilistic data association (PDA) [188] and joint probabilistic data association (JPDA) [189] algorithms employ a multi-hypothesis approach per time step, in which several hypotheses are considered per target. However, at each time step, all the hypotheses per target are merged into one to provide a single-hypothesis approach between time instances. On the other hand, the multiple hypotheses tracking (MHT) [190] algorithm keeps track of all the possible data association hypotheses over time. However, this is an NP-hard problem, as the number of association hypotheses grows over time [191]. To avoid an explicit data association step, track before detect (TBD) [192], [193] algorithms have been developed using particle filter theory [84], [194]. However, these may lead to large computational complexity. With an increase in the number of targets, the dimensionality of the joint state-space increases exponentially.

In this work, we look into the multi-target tracking problem from a different perspective. We observe that a multi-target scene is generated by keeping track of the range and velocity (delay and Doppler, respectively) of each target over time. Suppose we discretize the delay-Doppler plane into  $N_\tau \times N_\beta$  grid points. Then, if number of targets  $M \ll N_\tau N_\beta$ , the target scene will be *sparse* in the delay-Doppler plane. This enables us to efficiently track the targets by applying a sparse-recovery algorithm [91], [132] – [134].

First, we present a state model describing the dynamic behavior of the targets. Then, we develop a parametric measurement model considering an OFDM radar. The use of an OFDM radar increases the frequency diversity of the system and decreases the block-coherence measure of the system matrix of the equivalent sparse measurement model.

Next, by exploiting the sparsity in the delay-Doppler plane, we convert the OFDM measurement model to an equivalent sparse measurement model, in which the nonzero components of the sparse vector correspond to the scattering coefficients of the targets. However, due to the use of a multi-carrier OFDM signal, each target produces multiple scattering coefficients, not a single value. Hence, our sparse vector exhibits an additional structure in the form of the nonzero coefficients occurring in clusters. Such vectors are referred to as block-sparse [88], [89]. We also study the properties of the associated block-sparse measurement matrix by deducing the expressions of its sub-coherence and block-coherence measures [90]. From the expression of the block-coherence, we prove that the minimum value of block-coherence is attainable when equal amounts of energy are transmitted over the available OFDM subcarriers and further prove that the minimum value is inversely proportional to the number of OFDM subcarriers. Hence, this reconfirms the advantage of using the OFDM signals.

As pointed out in [88], the conventional CoSaMP algorithm provides two benefits. It ensures speedy and robust recovery and provides tight error bounds by including the ideas from the combinatorial algorithms [91]. Further, it has a simple, iterative greedy structure that can be modified easily to incorporate the block-sparsity nature of the sparse vector, instead of treating it as a conventional sparse vector and thereby ignoring the additional structure in the problem. Therefore, in the tracking filter, we propose to employ a block version of the CoSaMP algorithm, termed BCoSaMP.

At each pulse interval, we dynamically partition a smaller portion of the delay-Doppler plane, depending on the predicted state parameters. We compare the performance of our sparsity-based tracking method with that of a particle filter (PF) based tracking procedure. Our results show that the sparsity-based tracking algorithm not only takes much less time (about one order less) than the PF-based tracking procedure, but also achieves equal (and sometimes better) tracking performance. In addition, we find similar results when we apply compressive sensing (CS) to our sparse model, by pre-multiplying the measurements with a Gaussian random matrix.

## 6.2 Problem Description and Modeling

Fig. 6.1 presents a schematic representation of the problem scenario. We consider an OFDM radar system that overlooks a region of interest containing multiple moving targets. We assume that the targets are at far-field with respect to the radar, i.e., the relative distance between any two targets is much smaller than their individual distances with respect to the radar. Hence, at a particular pulse interval all the targets can be associated with the same DOA unit vectors  $\mathbf{u}$ .

### 6.2.1 Dynamic State Model

Suppose there are  $M$  targets in the region of interest. Each target's dynamics are described with individual states composed of its position and velocity. At the  $k$ -th pulse interval, we denote the position coordinates of the  $m$ -th target as  $\mathbf{p}_k^m = [x_k^m, y_k^m, z_k^m]^T$  and its velocity components as  $\mathbf{v}_k^m = [\dot{x}_k^m, \dot{y}_k^m, \dot{z}_k^m]^T$ . Then, the state vector of the  $m$ -th target at the  $k$ -th pulse interval is  $\boldsymbol{\zeta}_k^m \triangleq [(\mathbf{p}_k^m)^T, (\mathbf{v}_k^m)^T]^T$ .

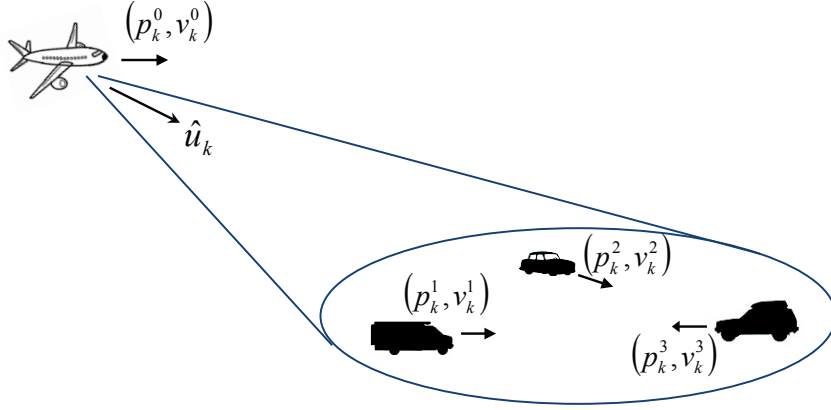


Figure 6.1: A schematic representation of a multi-target tracking scenario (not drawn to scale).

Assuming constant velocity movement, we obtain a linear dynamic state equation of the  $m$ -th target at the  $k$ -th pulse interval as

$$\zeta_k^m = \begin{bmatrix} \mathbf{I}_3 & T_p \mathbf{I}_3 \\ \mathbf{0} & \mathbf{I}_3 \end{bmatrix} \zeta_{k-1}^m + \mathbf{w}_k^m, \quad \text{for } m = 1, 2, \dots, M, \quad k = 1, 2, \dots, \quad (6.1)$$

where  $T_p$  denotes the sampling interval, which in our case is equal to the PRI. However, in practice the targets could exhibit accelerations or decelerations, which are represented as the state noise vector  $\mathbf{w}$ .

However, instead of the position and velocity, the radar tracks the targets using their associated delays ( $\tau$ ) and Doppler factors ( $\beta$ ). If we consider the radar to be at position  $\mathbf{p}_k^0 = [x_k^0, y_k^0, z_k^0]^T$  and moving with velocity  $\mathbf{v}_k^0 \triangleq \dot{x}_k^0 \hat{i} + \dot{y}_k^0 \hat{j} + \dot{z}_k^0 \hat{k}$ , then we can write the delay and Doppler expressions as

$$\tau_k^m = \frac{2}{c} \|\mathbf{p}_k^m - \mathbf{p}_k^0\|_2, \quad (6.2)$$

$$\beta_k^m = \frac{2}{c} \langle \mathbf{u}_k, \mathbf{v}_k^m \rangle - \frac{2}{c} \langle \mathbf{u}_k, \mathbf{v}_k^0 \rangle, \quad (6.3)$$

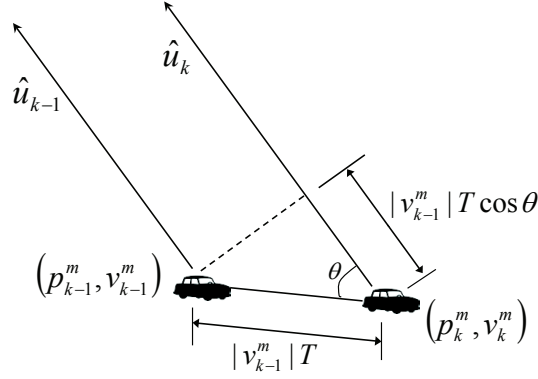


Figure 6.2: Description of a particular target dynamics for two consecutive pulse intervals.

where  $c$  is the speed of propagation;  $\mathbf{u}_k$  is the DOA unit vector, defined as  $\mathbf{u}_k \triangleq u_{xk} \hat{i} + u_{yk} \hat{j} + u_{zk} \hat{k}$  and  $\|\mathbf{u}_k\|_2 = 1$ ; and  $\mathbf{v}_k^m$  is the target velocity represented in vector form as  $\mathbf{v}_k^m \triangleq \dot{x}_k^m \hat{i} + \dot{y}_k^m \hat{j} + \dot{z}_k^m \hat{k}$ . Therefore, we can form a modified state dynamic equation, similar to (6.1), by considering a modified state vector of the  $m$ -th target at the  $k$ -th pulse interval, i.e.,  $\bar{\boldsymbol{\zeta}}_k^m \triangleq [\tau_k^m, \beta_k^m]^T$ .

Note that under the far-field assumption, as shown in Fig. 6.2, we can approximate that  $\mathbf{u}_k \approx \mathbf{u}_{k-1}$ , and due to the constant velocity movement we have  $\mathbf{v}_k^m \approx \mathbf{v}_{k-1}^m$ . Therefore, in terms of the Doppler factor we get

$$\beta_k^m \approx \beta_{k-1}^m. \quad (6.4)$$

Moreover, from Fig. 6.2 we can write

$$\|\mathbf{p}_k^m - \mathbf{p}_{k-1}^m\|_2 \approx \|\mathbf{p}_{k-1}^m - \mathbf{p}_{k-1}^0\|_2 + |\mathbf{v}_{k-1}^m| T \cos \theta, \quad (6.5)$$

where  $|\mathbf{v}_{k-1}^m|$  is the magnitude of the target velocity vector and  $\theta$  is the angle between the DOA and target velocity vectors. Now, since  $|\mathbf{v}_{k-1}^m| \cos \theta = \langle \mathbf{u}_{k-1}, \mathbf{v}_{k-1}^m \rangle$ , we can

rewrite (6.5) as

$$\|\mathbf{p}_k^m - \mathbf{p}_k^0\|_2 \approx \|\mathbf{p}_{k-1}^m - \mathbf{p}_{k-1}^0\|_2 + T \langle \mathbf{u}_{k-1}, \mathbf{v}_{k-1}^m \rangle, \quad (6.6)$$

and hence

$$\begin{aligned} \tau_k^m &= \frac{2}{c} \|\mathbf{p}_k^m - \mathbf{p}_k^0\|_2 \approx \frac{2}{c} \|\mathbf{p}_{k-1}^m - \mathbf{p}_{k-1}^0\|_2 + T \left( \frac{2}{c} \langle \mathbf{u}_{k-1}, \mathbf{v}_{k-1}^m \rangle \right), \\ &= \tau_{k-1}^m + T \beta_{k-1}^m + T \beta_{k-1}^r, \end{aligned} \quad (6.7)$$

where  $\beta_{k-1}^r \triangleq (2/c) \langle \mathbf{u}_{k-1}, \mathbf{v}_{k-1}^0 \rangle$  denotes the Doppler effect only due to the motion of the radar, which is obviously known to the radar. Then, combining (6.4) and (6.7), we get a modified state dynamic model, in terms of the delay and Doppler parameters of the target, as

$$\bar{\boldsymbol{\zeta}}_k^m = \begin{bmatrix} 1 & T \\ 0 & 1 \end{bmatrix} \bar{\boldsymbol{\zeta}}_{k-1}^m + \begin{bmatrix} T \\ 0 \end{bmatrix} \beta_{k-1}^r + \bar{\mathbf{w}}_k^m, \quad (6.8)$$

where  $\bar{\mathbf{w}}$  represents the model error associated with the approximations involved in (6.4) and (6.7).

## 6.2.2 Measurement Model

We consider an OFDM signalling system with  $\mathbf{a} = [a_0, a_1, \dots, a_{L-1}]^T$  representing the complex transmit-weights over the  $L$  subcarriers, as previously described in (2.1) – (2.4). Then, similar to (3.1), the received signal due to only the  $l$ -th



subcarrier at the  $k$ -th pulse interval can be written as

$$\tilde{y}_l(t, \bar{\boldsymbol{\zeta}}_k) = \sum_{m=1}^M x_l^m \tilde{s}_l(\gamma_k^m(t - \tau_k^m)) + \tilde{e}_l(t), \quad \text{when } T \leq t < T_p, \quad (6.9)$$

where all the notations have the same interpretations as described in reference to (3.1), but modified to include multiple targets.

Next, denoting an indicator function as  $I_m(t) = I(\gamma_k^m(t - \tau_k^m))$ , which is nonzero only when  $\tau_k^m \leq t < \tau_k^m + T/\gamma_k^m$ , we obtain the complex envelope of the received signal at the output of the  $l$ -th subchannel (similar to (3.3)) as

$$y_l(t_n, \bar{\boldsymbol{\zeta}}_k) = \sum_{m=1}^M a_l x_l^m \phi_l(t_n, \tau_k^m, \beta_k^m) + e_l(t_n), \quad \text{for } l = 0, \dots, L-1, \quad n = 0, \dots, N-1 \quad (6.10)$$

where

- $\phi_l(\cdot)$  is defined as

$$\begin{aligned} \phi_l(t_n, \tau_k^m, \beta_k^m) &\triangleq e^{-j2\pi f_l(1+\beta_k^m)\tau_k^m} e^{j2\pi f_l \beta_k^m t_n} I_{[\tau_k^m]}(t_n), \\ &= e^{-j2\pi f_l \tau_k^m} e^{j2\pi f_l \beta_k^m (t_n - \tau_k^m)} I_{[\tau_k^m]}(t_n). \end{aligned} \quad (6.11)$$

- $N$  denotes the number of temporal samples per pulse transmission, covering the range of delays corresponding to a region of interest ( $T < t_0 < t_1 < \dots < t_{N-1} < T_p$ ).
- The sampling interval or time resolution  $\Delta t \triangleq t_i - t_{i-1}$  depends on the bandwidth of the signal transmitted by the radar; i.e.,  $\Delta t = 1/(2B) = T/(2(L+1))$ .

- Assuming  $T/\gamma_k^m \approx T$ , the indicator function  $I_{[\tau_k^m]}(t_n)$  can be represented as an approximated version of  $I_m(t)$  in the discrete-time domain; i.e.,

$$I_{[\tau_k^m]}(t_n) = \begin{cases} 1, & \text{when } \tau_k^m \leq t_n < \tau_k^m + T \\ 0, & \text{otherwise} \end{cases}. \quad (6.12)$$

- $e_l(t_n)$  represents an aggregation of any static clutter returns, co-channel interference, and measurement noise at baseband.

From the definition of  $I_{[\tau_k^m]}(t_n)$ , we find that for each target there will be  $N_s \triangleq T/\Delta t = 2(L + 1)$  temporal samples corresponding to target returns plus clutter and noise. For example, in (6.10) the  $m$ -th target responses will be found at  $n = n^m, n^m + 1, \dots, n^m + N_s - 1$ , where  $n^m = \lceil \tau_k^m / \Delta t \rceil - t_0 / \Delta t$ . Hence, out of the total  $N$  temporal measurements, at most  $MN_s$  samples will bear the target responses along with the clutter and noise, while the rest of  $N - MN_s$  samples will correspond to only clutter and noise.

Stacking the measurements of all subchannels into one vector of length  $L$ , we get

$$\mathbf{y}(t_n, \bar{\boldsymbol{\zeta}}_k) = \sum_{m=1}^M \boldsymbol{\Phi}(t_n, \tau_k^m, \beta_k^m) \mathbf{A} \mathbf{x}^m + \mathbf{e}(t_n), \quad (6.13)$$

where

- $\mathbf{y}(t_n, \bar{\boldsymbol{\zeta}}_k) = [y_0(t_n, \bar{\boldsymbol{\zeta}}_k), y_1(t_n, \bar{\boldsymbol{\zeta}}_k), \dots, y_{L-1}(t_n, \bar{\boldsymbol{\zeta}}_k)]^T$ .
- $\boldsymbol{\Phi}(t_n, \tau_k^m, \beta_k^m) = \text{diag}(\phi_0(t_n, \tau_k^m, \beta_k^m), \phi_1(t_n, \tau_k^m, \beta_k^m), \dots, \phi_{L-1}(t_n, \tau_k^m, \beta_k^m))$  is an  $L \times L$  matrix containing the delay and Doppler information of the  $m$ -th target.

- $\mathbf{A} = \text{diag}(\mathbf{a})$  is an  $L \times L$  complex diagonal matrix that contains the transmitted weights  $\mathbf{a}$ .
- $\mathbf{x}^m = [x_0^m, x_1^m, \dots, x_{L-1}^m]^T$  is an  $L \times 1$  vector having the scattering coefficients of the  $m$ -th target over all  $L$  subchannels.
- $\mathbf{e}(t_n) = [e_0(t_n), e_1(t_n), \dots, e_{L-1}(t_n)]^T$  is an  $L \times 1$  vector composed of any static clutter returns, measurement noise, or co-channel interference.

Then, concatenating all the temporal data columnwise into a long column vector of length  $LN$ , we obtain the OFDM measurement model at the  $k$ -th pulse interval as

$$\mathbf{y}_k = \sum_{m=1}^M \bar{\Phi}(\tau_k^m, \beta_k^m) \mathbf{A} \mathbf{x}^m + \mathbf{e}_k, \quad (6.14)$$

where

- $\mathbf{y}_k = [\mathbf{y}(t_0, \bar{\zeta}_k)^T, \mathbf{y}(t_1, \bar{\zeta}_k)^T, \dots, \mathbf{y}(t_{N-1}, \bar{\zeta}_k)^T]^T$ .
- $\bar{\Phi}(\tau_k^m, \beta_k^m) = [\Phi(t_0, \tau_k^m, \beta_k^m)^T \dots \Phi(t_{N-1}, \tau_k^m, \beta_k^m)^T]^T$  is an  $LN \times L$  matrix containing the delay and Doppler information of the  $m$ -th target.
- $\mathbf{e}_k = [\mathbf{e}(t_0)^T, \mathbf{e}(t_1)^T, \dots, \mathbf{e}(t_{N-1})^T]^T$  is an  $LN \times 1$  vector comprising static clutter returns, measurement noise, and interference.

Hence, with respect to our modified state vector  $\bar{\zeta}_k^m = [\tau_k^m, \beta_k^m]^T$ , the measurement vector  $\mathbf{y}_k$  in (6.14) depends on the state variables at the  $k$ -th pulse interval through the matrix  $\bar{\Phi}(\cdot)$ , represented as

$$\mathbf{y}_k = \sum_{m=1}^M \bar{\Phi}(\bar{\zeta}_k^m) \mathbf{A} \mathbf{x}^m + \mathbf{e}_k. \quad (6.15)$$

## 6.3 Sparse Modeling

Exploiting the inherent sparsity on the delay-Doppler plane, we develop an equivalent sparse representation of our OFDM measurement model (6.14). Due to the multi-carrier OFDM signal, the resultant model shows block-sparsity properties. Hence, in the following, we first present a brief overview of block sparsity. Then we construct our block-sparse equivalent model and discuss the properties of the corresponding block-sparse measurement matrix.

### 6.3.1 Block Sparsity

There are certain practical scenarios in which the sparse vector displays some additional structures. For example, the nonzero entries can appear in blocks (or clusters) instead of spreading out arbitrarily throughout the sparse vector. Such vectors are referred to as block sparse [88] – [90]. Assuming equal block length  $b$ , a block-sparse vector  $\mathbf{s}$  of dimension  $P \times 1$  can be represented as a concatenation of  $Q$  blocks of entries; i.e.,

$$\mathbf{s} = \left[ \underbrace{s_1, \dots, s_b}_{\mathbf{s}^{(1)T}}, \underbrace{s_{b+1}, \dots, s_{2b}}_{\mathbf{s}^{(2)T}}, \dots, \underbrace{s_{P-b+1}, \dots, s_P}_{\mathbf{s}^{(Q)T}} \right]^T, \quad (6.16)$$

where  $P = Qb$ . Then, the measurement matrix  $\mathcal{A}$  of dimension  $R \times P$  can also be represented as a concatenation of  $Q$  blocks of columns (each block representing a submatrix of dimension  $R \times b$ ); i.e.,

$$\mathcal{A} = \left[ \underbrace{\mathbf{a}_1 \cdots \mathbf{a}_b}_{\mathcal{A}^{(1)}} \underbrace{\mathbf{a}_{b+1} \cdots \mathbf{a}_{2b}}_{\mathcal{A}^{(2)}} \cdots \underbrace{\mathbf{a}_{P-b+1} \cdots \mathbf{a}_P}_{\mathcal{A}^{(Q)}} \right]. \quad (6.17)$$

The vector  $\mathbf{s}$  is called block  $S$ -sparse if  $\mathbf{s}(q)$  has nonzero Euclidean norm at no more than  $S$  indices  $q$ , where  $q = 1, 2, \dots, Q$ . As in [88] – [90], if we denote the number of nonzero block-entries as

$$\|\mathbf{s}\|_{2,0} = \sum_{q=1}^Q I(\|\mathbf{s}(q)\|_2 > 0), \quad (6.18)$$

where  $I(\cdot)$  denotes an indicator function

$$I(\|\mathbf{s}(q)\|_2 > 0) = \begin{cases} 1, & \text{if } \|\mathbf{s}(q)\|_2 > 0 \\ 0, & \text{otherwise} \end{cases},$$

then a block  $S$ -sparse vector  $\mathbf{s}$  is defined as a vector that satisfies  $\|\mathbf{s}\|_{2,0} \leq S$ .

To assess the block-sparse recovery conditions, we must characterize the measurement matrix,  $\mathcal{A}$ , in terms of two different coherence measures: sub-coherence and block-coherence [90]. Sub-coherence captures the local properties by computing the coherence measure within a particular block; i.e.,

$$\nu = \max_q \max_{i,j \neq i} |\mathbf{a}_i^H \mathbf{a}_j|, \quad \text{where } \mathbf{a}_i, \mathbf{a}_j \in \mathcal{A}(q), \quad q = 1, 2, \dots, Q. \quad (6.19)$$

Block-coherence describes the global properties by calculating the coherence measure between two different blocks; i.e.,

$$\mu = \max_{q_1, q_2 \neq q_1} \frac{1}{b} \rho(\mathcal{A}(q_1)^H \mathcal{A}(q_2)), \quad \text{for } q_1, q_2 = 1, 2, \dots, Q, \quad (6.20)$$

where  $\rho(\cdot)$  is the spectral radius.

### 6.3.2 Sparse Measurement Model

Consider that at the  $k$ -th pulse interval we can discretize the possible range of values of delay and Doppler in  $N_\tau$  and  $N_\beta$  grid points, respectively, and denote  $N_G = N_\tau N_\beta$ . Recognizing that each of the  $M$  targets can occupy one such delay-Doppler grid point, we can rewrite (6.14) as

$$\mathbf{y}_k = \sum_{i=1}^{N_\tau} \sum_{j=1}^{N_\beta} \overline{\Phi}(\tau_k^i, \beta_k^j) \mathbf{A} \tilde{\mathbf{x}}^{ij} + \mathbf{e}_k, \quad (6.21)$$

where

$$\tilde{\mathbf{x}}^{ij} = \begin{cases} \mathbf{x}^m, & \text{if } \tau_k^i = \tau_k^m \quad \text{and} \quad \beta_k^j = \beta_k^m \\ 0, & \text{otherwise} \end{cases}. \quad (6.22)$$

Therefore, considering all possible combinations of  $(\tau_k^i, \beta_k^j)$ ,  $i = 1, 2, \dots, N_\tau$ ,  $j = 1, 2, \dots, N_\beta$ , we can form an equivalent sparse measurement model as

$$\mathbf{y}_k = \tilde{\Phi}_k \tilde{\mathbf{x}} + \mathbf{e}_k, \quad (6.23)$$

where

- $\tilde{\mathbf{x}}$  is an  $LN_G \times 1$  block-sparse vector, having in total  $LM$  nonzero entries, distributed over  $M$  blocks, with each of length  $L$  (i.e., the number of OFDM subcarriers). Hence, the block-sparsity level is equal to the number of targets, i.e.,  $S = M \ll N_G$ .
- $\tilde{\Phi}_k = \left[ \overline{\Phi}(\tau_k^1, \beta_k^1) \cdots \overline{\Phi}(\tau_k^{N_\tau}, \beta_k^{N_\beta}) \right] \otimes \mathbf{A}$  is an  $LN \times LN_G$  matrix representing the block-sparse measurement matrix, with all possible combinations of delay

and Doppler, where each block of columns,  $\overline{\Phi}(\tau_k^i, \beta_k^j) \mathbf{A}$ ,  $i = 1, 2, \dots, N_\tau$ ,  $j = 1, 2, \dots, N_\beta$ , is of dimensions  $LN \times L$ .

### 6.3.3 Properties of the Measurement Matrix and Coherence Measures

In this subsection, we study the properties of the block-sparse measurement matrix  $\tilde{\Phi}_k$  and associated coherence measures under the following two categories.

#### Within a Block

Within any  $(i, j)$ -th block of columns of the measurement matrix, the  $l$ -th column has the following form:

$$[0, \dots, \underbrace{a_l \phi_l(t_0, \tau_k^i, \beta_k^j)}_{\text{index } =l}, 0, \dots, \underbrace{a_l \phi_l(t_1, \tau_k^i, \beta_k^j)}_{\text{index } =2l}, 0, \dots, \underbrace{a_l \phi_l(t_{N-1}, \tau_k^i, \beta_k^j)}_{\text{index } =Nl}, \dots, 0]^T, \quad (6.24)$$

where  $\phi_l(\cdot)$  is defined in (6.11). As explained before in Section 6.2.2, the responses of a target will be found only at  $N_s$  temporal samples, denoted as  $n = n^i, n^i + 1, \dots, n^i + N_s - 1$ , where  $n^i = \lceil \tau_k^i / \Delta t \rceil - t_0 / \Delta t$ . Hence, the terms  $a_l \phi_l(t_n, \tau_k^i, \beta_k^j)$  will be zero for all other temporal points.

**Property 1. Column-norm:** The norm of the  $l$ -th column is given as

$$\begin{aligned} n_{\text{col}}(l) &= \sqrt{\sum_{n=0}^{N-1} (a_l \phi_l(t_n, \tau_k^i, \beta_k^j))^* (a_l \phi_l(t_n, \tau_k^i, \beta_k^j))} = \sqrt{\sum_{n=n^i}^{n^i+N_s-1} |a_l|^2} \\ &= \sqrt{N_s} |a_l| = \sqrt{2(L+1)} |a_l|, \quad \text{for } l = 0, \dots, L-1. \end{aligned} \quad (6.25)$$

**Property 2. Sub-coherence:** From the structure of (6.24), it is evident that the columns within a particular block are orthogonal to each other, and hence from (6.19) we find that the sub-coherence of  $\tilde{\Phi}_k$  is zero, i.e.,

$$\nu = 0. \quad (6.26)$$

### Between Two Different Blocks

For two separate blocks of columns (either  $i \neq i'$  or  $j \neq j'$ ) of the measurement matrix, we get

$$\left[ \overline{\Phi}(\tau_k^i, \beta_k^j) \mathbf{A} \right]^H \left[ \overline{\Phi}(\tau_k^{i'}, \beta_k^{j'}) \mathbf{A} \right] = \mathbf{A}^H \mathbf{Q} \mathbf{A}, \quad \text{for } i, i' = 1, \dots, N_\tau, j, j' = 1, \dots, N_\beta \quad (6.27)$$

where  $\mathbf{Q}$  is an  $L \times L$  diagonal matrix having the following form [see Appendix E for the derivation]

$$\mathbf{Q} = \text{diag} \left( \dots, \alpha(l) e^{j 2\pi \theta(l)}, \dots \right), \quad l = 0, 1, \dots, L - 1, \quad (6.28)$$

and

$$\begin{aligned} \alpha(l) &= \tilde{N} \text{sinc} \left( \tilde{N} f_l (\beta_k^j - \beta_k^{j'}) \Delta t \right) \approx \tilde{N} = N_s - (n^{i'} - n^i), \\ \theta(l) &= f_l \left[ (1 + \beta_k^j) \tau_k^i - (1 + \beta_k^{j'}) \tau_k^{i'} - (\beta_k^j - \beta_k^{j'}) (t_{n^{i'}} + t_{n^i + N_s - 1}) / 2 \right], \end{aligned}$$

with  $n^i = \lceil \tau_k^i / \Delta t \rceil - t_0 / \Delta t$  and  $n^{i'} = \lceil \tau_k^{i'} / \Delta t \rceil - t_0 / \Delta t$ . Therefore, from the definitions of  $\mathbf{A}$  and  $\mathbf{Q}$ , it follows that  $\mathbf{A}^H \mathbf{Q} \mathbf{A}$  is also an  $L \times L$  diagonal matrix whose eigenvalues



are equal to the entries on the main diagonal; i.e.,

$$\lambda_l(\mathbf{A}^H \mathbf{Q} \mathbf{A}) = |a_l|^2 \alpha(l) e^{j 2\pi \theta(l)}, \quad \text{for } l = 0, 1, \dots, L-1, \quad (6.29)$$

and hence the corresponding spectral radius is

$$\begin{aligned} \rho(\mathbf{A}^H \mathbf{Q} \mathbf{A}) &= \max_l |a_l|^2 |\alpha(l)|, \\ &\approx \left[ N_s - (n^{i'} - n^i) \right] \max_l |a_l|^2, \\ &= \left[ 2(L+1) - (n^{i'} - n^i) \right] \max_l |a_l|^2. \end{aligned} \quad (6.30)$$

**Property 3. Block-coherence:** From (6.20) and (6.30), we compute the block-coherence of  $\tilde{\Phi}_k$  as

$$\begin{aligned} \mu &= \max_{\substack{(i,j),(i',j'): \\ i \neq i' \text{ OR } j \neq j'}} \frac{1}{L} \left[ 2(L+1) - (n^{i'} - n^i) \right] \max_l |a_l|^2, \\ &= \frac{2(L+1)}{L} \max_l |a_l|^2, \quad \text{when } i = i' \text{ but } j \neq j'. \end{aligned} \quad (6.31)$$

### 6.3.4 Minimizing the Block-Coherence

The block-coherence measure,  $\mu$ , of the block-sparse system matrix in (6.23) plays a role similar to the coherence of the conventional sparse measurement matrix. Therefore, to maximize accuracy in the sparse-recovery, it is desirable to have its value as small as possible. To minimize the value of  $\mu$ , we have to minimize the effect of  $\max_l |a_l|^2$  in the numerator of (6.31). The minimum value of  $\mu$  can be achieved when we transmit equal amounts of energy over all the OFDM subcarriers, i.e.,  $|a_l|^2 = 1/L, \forall l$ . This is the consequence of the following theorem.

**Theorem 3.** Given  $L$  complex coefficients  $\{a_0, \dots, a_{L-1}\}$  such that  $\sum_{l=0}^{L-1} |a_l|^2 = 1$ ,

$$\min_{\{a_0, \dots, a_{L-1}\}} \max_l |a_l|^2 = \frac{1}{L},$$

and it is achievable when  $|a_l|^2 = 1/L \forall l$ .

*Proof.* Contrary to the statement of the theorem, assume that it is possible to select  $a_l$ 's in such a way that  $\max_l |a_l|^2 < 1/L$ . However, from the constraint equation  $\sum_{l=0}^{L-1} |a_l|^2 = 1$  we note that if  $|a_l|^2 < 1/L$  is satisfied for any  $l$ , then there would exist at least another  $l'$  for which  $|a_{l'}|^2 > 1/L$ , and therefore  $\max_l |a_l|^2 < 1/L$  would not be satisfied. Hence, the minimum value of  $\max_l |a_l|^2$  could be only  $1/L$ , and that could be achieved when  $|a_l|^2 = 1/L \forall l$ .  $\square$

Therefore, considering one of the simplest choices with  $a_l = 1/\sqrt{L} \forall l$ , we can write a modified version of (6.23) as

$$\mathbf{y}_k = \tilde{\Phi}_k \tilde{\mathbf{x}} + \mathbf{e}_k, \quad (6.32)$$

where  $\tilde{\Phi}_k = (1/\sqrt{L}) \left[ \bar{\Phi}(\tau_k^1, \beta_k^1) \cdots \bar{\Phi}(\tau_k^{N_\tau}, \beta_k^{N_\beta}) \right]$ . Consequently, the block-coherence of this modified version of the block-sparse measurement matrix,  $\tilde{\Phi}_k$ , becomes  $\tilde{\mu} = 2(L+1)/L^2$ .

Note that  $\tilde{\mu} = 2(L+1)/L^2$  implies that it would be advantageous to increase the value of  $L$  (i.e., the number of OFDM subcarriers) as much as possible. However, given a fixed bandwidth of operation, as we increase the value of  $L$ , the subcarrier spacing  $\Delta f$  decreases, i.e., two adjacent subcarriers come closer to each other on the frequency axis. Then it may happen that the variations of the target responses

become insignificant over the adjacent subcarriers, and hence we do not achieve any improvement. Therefore, the value of  $L$  is to be chosen as a compromise between the expected variability of the target responses over different frequencies and the block-coherence measure of the measurement matrix.

## 6.4 Tracking Filter

Any tracking procedure is a sequential method consisting of repeated applications of two sub-procedures: prediction and update. In the prediction stage, the previous estimated state  $(\bar{\boldsymbol{\zeta}}_{k-1})^+$  is substituted into the state dynamic equation (6.8) to obtain a predicted state  $(\bar{\boldsymbol{\zeta}}_k)^-$  at the  $k$ -th pulse interval. Then, in the update stage, the new measurement  $\mathbf{y}_k$  from (6.15) is used to modify the predicted state  $(\bar{\boldsymbol{\zeta}}_k)^-$  and obtain the estimated state  $(\bar{\boldsymbol{\zeta}}_k)^+$  at the  $k$ -th pulse interval.

To exploit the inherent sparsity on the delay-Doppler plane, we employ a block version of the conventional CoSaMP recovery algorithm, called block-CoSaMP or BCoSaMP, in the update stage. Our approach stems from [195, Algo. 1]. From the discussion in the previous section, we notice that the sparse vector in our model shows a block structure, which is important to incorporate in the recovery algorithm. The simple and iterative greedy structure of the conventional CoSaMP algorithm helps us to easily integrate the block-sparsity nature of the sparse vector into our algorithm, the pseudocode of which is given in Table 6.1.

For the notations used in Table 6.1, please refer to Section 6.3.1 and [91]. Given a vector  $\mathbf{s}$  of length  $P$ ,  $\mathbf{s}_{[S]}$  denotes another vector, having the same length, that is formed by restricting  $\mathbf{s}$  to those  $S$  blocks of components that have largest Euclidean

Table 6.1: BCoSaMP Recovery Algorithm

<b>Inputs:</b> System matrix $\tilde{\Phi}_k$ , measurement vector $\mathbf{y}_k$ , block-sparsity level $S$ .	
<b>Output:</b> A block $S$ -sparse estimation $(\tilde{\zeta}_k)^+$ of the true state vector $\tilde{\zeta}_k$ .	
<b>Initializations:</b>	
$\hat{\zeta}_0 = (\tilde{\zeta}_k)^-$	{ Initial estimate as the predicted state }
$\mathbf{r} = \mathbf{y}_k$	{ Initial residue as the current measurement }
$i = 0$	
<b>repeat</b>	
$i \leftarrow i + 1$	
$\mathbf{p} \leftarrow \tilde{\Phi}_k^H \mathbf{r}$	{ Form state proxy }
$\Omega \leftarrow \text{bsupp}(\mathbf{p}_{[2S]})$	{ Identify the $2S$ largest blocks of the proxy }
$T \leftarrow \Omega \cup \text{bsupp}(\hat{\zeta}_{i-1})$	{ Merge block-supports }
$\mathbf{b} _T \leftarrow (\tilde{\Phi}_k)_T^\dagger \mathbf{y}_k, \mathbf{b} _{T^c} \leftarrow \mathbf{0}$	{ Form state estimate by least-squares }
$\hat{\zeta}_i \leftarrow \mathbf{b} _{[S]}$	{ Prune to get block $S$ -sparse approximation }
$\mathbf{r} \leftarrow \mathbf{y}_k - \tilde{\Phi}_k \hat{\zeta}_i$	{ Update the residue }
<b>until</b> halting criterion <i>true</i>	
<b>return</b> $(\tilde{\zeta}_k)^+ = \hat{\zeta}_i$	

norms. In other words,  $\mathbf{s}_{[S]}$  corresponds to the best block  $S$ -sparse approximation of  $\mathbf{s}$ . If  $\mathbf{s}$  has blocks of equal length  $b$ , then  $\mathbf{s}_{[S]}$  will have  $bS$  nonzero components. Denoting  $T$  as a subset of  $\{1, 2, \dots, Q\}$ , we define a restriction of the vector,  $\mathbf{s}|_T$ , and a restriction of the measurement matrix,  $(\tilde{\Phi}_k)_T$ , as the blocks of components and blocks of columns, respectively, whose block-indices are specified by the set  $T$ . We define the block support of the vector  $\mathbf{s}$  as the set of block-indices where the block-norm is not zero; i.e.,

$$\text{bsupp}(\mathbf{s}) = \{q : \|\mathbf{s}(q)\|_2 > 0\}.$$

Finally, as the halting criterion we use the difference in norms of the residue vectors at two consecutive iterations. Whenever that difference is smaller than a pre-defined threshold value, we stop the algorithm.

## 6.5 Numerical Results

We present the results of several numerical examples to demonstrate the performance of our proposed sparsity-based tracking approach. First, we provide a description of the simulation setup, and then discuss different numerical examples.

Fig. 6.3 schematically describes a scenario that we used in the simulations. The radar was at height  $z = 1$  km above the ground and moving with a velocity  $33.33 (= 33.33 \hat{j})$  m/s, which is approximately 120 kph. We considered that it was looking over an area whose center was at  $(x, y) = (3, 2)$  km. There were two moving targets within the region of interest, which was designated by a range of roundtrip delays  $(t_0, t_{N-1})$  with  $N = 120$ . Any other backscattering from ground-based objects were considered as static clutter returns (with respect to the radar). In our simulation, we kept the SNR fixed at 10 dB. Assuming the noise  $\mathbf{e}(t_n)$  in (6.13) to be a zero-mean Gaussian vector with covariance matrix  $\mathbf{\Sigma}$ , and temporally independent, we defined the SNR as

$$\text{SNR} = \frac{(1/N) \sum_{n=0}^{N-1} \left\| \sum_{m=1}^M \mathbf{\Phi}(t_n, \tau_k^m, \beta_k^m) \mathbf{A} \mathbf{x}^m \right\|_2^2}{\text{tr}(\mathbf{\Sigma})}. \quad (6.33)$$

The details of the target and radar parameters are as follows:

- Target parameters:

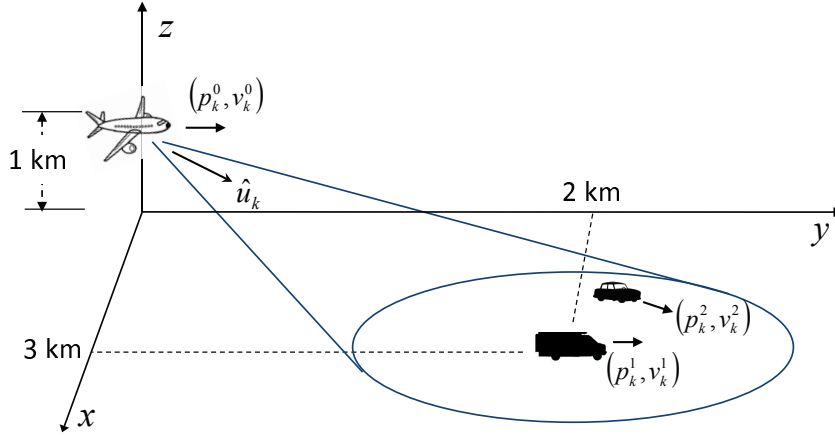


Figure 6.3: A schematic representation of the simulation scenario (not drawn to scale).

- The first target started at a position  $(x_0^1, y_0^1, z_0^1) = (3000, 2000, 0)$  m and was moving with a velocity of  $16.67 (= 16.67 \cos(5^\circ) \hat{i} + 16.67 \sin(5^\circ) \hat{j})$  m/s, which is approximately 60 kph. The scattering parameters of this target were assumed to be the same for all subchannels, i.e.,  $\mathbf{x}^1 = [1, 1, 1, 1]^T$ .
- The second target started at a position  $(x_0^2, y_0^2, z_0^2) = (3010, 2006, 0)$  m and was moving with a velocity of  $12.5 (= 12.5 \cos(-5^\circ) \hat{i} + 12.5 \sin(-5^\circ) \hat{j})$  m/s, which is approximately 45 kph. The scattering parameters of the second target were assumed to be quite different across the subchannels, i.e.,  $\mathbf{x}^2 = [0.01, 0.5, 1.1, 1.6]^T$ .
- Radar parameters:
  - Carrier frequency  $f_c = 1$  GHz.
  - Total bandwidth  $B = 100$  MHz.
  - Number of OFDM subcarriers  $L = 4$ .
  - Subcarrier spacing  $\Delta f = B/(L + 1) = 20$  MHz.
  - Pulse width  $T = 1/\Delta f = 50$  ns.

- Pulse repetition interval  $T_p = 10$  ms.
- All the transmitted OFDM weights were equal, i.e.,  $\mathbf{a} = (1/\sqrt{L})\mathbf{1}_L$ .

We used the BCoSaMP algorithm, as described in Section 6.4, to track the targets, and compared the resultant tracking performance with that of a particle filter (PF). The following are some specific parameterizations used in these two approaches:

- Sparsity-based approach:
  - To partition the delay-Doppler plane, we used the regular (uniform) grids having a delay resolution of  $\Delta\tau = 3.33$  ns (i.e., corresponding to a range grid of 0.5 m) and a Doppler resolution of  $\Delta\beta = 2.46 \times 10^{-9}$  (i.e., corresponding to a velocity grid of 1 m/s).
  - Instead of using all the possible delay-Doppler grids for every pulse interval, we dynamically partitioned a small portion of the delay-Doppler plane at a particular pulse interval. This could be done because at every pulse interval the predicted state provides a rough approximation of the new estimated state. Therefore, we first used (6.8) to compute the predicted values of delay,  $(\tau_k^m)^-$ , and Doppler,  $(\beta_k^m)^-$ , for both the targets at the  $k$ -th pulse interval. Then, to form the grids, we selected a small region of the delay-Doppler plane as

$$\mathcal{R} := \bigcup_{i=1,2} [(\tau_k^i)^- - \bar{\tau}/2, (\tau_k^i)^- + \bar{\tau}/2] \times [(\beta_k^i)^- - \bar{\beta}/2, (\beta_k^i)^- + \bar{\beta}/2] \quad (6.34)$$

where  $\bar{\tau}$  and  $\bar{\beta}$  defined the total possible area around  $((\tau_k^i)^-, (\beta_k^i)^-)$  in which we expected to get the state estimates at the  $k$ -th pulse.

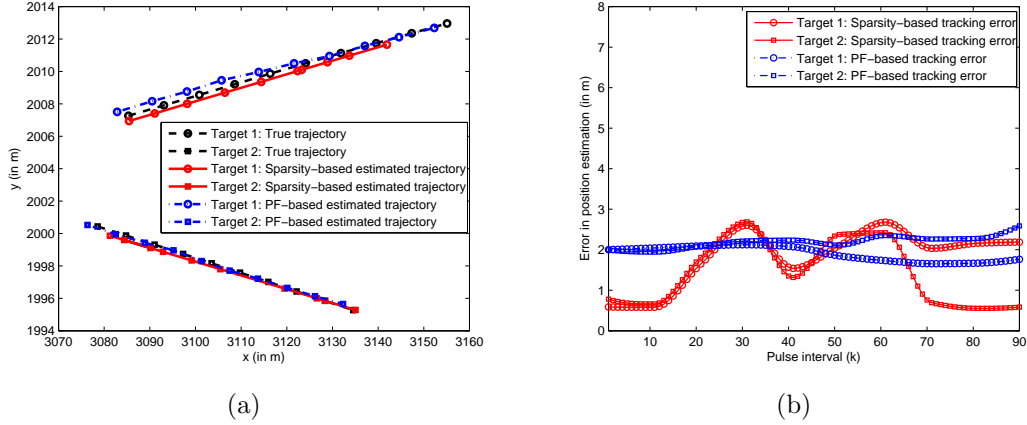


Figure 6.4: Comparison of the (a) true and estimated trajectories and (b) associated root-mean-squared errors in position estimation of two non-crossing target paths using the sparsity-based and PF-based tracking algorithms.

- Note here that the choice of the values of  $\bar{\tau}$  and  $\bar{\beta}$  depends mainly on two factors: the SNR of the measurement scenario and relative length of the sparse vector with the actual sparsity level. For example, in a low SNR condition we would like to choose larger values of  $\bar{\tau}$  and  $\bar{\beta}$ , which however increase the length of the sparse vector. Then, it becomes inefficient to estimate a few nonzero values from a lengthier sparse vector. On the contrary, if we reduce the length of the sparse vector, i.e., we choose smaller values of  $\bar{\tau}$  and  $\bar{\beta}$  and hence a smaller region  $\mathcal{R}$ , then the true values of the state variables might lie outside  $\mathcal{R}$  and this dynamic grid-based approach would fall apart. In our simulations, we chose  $\bar{\tau} = 40\Delta\tau$  and  $\bar{\beta} = 4\Delta\beta$ .

- Particle filter approach:

- We used an augmented state vector in which we incorporated the scattering coefficients of the targets along with their positions and velocities. The temporal evaluation of the scattering coefficients was assumed to be



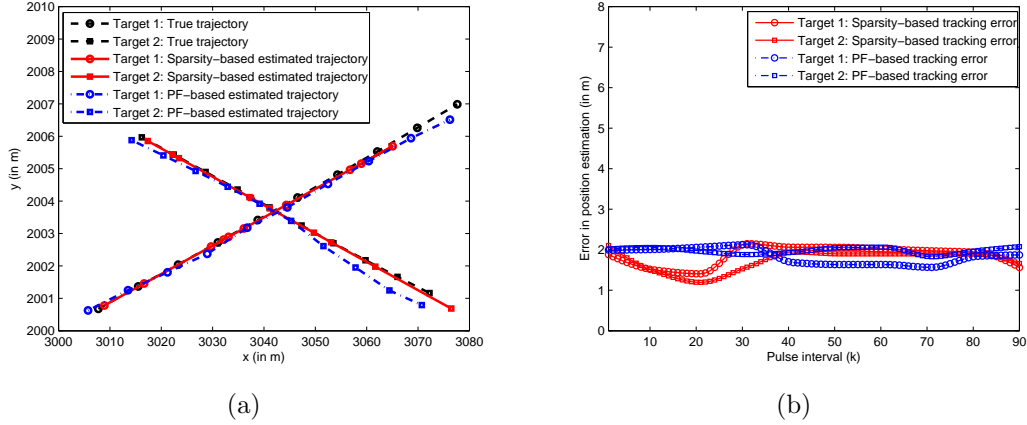


Figure 6.5: Comparison of the (a) true and estimated trajectories and (b) associated root-mean-squared errors in position estimation of two crossing target paths using the sparsity-based and PF-based tracking algorithms.

constant, i.e.,  $\mathbf{x}^m(k) = \mathbf{x}^m(k-1)$ ,  $m = 1, 2$ . This assumption is in general true when the target is far away from the radar, as in our case.

- Both the state and measurement noise processes were assumed to be zero-mean Gaussian processes.
- The state particles were generated from an importance density function, which we chose to be the transitional prior  $p\left(\zeta_k^{(i)}|\zeta_{k-1}^{(i)}\right)$ ,  $i = 1, 2, \dots, N_\zeta$ , where  $N_\zeta$  was the number of state particles. In our simulations, we considered  $N_\zeta = 800$  state particles.
- The importance weights were formulated as  $w_k^{(i)} \propto w_{k-1}^{(i)} p\left(\mathbf{y}_k|\zeta_k^{(i)}\right)$ .

Figs. 6.4 and 6.5 depict the tracking performance and associated root-mean-squared errors in position estimation for two non-crossing and crossing target paths, respectively. It is evident from these plots that, compared to the PF-based approach, the sparsity-based tracking approach provided equivalent tracking performances, and particularly even better when the target paths do not cross. In addition, our sparsity-based

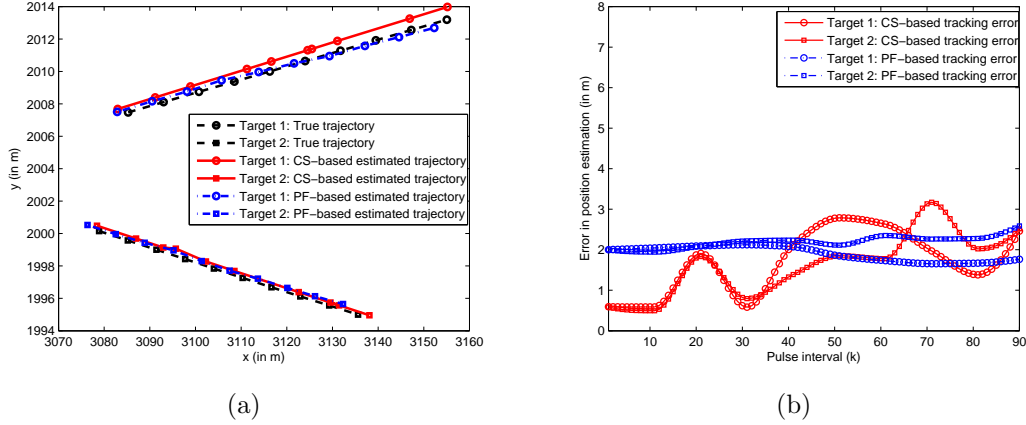


Figure 6.6: Comparison of the (a) true and estimated trajectories and (b) associated root-mean-squared errors in position estimation of two non-crossing target paths using the sparsity-based (with 50% measurements) and PF-based tracking algorithms.

approach provided estimation results much quicker than the PF-based algorithm. We found that on average the PF-based approach took 131.25 s to estimate the target state per pulse interval; whereas the sparsity-based technique took only 17.87 s (for non-crossing target paths) and 6.85 s (for crossing target paths), which was one order less than that of the PF-based tracking. The difference in times in the sparsity-based approach, corresponding to the non-crossing and crossing target paths, occurred due to the dynamic computation of the delay-Doppler grids over region  $\mathcal{R}$ , as specified in (6.34). When the target paths crossed each other, the size of  $\mathcal{R}$  was smaller, and hence it took less time to calculate the grid values.

## Compressive Sensing

To investigate the potential advantage of computational efficiency of compressive sensing (CS), we pre-multiplied the measurement vector in (6.32) with a zero-mean

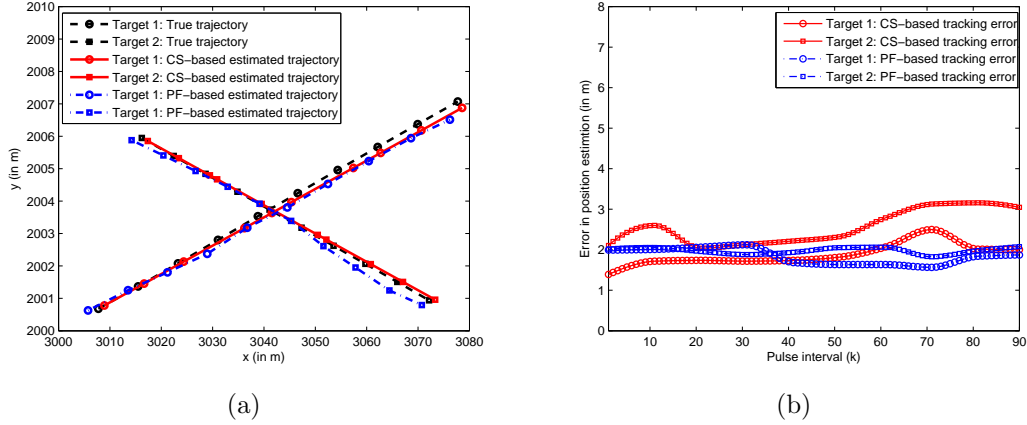


Figure 6.7: Comparison of the (a) true and estimated trajectories and (b) associated root-mean-squared errors in position estimation of two crossing target paths using the sparsity-based (with 50% measurements) and PF-based tracking algorithms.

Gaussian random matrix  $\Psi$  of dimensions  $LN_r \times LN$  ( $N_r < N$ ) as

$$\mathbf{z}_k = \Psi \mathbf{y}_k = \Psi \tilde{\Phi}_k \tilde{\mathbf{x}} + \Psi \mathbf{e}_k. \quad (6.35)$$

Then, we used the compressed measurement vector  $\mathbf{z}_k$ , instead of the original measurements  $\mathbf{y}_k$ , in our sparsity-based tracking algorithm. As before, we compared the resultant performance with that of a PF-based tracking procedure using the original measurements  $\mathbf{y}_k$ .

Figs. 6.6 and 6.7 show the tracking performance and associated root-mean-squared errors in position estimation for two non-crossing and crossing target paths, respectively. For these simulations we worked with only 50% of the total measurements (i.e.,  $N_r = \lceil 0.5N \rceil$ ) in the CS-based tracking technique. Figs. 6.8 and 6.9 represent similar tracking results, apart from the fact that we used only 10% of the total measurements (i.e.,  $N_r = \lceil 0.1N \rceil$ ) in the CS-based tracking. Hence, we observe from these results that our sparsity-based tracking algorithm demonstrated approximately

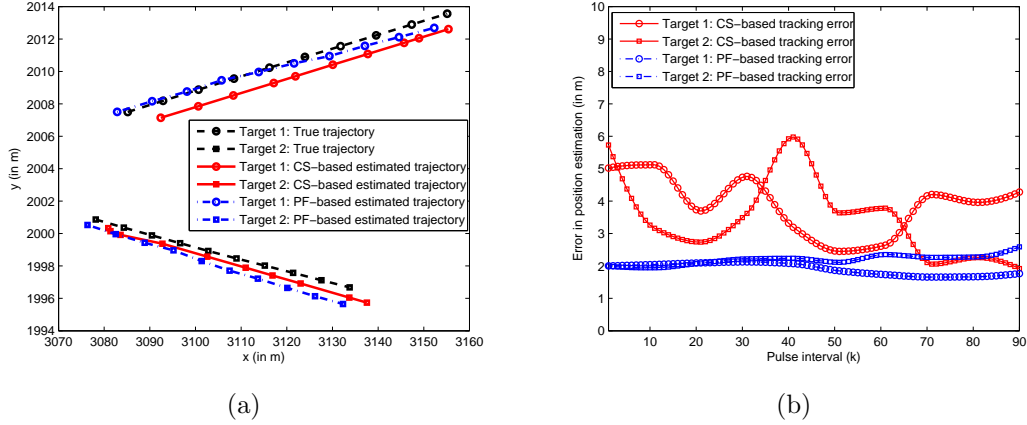


Figure 6.8: Comparison of the (a) true and estimated trajectories and (b) associated root-mean-squared errors in position estimation of two non-crossing target paths using the sparsity-based (with 10% measurements) and PF-based tracking algorithms.

equivalent tracking performance, except when the target paths were crossing, but we still worked with only 10% of all measurements. The advantage of our sparsity-based tracking was even more noticeable in the speed of estimation results, which are tabulated in Table 6.2. As we explained before, the difference of execution times in the sparsity-based approach, corresponding to the non-crossing and crossing target path scenarios, occurred due to the dynamic computation of the delay-Doppler grids.

## 6.6 Summary

We addressed the problem of tracking multiple targets in a region of interest by exploiting sparsity on the delay-Doppler plane (since, the targets lie only at a few delay-Doppler points). In our model, the nonzero components of the sparse vector correspond to the scattering coefficients of the targets at different OFDM subcarriers, and hence we had a block-sparse measurement model. We designed the

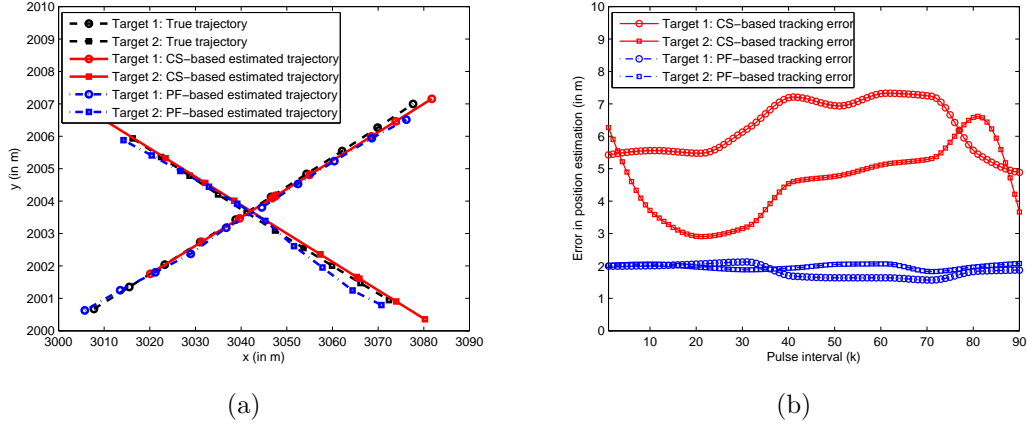


Figure 6.9: Comparison of the (a) true and estimated trajectories and (b) associated root-mean-squared errors in position estimation of two crossing target paths using the sparsity-based (with 10% measurements) and PF-based tracking algorithms.

Table 6.2: Average time (in seconds) to compute the estimated state per pulse interval

Sparsity based tracking			Particle filter based tracking
Fraction of measurements used	Non-crossing target paths	Crossing target paths	131.25
$N_r = N$	17.87	6.85	
$N_r = \lceil 0.5N \rceil$	8.21	4.71	
$N_r = \lceil 0.1N \rceil$	4.69	2.37	

OFDM signal for the minimum block-coherence measure (i.e., maximum accuracy in the sparse-recovery), and proved that is attainable by transmitting equal amounts of energy over all the OFDM subcarriers. In the tracking filter, we used the same block-sparsity property to propose a block version of the CoSaMP algorithm. We presented numerical examples to show the performance of our sparsity-based tracking approach and compared it with the performance of a PF-based tracking procedure. The sparsity-based tracking algorithm took much less time and provided equivalent tracking performance in comparison to the PF-based tracking.

# Chapter 7

## Conclusions

In this dissertation, we employed a wideband OFDM radar signal for target detection and tracking problems. The frequency diversity of the OFDM signal improved the sensing performance as the scattering centers of a target resonate differently at different frequencies. Being a wideband signal, OFDM also improved the range resolution and provided spectral efficiency. In addition, we developed adaptive waveform design techniques to select the spectral parameters of the OFDM signal. In contrast to a conventional system, the adaptive waveform design (in a closed loop) enabled us to achieve better performance by fitting the operational scenario. In the following, we first summarize the key contributions of our work, and then provide some discussion on the possible future work.

### 7.1 Key Contributions

Our key contributions can be summarized as follows:

We first analyzed the OFDM waveform in terms of its wideband ambiguity function (WAF). Here we emphasized that the received signal depends on the scattering parameters of the target. Hence, the corresponding WAF at the output of the matched

filter must include the target responses, along with delay and Doppler. This is different from a conventional formulation of the WAF, which either does not include a scattering coefficient of the target in the received signal model, or assumes identical values for the scattering coefficients at different frequencies. This explicit formulation of WAF in terms of target scattering coefficients enabled us to adaptively design the OFDM signal such that the volume of the corresponding WAF best approximates the volume of a desired ambiguity function over a region in the delay-Doppler plane. The improved delay (range) resolution of the designed OFDM waveform further motivated us to use it for specific radar problems, such as the detection and tracking of targets.

We developed methods for detecting a moving target in the presence of multipath reflections, particularly in urban environments. We exploited the multipath propagation by utilizing multiple Doppler shifts that correspond to the projections of the target velocity on each of the multipath components. We developed a parametric measurement model under the generalized multivariate analysis of variance framework and applied the generalized likelihood ratio test to detect the presence of a target. We adaptively designed the spectral parameter of the OFDM signal by first evaluating the asymptotic performance analysis of the detector and then maximizing the expression of the noncentrality parameter.

Next, we transformed the target-detection problem into the task of sparse-signal spectrum estimation by exploiting both the sparsity of multiple paths and the knowledge of the environment. To estimate the sparse vector we employed a collection of multiple small Dantzig selectors, and used the  $\ell_1$ -constrained minimal singular value of the measurement matrix to analytically evaluate the reconstruction performance. In addition, we proposed a constrained multi-objective optimization (MOO) based algorithm to adaptively design the spectral parameters of the OFDM waveform

by simultaneously minimizing the upper bound on the estimation error to improve the efficiency of sparse-recovery and maximizing the squared Mahalanobis-distance to increase the performance of the underlying detection problem. We applied the nondominated sorting genetic algorithm II to solve our MOO problem.

Then, we developed tracking methods for both a single and multiple targets. For the single-target case, we considered the low-grazing angle tracking, which is one of the most challenging problems in radar due to the ever-changing meteorological conditions in the troposphere, curved surface of the earth, roughness of the sea-surface, etc. We employed a co-located multiple-input multiple-output radar configuration with polarization-sensitive transceivers to achieve the waveform diversity and to better resolve the multipath signals. To track the target, we used a sequential Monte Carlo method and integrated an adaptive waveform design technique based on the maximization of the mutual information between the state and measurement vectors.

For the multi-target tracking problem, we exploited the inherent sparsity on the delay-Doppler plane to develop an efficient tracking procedure. In our model, the nonzero components of the sparse vector appeared in blocks. Hence, in the tracking filter, we utilized the same block-sparsity property to propose a block version of the CoSaMP algorithm. For computational efficiency, instead of using all the possible delay-Doppler grids, we used more prior information to dynamically partition a small portion of the delay-Doppler plane.

## 7.2 Future Work

In our future work, we will extend our model to incorporate more realistic physical phenomena. A multipath environment, for example an urban scene, contains not



only the specular multipath reflection, but also diffractions, refractions, and attenuations due to the sharp edges and corners of buildings or rooftops. Similarly, in a low-grazing angle scenario, multiple horizontally stratified atmospheric layers with different refractivity gradients may exist between the transmitter and receiver pairs. Therefore, it is important to include these underlying physical behaviors into the model as realistically as possible.

We will develop statistical signal processing methods by integrating the detection procedure with the target tracking algorithm. This approach could be useful when the targets appear and disappear within the observation period, particularly in a multipath rich environment. Additionally, we will extend the sparsity-based algorithms to study the effects of nonuniform grids on the delay-Doppler plane.

To design more realistic signals that are particularly suitable for radar applications, we will impose some other constraints in the waveform-optimization problem: constant modulus, limited transmit energy, peak-to-average power ratio (PAPR), and similarity constraint. We will generalize OFDM to nonorthogonal frequency channels using the concept of frames for robustness. We will also check the practical viability of the designed waveform. For example, while using a two-dimensional polarimetric transceiver system, we cannot arbitrarily choose a polarization pair because the practical systems support only horizontal and vertical polarizations. Therefore, in such a case, we can select the relative weights of the horizontal and vertical polarizations to realize different types of signals. Furthermore, we will validate the performance of our proposed techniques with real data.

# Appendix A

In this appendix, we show the derivation of (2.19) as follows:

$$\begin{aligned}\chi_N(\tau, \nu) &= \sqrt{\gamma} \int_{-\infty}^{\infty} \left[ \sum_{n_1=0}^{N-1} s(t - n_1 T_P) e^{j2\pi f_c t} \right] \left[ \sum_{n_2=0}^{N-1} s^*(\gamma(t - \tau) - n_2 T_P) e^{-j2\pi f_c \gamma(t - \tau)} \right] dt \\ &= \sqrt{\gamma} e^{j2\pi f_c \gamma \tau} \sum_{n_1=0}^{N-1} \sum_{n_2=0}^{N-1} \int_{-\infty}^{\infty} s(t - n_1 T_P) s^*(\gamma(t - \tau) - n_2 T_P) e^{-j2\pi \nu t} dt.\end{aligned}$$

Using a change of variable with  $p = t - n_1 T_P$  we get

$$\begin{aligned}\chi_N(\tau, \nu) &= \sqrt{\gamma} e^{j2\pi f_c \gamma \tau} \sum_{n_1=0}^{N-1} \sum_{n_2=0}^{N-1} e^{-j2\pi \nu n_1 T_P} \int_{-\infty}^{\infty} \tilde{s}(p) \tilde{s}^*(\gamma(p + n_1 T_P - \tau) - n_2 T_P) e^{-j2\pi \nu p} dp \\ &= \sum_{n_1=0}^{N-1} \sum_{n_2=0}^{N-1} e^{-j2\pi \nu n_1 T_P} \left[ \sqrt{\gamma} e^{j2\pi f_c \gamma \tau} \int_{-\infty}^{\infty} \tilde{s}(p) \tilde{s}^*(\gamma(p - [\tau + (n_2/\gamma + n_1) T_P])) e^{j2\pi \nu p} dp \right] \\ &= \sum_{n_1=0}^{N-1} \sum_{n_2=0}^{N-1} e^{-j2\pi \nu n_1 T_P} e^{-j2\pi f_c \gamma (n_2/\gamma - n_1) T_P} \\ &\quad \cdot \left[ \sqrt{\gamma} e^{j2\pi f_c \gamma (\tau + (n_2/\gamma - n_1) T_P)} \int_{-\infty}^{\infty} \tilde{s}(p) \tilde{s}^*(\gamma(p - [\tau + (n_2/\gamma + n_1) T_P])) e^{j2\pi \nu p} dp \right].\end{aligned}$$

The term in the square bracket has a similar form as (2.11) when  $\tau$  is replaced with  $[\tau + (n_2/\gamma - n_1) T_P]$ . In addition, the argument of the exponential term outside the square bracket can be simplified as  $\nu n_1 T_P + f_c \gamma (n_2/\gamma - n_1) T_P = f_c (n_2 - n_1) T_P$ . Hence, we get the expression in (2.19).

# Appendix B

In this appendix, we state and prove a theorem that we use to simplify (3.21) to (3.22) and (4.30) to (4.31).

**Theorem 4.** *Suppose  $\mathbf{a} \in \mathbb{C}^L$  is a vector that forms an  $L \times L$  complex diagonal matrix  $\mathbf{A} = \text{diag}(\mathbf{a})$ . Then, we have the following:*

$$\text{tr}(\mathbf{S}_1 \mathbf{A} \mathbf{S}_2 \mathbf{A}^H) = \mathbf{a}^H [\mathbf{S}_2^T \odot \mathbf{S}_1] \mathbf{a}, \quad (\text{B.1})$$

where  $\mathbf{S}_1$  and  $\mathbf{S}_2$  are two square matrices of dimension  $L \times L$ .

*Proof.* First, using the relationship between a trace and vec operator,  $\text{tr}(\mathbf{UV}) = \text{vec}(\mathbf{U}^T)^T \text{vec}(\mathbf{V})$ , we get

$$\text{tr}(\mathbf{S}_1 \mathbf{A} \mathbf{S}_2 \mathbf{A}^H) = \text{tr}(\mathbf{A}^H \mathbf{S}_1 \mathbf{A} \mathbf{S}_2) = \text{vec}((\mathbf{A}^H)^T)^T \text{vec}(\mathbf{S}_1 \mathbf{A} \mathbf{S}_2). \quad (\text{B.2})$$

Then, we apply one of the properties of the vec operator,  $\text{vec}(\mathbf{UQV}) = (\mathbf{V}^T \otimes \mathbf{U}) \text{vec}(\mathbf{Q})$ , to get

$$\text{vec}((\mathbf{A}^H)^T)^T \text{vec}(\mathbf{S}_1 \mathbf{A} \mathbf{S}_2) = \text{vec}((\mathbf{A}^H)^T)^T [\mathbf{S}_2^T \otimes \mathbf{S}_1] \text{vec}(\mathbf{A}). \quad (\text{B.3})$$

Since  $\mathbf{A}$  is a diagonal matrix,  $\text{vec}(\mathbf{A})$  can be written as

$$\text{vec}(\mathbf{A}) = \begin{bmatrix} \mathbf{C}_1 \\ \mathbf{C}_2 \\ \vdots \\ \mathbf{C}_L \end{bmatrix} \mathbf{a}, \quad (\text{B.4})$$

where  $\mathbf{C}_l$  is an  $L \times L$  matrix that has a 1 only at  $(l, l)$ -th position and zero elsewhere. Similarly, we have

$$\text{vec}((\mathbf{A}^H)^T)^T = \text{vec}((\mathbf{A}^*)^T)^T = \mathbf{a}^H \begin{bmatrix} \mathbf{C}_1 \\ \mathbf{C}_2 \\ \vdots \\ \mathbf{C}_L \end{bmatrix}^T. \quad (\text{B.5})$$

Additionally, from [196, Th. 1] we have

$$\begin{bmatrix} \mathbf{C}_1 \\ \mathbf{C}_2 \\ \vdots \\ \mathbf{C}_L \end{bmatrix}^T [\mathbf{S}_2^T \otimes \mathbf{S}_1] \begin{bmatrix} \mathbf{C}_1 \\ \mathbf{C}_2 \\ \vdots \\ \mathbf{C}_L \end{bmatrix} = \mathbf{S}_2^T \odot \mathbf{S}_1. \quad (\text{B.6})$$

Therefore, substituting the results of (B.4)-(B.6) into (B.3) we get

$$\text{vec}((\mathbf{A}^H)^T)^T [\mathbf{S}_2^T \otimes \mathbf{S}_1] \text{vec}(\mathbf{A}) = \mathbf{a}^H [\mathbf{S}_2^T \odot \mathbf{S}_1] \mathbf{a}, \quad (\text{B.7})$$

and hence (B.1) is proved.  $\square$

# Appendix C

In this appendix, we provide a proof of Theorem 2.

Consider vectors  $\mathbf{z}_l \in \mathbb{C}^{PV}$  satisfying

$$s_1(\mathbf{z}_l) = \frac{\|\mathbf{z}_l\|_1^2}{\|\mathbf{z}_l\|_2^2} \leq 4k_l, \quad (\text{C.1})$$

and a long vector  $\mathbf{z} \in \mathbb{C}^{LPV}$  obtained after concatenating these  $\mathbf{z}_l$ s. Then, using the Cauchy-Schwartz inequality, we get

$$\begin{aligned} \|\mathbf{z}\|_1 &= \sum_{l=0}^{L-1} \|\mathbf{z}_l\|_1, \\ &\leq 2 \sum_{l=0}^{L-1} \sqrt{k_l} \|\mathbf{z}_l\|_2, \\ &\leq 2 \sqrt{\sum_{l=0}^{L-1} k_l} \sqrt{\sum_{l=0}^{L-1} \|\mathbf{z}_l\|_2^2}, \\ &= 2 \sqrt{k} \|\mathbf{z}\|_2, \end{aligned}$$

that is,

$$s_1(\mathbf{z}) = \frac{\|\mathbf{z}\|_1^2}{\|\mathbf{z}\|_2^2} \leq 4k. \quad (\text{C.2})$$

As a consequence, for any such constructed  $z$ , we have

$$\rho_{4k}^2(\Phi) \leq \frac{z^H \Phi^H \Phi z}{z^H z} = \sum_{l=0}^{L-1} \frac{z_l^H \Phi_l^H \Phi_l z_l}{z^H z}.$$

Taking a  $z_l$  such that  $\|z_l\|_2^2 = \omega_l \geq 0$  with  $\|z\|_2^2 = \sum_{l=0}^{L-1} \omega_l = 1$ , and

$$\omega_l \rho_{4k_l}^2(\Phi_l) = z_l^H \Phi_l^H \Phi_l z_l,$$

we get

$$\rho_{4k}^2(\Phi) \leq \sum_{l=0}^{L-1} \omega_l \rho_{4k_l}^2(\Phi_l). \quad (\text{C.3})$$

In particular, we have

$$\rho_{4k}^2(\Phi) \leq \rho_{4k_l}^2(\Phi_l). \quad (\text{C.4})$$

Moreover, noticing that  $\lambda_l \leq \lambda$ , we obtain

$$\sum_{l=0}^{L-1} \frac{\lambda_l^2 k_l \sigma^2}{\rho_{4k_l}^4(\Phi_l)} \leq \sum_{l=0}^{L-1} \frac{\lambda^2 k_l \sigma^2}{\rho_{4k}^4(\Phi)} = \frac{\lambda^2 k \sigma^2}{\rho_{4k}^4(\Phi)}. \quad (\text{C.5})$$

# Appendix D

In this appendix, we provide the details of the relationship presented in (4.25), i.e., how to obtain a computable lower bound on the original complex  $\ell_1$ -CMSV.

In (4.24),  $\rho_{4k_l}(\tilde{\Phi}_l)$  corresponds to a solution of the following problem:

$$\min_{\mathbf{z}_l \in \mathbb{C}^{PV}} \mathbf{z}_l^H \tilde{\Phi}_l^H \tilde{\Phi}_l \mathbf{z}_l \quad \text{subject to} \quad \|\mathbf{z}_l\|_1 \leq \sqrt{4k_l}, \quad \|\mathbf{z}_l\|_2 = 1. \quad (\text{D.1})$$

However,  $\mathbf{z}_l$  being a complex vector,  $\|\mathbf{z}_l\|_1 = \sum_{i=1}^{PV} \sqrt{(\text{Re } z_{l,i})^2 + (\text{Im } z_{l,i})^2}$  is not everywhere differentiable with respect to  $\text{Re } \mathbf{z}_l$  and  $\text{Im } \mathbf{z}_l$ . Defining  $\mathbf{g} = \text{Re } \mathbf{z}_l$ ,  $\mathbf{h} = \text{Im } \mathbf{z}_l$ , and  $\Psi_1 = \text{Re } \tilde{\Phi}_l$ ,  $\Psi_2 = \text{Im } \tilde{\Phi}_l$ , we have

$$\mathbf{z}_l^H \tilde{\Phi}_l^H \tilde{\Phi}_l \mathbf{z}_l = \mathbf{g}^T (\Psi_1^T \Psi_1 + \Psi_2^T \Psi_2) \mathbf{g} + \mathbf{h}^T (\Psi_1^T \Psi_1 + \Psi_2^T \Psi_2) \mathbf{h}, \quad (\text{D.2})$$

and note that

$$\|\mathbf{z}_l\|_1 = \sum_{i=1}^{PV} \sqrt{g_i^2 + h_i^2} \geq \frac{\sqrt{2}}{2} \sum_{i=1}^{PV} (|g_i| + |h_i|) = \frac{1}{\sqrt{2}} \left\| [\mathbf{g}^T, \mathbf{h}^T]^T \right\|_1, \quad (\text{D.3})$$

$$\|\mathbf{z}_l\|_2 = \sum_{i=1}^{PV} (g_i^2 + h_i^2) = \left\| [\mathbf{g}^T, \mathbf{h}^T]^T \right\|_2. \quad (\text{D.4})$$

Therefore, we can compute a lower bound on the original complex  $\ell_1$ -CMSV as a solution of the following problem:

$$\begin{aligned} & \min_{\mathbf{g} \in \mathbb{R}^{PV}, \mathbf{h} \in \mathbb{R}^{PV}} \begin{bmatrix} \mathbf{g}^T & \mathbf{h}^T \end{bmatrix} \begin{bmatrix} \Psi_1^T \Psi_1 + \Psi_2^T \Psi_2 & \mathbf{0} \\ \mathbf{0} & \Psi_1^T \Psi_1 + \Psi_2^T \Psi_2 \end{bmatrix} \begin{bmatrix} \mathbf{g} \\ \mathbf{h} \end{bmatrix}, \\ & \text{subject to } \left\| \begin{bmatrix} \mathbf{g} \\ \mathbf{h} \end{bmatrix} \right\|_1 \leq \sqrt{8k_l} \quad \text{and} \quad \left\| \begin{bmatrix} \mathbf{g} \\ \mathbf{h} \end{bmatrix} \right\|_2 = 1. \end{aligned} \quad (\text{D.5})$$

Then, denoting the solution of (D.5) as  $\rho_{8k_l}(\tilde{\Psi})$ , where

$$\tilde{\Psi}^T \tilde{\Psi} = \begin{bmatrix} \Psi_1^T \Psi_1 + \Psi_2^T \Psi_2 & \mathbf{0} \\ \mathbf{0} & \Psi_1^T \Psi_1 + \Psi_2^T \Psi_2 \end{bmatrix},$$

we get

$$\rho_{8k_l}(\tilde{\Psi}) \leq \rho_{4k_l}(\tilde{\Phi}_l). \quad (\text{D.6})$$



# Appendix E

In this appendix, we derive the expressions of  $\mathbf{Q}$ , given in (6.28). From (6.27), we have

$$\begin{aligned} \mathbf{Q} &= \begin{bmatrix} \Phi(t_0, \tau_k^i, \beta_k^j)^H & \Phi(t_1, \tau_k^i, \beta_k^j)^H & \cdots & \Phi(t_{N-1}, \tau_k^i, \beta_k^j)^H \end{bmatrix} \begin{bmatrix} \Phi(t_0, \tau_k^{i'}, \beta_k^{j'}) \\ \Phi(t_1, \tau_k^{i'}, \beta_k^{j'}) \\ \vdots \\ \Phi(t_{N-1}, \tau_k^{i'}, \beta_k^{j'}) \end{bmatrix}, \\ &= \left[ \sum_{n=0}^{N-1} \Phi(t_n, \tau_k^i, \beta_k^j)^H \Phi(t_n, \tau_k^{i'}, \beta_k^{j'}) \right]. \end{aligned}$$

Now, out of total  $N$  temporal points,  $\Phi(t_n, \tau_k^i, \beta_k^j)$  will have non-zero entries corresponding to  $n = n^i, n^i + 1, \dots, n^i + N_s - 1$ , and  $\Phi(t_n, \tau_k^{i'}, \beta_k^{j'})$  will have non-zero entries for  $n = n^{i'}, n^{i'} + 1, \dots, n^{i'} + N_s - 1$ .

Without loss of generality, assume that  $\tau_k^i < \tau_k^{i'}$ , and consequently we have  $n^i < n^{i'}$ .

Then, the  $(l, l)$ -th entry of  $\mathbf{Q}$  is given as

$$\begin{aligned}
& \sum_{n=0}^{N-1} \phi_l(t_n, \tau_k^i, \beta_k^j) * \phi_l(t_n, \tau_k^{i'}, \beta_k^{j'}) \\
&= e^{j 2\pi f_l [(1+\beta_k^j) \tau_k^i - (1+\beta_k^{j'}) \tau_k^{i'}]} \sum_{n=n^{i'}}^{n^i + N_s - 1} e^{-j 2\pi f_l (\beta_k^j - \beta_k^{j'}) t_n}, \quad \text{provided } n^{i'} \leq n^i + N_s - 1, \\
&= e^{j 2\pi f_l [(1+\beta_k^j) \tau_k^i - (1+\beta_k^{j'}) \tau_k^{i'}]} \cdot e^{-j 2\pi f_l (\beta_k^j - \beta_k^{j'}) t_{n^{i'}}} \cdot \frac{1 - e^{-j 2\pi \tilde{N} \pi f_l (\beta_k^j - \beta_k^{j'}) \Delta t}}{1 - e^{-j 2\pi f_l (\beta_k^j - \beta_k^{j'}) \Delta t}}, \\
&= e^{j 2\pi f_l [(1+\beta_k^j) \tau_k^i - (1+\beta_k^{j'}) \tau_k^{i'} - (\beta_k^j - \beta_k^{j'}) t_{n^{i'}} - (\beta_k^j - \beta_k^{j'}) (\tilde{N}-1) \Delta t / 2]} \cdot \frac{\sin(\tilde{N} \pi f_l (\beta_k^j - \beta_k^{j'}) \Delta t)}{\sin(\pi f_l (\beta_k^j - \beta_k^{j'}) \Delta t)},
\end{aligned}$$

where  $\tilde{N} = N_s - (n^{i'} - n^i)$ . Since  $f_l (\beta_k^j - \beta_k^{j'}) \Delta t \approx 0$ , we get

$$\begin{aligned}
& \sum_{n=0}^{N-1} \phi_l(t_n, \tau_k^i, \beta_k^j) * \phi_l(t_n, \tau_k^{i'}, \beta_k^{j'}) \\
&\approx e^{j 2\pi f_l [(1+\beta_k^j) \tau_k^i - (1+\beta_k^{j'}) \tau_k^{i'} - (\beta_k^j - \beta_k^{j'}) (t_{n^{i'}} + (\tilde{N}-1) \Delta t / 2)]} \cdot \frac{\sin(\tilde{N} \pi f_l (\beta_k^j - \beta_k^{j'}) \Delta t)}{\pi f_l (\beta_k^j - \beta_k^{j'}) \Delta t}, \\
&= e^{j 2\pi f_l [(1+\beta_k^j) \tau_k^i - (1+\beta_k^{j'}) \tau_k^{i'} - (\beta_k^j - \beta_k^{j'}) (t_{n^{i'}} + t_{n^i + N_s - 1}) / 2]} \cdot \tilde{N} \operatorname{sinc}(\tilde{N} f_l (\beta_k^j - \beta_k^{j'}) \Delta t),
\end{aligned}$$

and hence the expressions of  $\alpha(l)$  and  $\theta(l)$ .

# References

- [1] M. I. Skolnik, *Introduction to Radar Systems*, 3rd ed. New York, NY: McGraw-Hill, Dec. 2002.
- [2] —, “Fifty years of radar,” *Proc. IEEE*, vol. 73, no. 2, pp. 182–197, Feb. 1985.
- [3] T. May and H. Rohling, “Orthogonal frequency division multiplexing,” in *Wideband Wireless Digital Communications*, A. F. Molisch, Ed. Upper Saddle River, NJ: Prentice Hall PTR, 2001, ch. 17-25.
- [4] P. Z. Peebles, Jr., *Radar Principles*. New York, NY: Wiley-Interscience, Sep. 1998.
- [5] R. H. Dicke, “Object detection system,” U.S. Patent 2 624 876, Jan. 6, 1953.
- [6] R. H. Barker, “Group synchronizing of binary digital system,” in *Communication Theory*, W. Jackson, Ed. London, UK: Academic Press, Inc., 1953, pp. 273–287.
- [7] R. L. Frank, “Phase coded communication system,” U.S. Patent 3 099 795, Jul. 30, 1963.
- [8] —, “Polyphase codes with good nonperiodic correlation properties,” *IEEE Trans. Inf. Theory*, vol. 9, no. 1, pp. 43–45, Jan. 1963.
- [9] B. L. Lewis and F. F. Kretschmer, Jr., “A new class of polyphase pulse compression codes and techniques,” *IEEE Trans. Aerosp. and Electron. Syst.*, vol. AES-17, no. 3, pp. 364–372, May 1981.
- [10] —, “Linear frequency modulation derived polyphase pulse compression codes,” *IEEE Trans. Aerosp. and Electron. Syst.*, vol. AES-18, no. 5, pp. 637–641, Sep. 1982.
- [11] N. Levanon, “Multifrequency radar signals,” in *Records of the IEEE Int. Radar Conf.*, Alexandria, VA, May 7–12, 2000, pp. 683–688.
- [12] —, “Multifrequency complementary phase-coded radar signal,” *IEE Proc. - Radar, Sonar and Navigation*, vol. 147, no. 6, pp. 276–284, Dec. 2000.
- [13] —, “Train of diverse multifrequency radar pulses,” in *Proc. IEEE Radar Conf.*, Atlanta, GA, May 1–3, 2001, pp. 93–98.

- [14] N. Levanon and E. Mozeson, "Multicarrier radar signal - pulse train and CW," *IEEE Trans. Aerosp. and Electron. Syst.*, vol. 38, no. 2, pp. 707–720, Apr. 2002.
- [15] E. Mozeson and N. Levanon, "Multicarrier radar signals with low peak-to-mean envelope power ratio," *IEE Proc. - Radar, Sonar and Navigation*, vol. 150, no. 2, pp. 71–77, Apr. 2003.
- [16] N. Levanon and E. Mozeson, *Radar Signals*. Hoboken, NJ: Wiley-IEEE Press, 2004.
- [17] N. Majurec, S. M. Sekelsky, S. J. Frasier, and S. A. Rutledge, "The advanced multi-frequency radar (AMFR) for remote sensing of clouds and precipitation," in *Proc. 32nd Conf. on Radar Meteorology*, Albuquerque, NM, 2004, paper P1R.6.
- [18] P. V. Genderen, P. Hakkaart, J. V. Heijenoort, and G. P. Hermans, "A multi frequency radar for detecting landmines: Design aspects and electrical performance," in *Proc. 31st European Microwave Conf.*, vol. 2, London, England, Sep. 24–26, 2001, pp. 249–252.
- [19] C. Bennett and J. Toomey, "Target classification with multiple frequency illumination," *IEEE Trans. Antennas Propag.*, vol. 29, no. 2, pp. 352–358, Mar. 1981.
- [20] M. L. Bryan, "Interpretation of an urban scene using multi-channel radar imagery," *Remote Sensing of Environment*, vol. 4, pp. 49–66, 1975.
- [21] Z.-G. Xia, "Applications of multi-frequency, multi-polarization and multi-incident angle SAR systems in urban land use and land cover mapping," in *Int. Geoscience and Remote Sensing Symp.*, vol. 4, Lincoln, NE, May 27–31, 1996, pp. 2310–2314.
- [22] E. F. Knott, "Radar cross section," in *Radar Handbook*, 2nd ed., M. I. Skolnik, Ed. McGraw-Hill, Inc., Jan. 1990, ch. 11.
- [23] S. Weinstein and P. Ebert, "Data transmission by frequency-division multiplexing using the discrete fourier transform," *IEEE Trans. Commun. Technol.*, vol. 19, no. 5, pp. 628–634, Oct. 1971.
- [24] J. Chow, J. Tu, and J. Cioffi, "A discrete multitone transceiver system for HDSL applications," *IEEE J. Sel. Areas Commun.*, vol. 9, no. 6, pp. 895–908, Aug. 1991.
- [25] H. Papadopoulos and C. Sunberg, "Simultaneous broadcasting of analog FM and digital audio signals by means of adaptive precanceling techniques," *IEEE Trans. Commun.*, vol. 46, no. 9, pp. 1233–1242, Sep. 1998.

- [26] R. van Nee, G. Awater, M. Morikura, H. Takanashi, M. Webster, and K. Halford, “New high-rate wireless LAN standards,” *IEEE Commun. Mag.*, vol. 37, no. 12, pp. 82–88, Dec. 1999.
- [27] I. Koffman and V. Roman, “Broadband wireless access solutions based on OFDM access in IEEE 802.16,” *IEEE Commun. Mag.*, vol. 40, no. 4, pp. 96–103, Apr. 2002.
- [28] H. Dai and H. Poor, “Advanced signal processing for power line communications,” *IEEE Commun. Mag.*, vol. 41, no. 5, pp. 100–107, May 2003.
- [29] D. Poullin, “Passive detection using digital broadcasters (DAB, DVB) with COFDM modulation,” *IEE Proc. - Radar, Sonar and Navigation*, vol. 152, no. 3, pp. 143–152, Jun. 2005.
- [30] C. Berger, S. Zhou, P. Willett, B. Demissie, and J. Heckenbach, “Compressed sensing for OFDM/MIMO radar,” in *Proc. 42nd Asilomar Conf. on Signals, Systems and Computers*, Pacific Grove, CA, Oct. 26–29, 2008, pp. 213–217.
- [31] C. Berger, B. Demissie, J. Heckenbach, P. Willett, and S. Zhou, “Signal processing for passive radar using OFDM waveforms,” *IEEE J. Sel. Topics Signal Process.*, vol. 4, no. 1, pp. 226–238, Feb. 2010.
- [32] D. Garmatyuk, “Ultrawideband imaging radar based on OFDM: System simulation analysis,” in *Proc. SPIE*, vol. 6210, no. 1, Orlando, FL, May 2006, paper 621007.
- [33] —, “Simulated imaging performance of UWB SAR based on OFDM,” in *Proc. IEEE Int. Conf. on Ultra-Wideband*, Waltham, MA, Sep. 24–27, 2006, pp. 237–242.
- [34] D. Garmatyuk, J. Schuerger, Y. Morton, K. Binns, M. Durbin, and J. Kimani, “Feasibility study of a multi-carrier dual-use imaging radar and communication system,” in *Proc. 4th European Radar Conf. (EuRAD)*, Munich, Germany, Oct. 10–12, 2007, pp. 194–197.
- [35] D. Garmatyuk, Y. Morton, and X. Mao, “On co-existence of in-band UWB-OFDM and GPS signals: Tracking performance analysis,” in *IEEE/ION Position, Location and Navigation Symp.*, Monterey, CA, May 5–8, 2008, pp. 196–202.
- [36] D. Garmatyuk and J. Schuerger, “Conceptual design of a dual-use radar/communication system based on OFDM,” in *IEEE Military Communications (MILCOM) Conf.*, San Diego, CA, Nov. 16–19, 2008, pp. 1–7.

- [37] D. Garmatyuk, J. Schuerger, K. Kauffman, and S. Spalding, “Wideband OFDM system for radar and communications,” in *Proc. IEEE Radar Conf.*, Pasadena, CA, May 4–8, 2009, pp. 1–6.
- [38] G. Franken, H. Nikookar, and P. van Genderen, “Doppler tolerance of OFDM-coded radar signals,” in *Proc. 3rd European Radar Conf. (EuRAD)*, Manchester, UK, Sep. 13–15, 2006, pp. 108–111.
- [39] M. Ruggiano and P. van Genderen, “Wideband ambiguity function and optimized coded radar signals,” in *Proc. 4th European Radar Conf. (EuRAD)*, Munich, Germany, Oct. 10–12, 2007, pp. 142–145.
- [40] R. Tigrek, W. de Heij, and P. van Genderen, “Solving Doppler ambiguity by Doppler sensitive pulse compression using multi-carrier waveform,” in *Proc. 5th European Radar Conf. (EuRAD)*, Amsterdam, The Netherlands, Oct. 30–31, 2008, pp. 72–75.
- [41] —, “Multi-carrier radar waveform schemes for range and Doppler processing,” in *Proc. IEEE Radar Conf.*, Pasadena, CA, May 4–8, 2009, pp. 1–5.
- [42] —, “Relation between the peak to average power ratio and Doppler sidelobes of the multi-carrier radar signal,” in *Int. Radar Conf.*, Bordeaux, France, Oct. 12–16, 2009, pp. 1–6.
- [43] R. Tigrek and P. van Genderen, “A Golay code based approach to reduction of the PAPR and its consequence for the data throughput,” in *Proc. 4th European Radar Conf. (EuRAD)*, Munich, Germany, Oct. 10–12, 2007, pp. 146–149.
- [44] B. Donnet and I. Longstaff, “Combining MIMO radar with OFDM communications,” in *Proc. 3rd European Radar Conf. (EuRAD)*, Manchester, UK, Sep. 13–15, 2006, pp. 37–40.
- [45] Y. Paichard, J. Castelli, P. Dreuillet, and G. Bobillot, “HYCAM: A RCS measurement and analysis system for time-varying targets,” in *Proc. IEEE Instrumentation and Measurement Technology Conf. (IMTC)*, Sorrento, Italy, Apr. 24–27, 2006, pp. 921–925.
- [46] P. Tran, “Person localization in adverse complex environment (PLACE) frequency agility in OFDM active radars,” Thales Naval Nederland, Delft, The Netherlands, Tech. Rep., Oct. 2006.
- [47] K. van Caekenberghe, K. Brakora, and K. Sarabandi, “A 94 GHz OFDM frequency scanning radar for autonomous landing guidance,” in *Proc. IEEE Radar Conf.*, Boston, MA, Apr. 17–20, 2007, pp. 248–253.
- [48] J. Stralka and G. Meyer, “OFDM-based wideband phased array radar architecture,” in *Proc. IEEE Radar Conf.*, Rome, Italy, May 26–30, 2008, pp. 1–6.

- [49] M. Sebt, A. Sheikhi, and M. Nayebi, "Orthogonal frequency-division multiplexing radar signal design with optimised ambiguity function and low peak-to-average power ratio," *IET Radar, Sonar & Navigation*, vol. 3, no. 2, pp. 122–132, Apr. 2009.
- [50] C. Sturm, E. Pancera, T. Zwick, and W. Wiesbeck, "A novel approach to OFDM radar processing," in *Proc. IEEE Radar Conf.*, Pasadena, CA, May 4–8, 2009, pp. 1–4.
- [51] E. J. Kelly and R. P. Wishner, "Matched-filter theory for high-velocity accelerating targets," *IEEE Trans. Mil. Electron.*, vol. 9, no. 1, pp. 56–69, Jan. 1965.
- [52] J. Speiser, "Wide-band ambiguity functions (Corresp.)," *IEEE Trans. Inf. Theory*, vol. 13, no. 1, pp. 122–123, Jan. 1967.
- [53] S. Sen and A. Nehorai, "Adaptive design of OFDM radar signal with improved wideband ambiguity function," *IEEE Trans. Signal Process.*, vol. 58, no. 2, pp. 928–933, Feb. 2010.
- [54] S. Sen, M. Hurtado, and A. Nehorai, "Adaptive OFDM radar for detecting a moving target in urban scenarios," in *Proc. 4th Int. Waveform Diversity & Design (WDD) Conf.*, Orlando, FL, Feb. 8–13, 2009, pp. 268–272.
- [55] S. Sen and A. Nehorai, "Adaptive OFDM radar for target detection in multipath scenarios," *IEEE Trans. Signal Process.*, vol. 59, no. 1, pp. 78–90, Jan. 2011.
- [56] J. Durek. (2009, Aug. 17) Multipath exploitation radar industry day. Strategic Technology Office, DARPA. [Online]. Available: [http://www.darpa.mil/STO/Solicitations/BAA09-01/presentations/MER\\_Industry\\_Day.pdf](http://www.darpa.mil/STO/Solicitations/BAA09-01/presentations/MER_Industry_Day.pdf)
- [57] J. L. Krolik, J. Farrell, and A. Steinhardt, "Exploiting multipath propagation for GMTI in urban environments," in *Proc. IEEE Conf. on Radar*, Verona, NY, Apr. 24–27, 2006, pp. 65–68.
- [58] R. F. Potthoff and S. N. Roy, "A generalized multivariate analysis of variance model useful especially for growth curve problems," *Biometrika*, vol. 51, no. 3/4, pp. 313–326, Dec. 1964.
- [59] A. Dogandzic and A. Nehorai, "Generalized multivariate analysis of variance: A unified framework for signal processing in correlated noise," *IEEE Signal Process. Mag.*, vol. 20, pp. 39–54, Sep. 2003.
- [60] S. M. Kay, *Fundamentals of Statistical Signal Processing: Detection Theory*. Upper Saddle River, NJ: Prentice Hall PTR, 1998.

- [61] S. Sen, G. Tang, and A. Nehorai, “Multi-objective optimization of OFDM radar waveform for target detection,” *IEEE Trans. Signal Process.*, vol. 59, no. 2, Feb. 2011.
- [62] —, “Multi-objective optimized OFDM radar waveform for target detection in multipath scenarios,” in *44th Asilomar Conf. on Signals, Systems and Computers*, Pacific Grove, CA, Nov. 7–10, 2010.
- [63] E. Candès and T. Tao, “The Dantzig selector: Statistical estimation when  $p$  is much larger than  $n$ ,” *The Annals of Statistics*, vol. 35, no. 6, pp. 2313–2351, 2007.
- [64] K. Deb, *Multi-Objective Optimization Using Evolutionary Algorithms*, 1st ed. John Wiley & Sons, Jun. 2001.
- [65] C. A. C. Coello, G. B. Lamont, and D. A. V. Veldhuizen, *Evolutionary Algorithms for Solving Multi-Objective Problems*, 2nd ed. New York, NY: Springer, 2007.
- [66] E. Zitzler, M. Laumanns, and S. Bleuler, “A tutorial on evolutionary multiobjective optimization,” in *Metaheuristics for Multiobjective Optimisation*, X. Gandibleux, M. Sevaux, K. Sörensen, and V. T’kindt, Eds. Berlin: Springer Lecture Notes in Economics and Mathematical Systems, vol. 535, 2004, pp. 3–37.
- [67] R. T. Marler and J. S. Arora, “Survey of multi-objective optimization methods for engineering,” *Structural and Multidisciplinary Optimization*, vol. 26, no. 6, pp. 369–395, Mar. 2004.
- [68] P. C. Mahalanobis, “On the generalized distance in statistics,” in *Proc. Nat. Inst. Sciences of India*, vol. 2, 1936, pp. 49–55.
- [69] T. W. Anderson, *An Introduction to Multivariate Statistical Analysis*, 3rd ed. Hoboken, NJ: John Wiley & Sons, Inc., 2003.
- [70] K. Deb, A. Pratap, S. Agarwal, and T. Meyarivan, “A fast and elitist multiobjective genetic algorithm: NSGA-II,” *IEEE Trans. Evolutionary Computation*, vol. 6, no. 2, pp. 182–197, Apr. 2002.
- [71] D. Barton, “Low-angle radar tracking,” *Proc. of the IEEE*, vol. 62, no. 6, pp. 687–704, Jun. 1974.
- [72] W. White, “Low-angle radar tracking in the presence of multipath,” *IEEE Trans. Aerosp. and Electron. Syst.*, vol. AES-10, no. 6, pp. 835–852, Nov. 1974.



- [73] Y. Bar-Shalom, A. Kumar, W. Blair, and G. Groves, "Tracking low elevation targets in the presence of multipath propagation," *IEEE Trans. Aerosp. and Electron. Syst.*, vol. 30, no. 3, pp. 973–979, Jul. 1994.
- [74] S. Sen and A. Nehorai, "OFDM MIMO radar with mutual-information waveform design for low-grazing angle tracking," *IEEE Trans. Signal Process.*, vol. 58, no. 6, pp. 3152–3162, Jun. 2010.
- [75] —, "OFDM MIMO radar for low-grazing angle tracking," in *Proc. 43rd Asilomar Conf. on Signals, Systems and Computers*, Pacific Grove, CA, Nov. 1–4, 2009, pp. 125–129.
- [76] —, "OFDM MIMO radar design for low-angle tracking using mutual information," in *Proc. 3rd IEEE Int. Workshop on Computational Advances in Multi-Sensor Adaptive Processing (CAMSAP)*, Aruba, Dutch Antilles, Dec. 13–16, 2009, pp. 173–176.
- [77] J. Wright, "A new model for sea clutter," *IEEE Trans. Antennas Propag.*, vol. 16, no. 2, pp. 217–223, Mar. 1968.
- [78] F. Bass, I. Fuks, A. Kalmykov, I. Ostrovsky, and A. Rosenberg, "Very high frequency radiowave scattering by a disturbed sea surface - Part II: Scattering from an actual sea surface," *IEEE Trans. Antennas Propag.*, vol. 16, no. 5, pp. 560–568, Sep. 1968.
- [79] J. Li and P. Stoica, "MIMO radar with colocated antennas," *IEEE Signal Process. Mag.*, vol. 24, no. 5, pp. 106–114, Sep. 2007.
- [80] A. Nehorai and E. Paldi, "Vector-sensor array processing for electromagnetic source localization," *IEEE Trans. Signal Process.*, vol. 42, pp. 376–398, Feb. 1994.
- [81] B. Hochwald and A. Nehorai, "Identifiability in array processing models with vector-sensor applications," *IEEE Trans. Signal Process.*, vol. 44, pp. 83–95, Jan. 1996.
- [82] A. Doucet, S. Godsill, and C. Andrieu, "On sequential Monte Carlo sampling methods for Bayesian filtering," *Statistics and Computing*, vol. 10, no. 3, pp. 197–208, Jul. 2000.
- [83] M. S. Arulampalam, S. Maskell, N. Gordon, and T. Clapp, "A tutorial on particle filters for online nonlinear/non-Gaussian Bayesian tracking," *IEEE Trans. Signal Process.*, vol. 50, no. 2, pp. 174–188, Feb. 2002.
- [84] B. Ristic, S. Arulampalam, and N. Gordon, *Beyond the Kalman Filter: Particle Filters for Tracking Applications*. Boston, MA: Artech House Publishers, Feb. 2004.

- [85] T. M. Cover and J. A. Thomas, *Elements of Information Theory*, 2nd ed. Wiley-Interscience, Jul. 2006.
- [86] S. Sen and A. Nehorai, “OFDM radar waveform design for sparsity-based multi-target tracking,” in *Proc. 5th Int. Waveform Diversity & Design (WDD) Conf.*, Niagara Falls, Canada, Aug. 8–13, 2010, pp. 18–22.
- [87] —, “Sparsity-based multi-target tracking using OFDM radar,” *IEEE Trans. Signal Process.*, to appear.
- [88] Y. C. Eldar and M. Mishali, “Robust recovery of signals from a structured union of subspaces,” *IEEE Trans. Inf. Theory*, vol. 55, no. 11, pp. 5302–5316, Nov. 2009.
- [89] Y. C. Eldar and H. Bölcskei, “Block-sparsity: Coherence and efficient recovery,” in *Proc. 34th Int. Conf. on Acoustics, Speech, and Signal Processing (ICASSP)*, Taipei, Taiwan, Apr. 19–24, 2009, pp. 2885–2888.
- [90] Y. Eldar, P. Kuppinger, and H. Bölcskei, “Block-sparse signals: Uncertainty relations and efficient recovery,” *IEEE Trans. Signal Process.*, vol. 58, no. 6, pp. 3042–3054, Jun. 2010.
- [91] D. Needell and J. Tropp, “CoSaMP: Iterative signal recovery from incomplete and inaccurate samples,” *Applied and Computational Harmonic Analysis*, vol. 26, no. 3, pp. 301–321, May 2009.
- [92] J. Ville, “Théorie et application de la notion de signal analytique,” *Cables et Transmission*, vol. 2, no. 1, pp. 61–74, 1948.
- [93] P. M. Woodward, *Probability and Information Theory, with Applications to Radar*. New York: McGraw-Hill, 1953.
- [94] —, “Radar ambiguity analysis,” Royal Radar Establishment, Malvern, UK, RRE Technical Note 731, Feb. 1967.
- [95] A. W. Rihaczek, *Principles of High-Resolution Radar*. New York: McGraw-Hill Book Co., 1969.
- [96] N. Levanon, *Radar Principles*. New York: Wiley-Interscience, 1988.
- [97] R. E. Blahut, W. Miller, Jr., and C. H. Wilcox, *Radar and Sonar: Part I*. New York: Springer-Verlag, 1991.
- [98] J.-C. Guey and M. R. Bell, “Diversity waveform sets for delay-Doppler imaging,” *IEEE Trans. Inf. Theory*, vol. 44, no. 4, pp. 1504–1522, Jul. 1998.

- [99] R. A. Altes, "Some invariance properties of the wide-band ambiguity function," *The Journal of the Acoustical Society of America*, vol. 53, no. 4, pp. 1154–1160, Apr. 1973.
- [100] L. H. Sibul and E. L. Titlebaum, "Volume properties for the wideband ambiguity function," *IEEE Trans. Aerosp. and Electron. Syst.*, vol. AES-17, no. 1, pp. 83–87, Jan. 1981.
- [101] Z. b. Lin, "Wideband ambiguity function of broadband signals," *The Journal of the Acoustical Society of America*, vol. 83, no. 6, pp. 2108–2116, Jun. 1988.
- [102] D. C. Lush and D. A. Hudson, "Ambiguity function analysis of wideband radars," in *Proc. IEEE Radar Conf.*, Los Angeles, CA, Mar. 12–13, 1991, pp. 16–20.
- [103] G. S. Antonio, D. R. Fuhrmann, and F. C. Robey, "MIMO radar ambiguity functions," *IEEE J. Sel. Topics Signal Process.*, vol. 1, no. 1, pp. 167–177, Jun. 2007.
- [104] A. I. Sinsky and C. P. Wang, "Standardization of the definition of the radar ambiguity function," *IEEE Trans. Aerosp. and Electron. Syst.*, vol. AES-10, no. 4, pp. 532–533, Jul. 1974.
- [105] C. H. Wilcox, "The synthesis problem for radar ambiguity functions," University of Wisconsin, Madison, WI, MRC Tech. Summary Report 156, Apr. 1960.
- [106] S. Sussman, "Least-square synthesis of radar ambiguity functions," *IRE Trans. Inf. Theory*, vol. 8, no. 3, pp. 246–254, Apr. 1962.
- [107] D. DeLong and E. Hofstetter, "On the design of optimum radar waveforms for clutter rejection," *IEEE Trans. Inf. Theory*, vol. 13, no. 3, pp. 454–463, Jul. 1967.
- [108] C. Stutt and L. Spafford, "A "best" mismatched filter response for radar clutter discrimination," *IEEE Trans. Inf. Theory*, vol. 14, no. 2, pp. 280–287, Mar. 1968.
- [109] R. de Buda, "Signals that can be calculated from their ambiguity function," *IEEE Trans. Inf. Theory*, vol. 16, no. 2, pp. 195–202, Mar. 1970.
- [110] I. Gladkova and D. Chebanov, "On a new extension of Wilcox's method," in *Proc. 5th WSEAS Int. Conf. on Applied Mathematics*, Miami, FL, 2004, pp. 1–6.
- [111] —, "On the synthesis problem for a waveform having a nearly ideal ambiguity surface," presented at the Int. Radar Conf., Toulouse, France, Oct. 18–22, 2004.

- [112] M. Greco, F. Bordonni, and F. Gini, “X-band sea-clutter nonstationarity: Influence of long waves,” *IEEE J. Ocean. Eng.*, vol. 29, no. 2, pp. 269–283, Apr. 2004.
- [113] M. Hurtado and A. Nehorai, “Polarimetric detection of targets in heavy inhomogeneous clutter,” *IEEE Trans. Signal Process.*, vol. 56, no. 4, pp. 1349–1361, Apr. 2008.
- [114] M. S. Bartlett, “Nearest neighbour models in the analysis of field experiments (with discussion),” *Journal of the Royal Statistical Society, Series B*, vol. 40, no. 2, pp. 147–174, 1978.
- [115] G. N. Wilkinson, S. R. Eckert, T. W. Hancock, and O. Mayo, “Nearest neighbour (NN) analysis of field experiments (with discussion),” *Journal of the Royal Statistical Society, Series B*, vol. 45, no. 2, pp. 151–211, 1983.
- [116] M. S. Srivastava and C. G. Khatri, *An Introduction to Multivariate Statistics*. New York: North-Holland, 1979.
- [117] L. Xu, P. Stoica, and J. Li, “A block-diagonal growth curve model,” *Digital Signal Process.*, vol. 16, no. 6, pp. 902–912, Nov. 2006.
- [118] A. T. Craig, “Note on the independence of certain quadratic forms,” *The Annals of Mathematical Statistics*, vol. 14, no. 2, pp. 195–197, Jun. 1943.
- [119] H. Sakamoto, “On the independence of two statistics,” *Res. Mem. Inst. Statist. Math. Tokyo*, vol. 1, no. 9, pp. 1–25, 1944.
- [120] H. H. Andersen, M. Højbjerg, D. Sørensen, and P. S. Eriksen, *Linear and Graphical Models for the Multivariate Complex Normal Distribution*. Springer-Verlag, 1995.
- [121] E. J. Kelly and K. M. Forsythe, “Adaptive detection and parameter estimation for multidimensional signal models,” Lincoln Laboratory, MIT, Lexington, MA, Tech. Rep. 848, Apr. 1989.
- [122] S. S. Wilks, “Certain generalizations in the analysis of variance,” *Biometrika*, vol. 24, no. 3/4, pp. 471–494, Nov. 1932.
- [123] A. K. Gupta and D. K. Nagar, *Matrix Variate Distributions*. Boca Raton, FL: Chapman & Hall/CRC, 2000.
- [124] T. W. Anderson and M. A. Girshick, “Some extensions of the Wishart distribution,” *The Annals of Mathematical Statistics*, vol. 15, no. 4, pp. 345–357, Dec. 1944.

- [125] T. W. Anderson, “The non-central Wishart distribution and certain problems of multivariate statistics,” *The Annals of Mathematical Statistics*, vol. 17, no. 4, pp. 409–431, Dec. 1946.
- [126] A. M. Kshirsagar, “The non-central multivariate beta distribution,” *The Annals of Mathematical Statistics*, vol. 32, no. 1, pp. 104–111, Mar. 1961.
- [127] M. J. Tretter and G. W. Walster, “Central and noncentral distributions of Wilks’ statistic in MANOVA as mixtures of incomplete beta functions,” *The Annals of Statistics*, vol. 3, no. 2, pp. 467–472, Mar. 1975.
- [128] Y. Fujikoshi, “Asymptotic expansions of the non-null distributions of three statistics in GMANOVA,” *Annals of the Institute of Statistical Mathematics*, vol. 26, no. 1, pp. 289–297, Dec. 1974.
- [129] A. Roy and R. Khattree, “On implementation of a test for Kronecker product covariance structure for multivariate repeated measures data,” *Statistical Methodology*, vol. 2, no. 4, pp. 297–306, Dec. 2005.
- [130] —, “Testing the hypothesis of a Kronecker product covariance matrix in multivariate repeated measures data,” in *Proc. 30th Annual SAS® Users Group Int. (SUGI) Conf.*, Philadelphia, PA, Apr.10–13, 2005, paper 199-30.
- [131] G. Tang and A. Nehorai, “The  $\ell_1$ -constrained minimal singular value: A computable quantification of the stability of sparse signal reconstruction,” *IEEE Trans. Inf. Theory*, Apr. 2010, submitted. [Online]. Available: <http://arxiv.org/abs/1004.4222v1>
- [132] S. S. Chen, D. L. Donoho, and M. A. Saunders, “Atomic decomposition by basis pursuit,” *SIAM Jour. on Scientific Computing*, vol. 20, no. 1, pp. 33–61, Aug. 1998.
- [133] D. Malioutov, M. Çetin, and A. S. Willsky, “A sparse signal reconstruction perspective for source localization with sensor arrays,” *IEEE Trans. Signal Process.*, vol. 53, no. 8, pp. 3010–3022, Aug. 2005.
- [134] S. G. Mallat and Z. Zhang, “Matching pursuits with time-frequency dictionaries,” *IEEE Trans. Signal Process.*, vol. 41, no. 12, pp. 3397–3415, Dec. 1993.
- [135] R. Baraniuk and P. Steeghs, “Compressive radar imaging,” in *Proc. IEEE Radar Conf.*, Boston, MA, Apr. 17–20, 2007, pp. 128–133.
- [136] K. R. Varshney, M. Çetin, J. W. Fisher, and A. S. Willsky, “Sparse representation in structured dictionaries with application to synthetic aperture radar,” *IEEE Trans. Signal Process.*, vol. 56, no. 8, pp. 3548–3561, Aug. 2008.

- [137] C.-Y. Chen and P. P. Vaidyanathan, “Compressed sensing in MIMO radar,” in *Proc. 42nd Asilomar Conf. on Signals, Systems and Computers*, Pacific Grove, CA, Oct. 26–29, 2008, pp. 41–44.
- [138] M. A. Herman and T. Strohmer, “High-resolution radar via compressed sensing,” *IEEE Trans. Signal Process.*, vol. 57, no. 6, pp. 2275–2284, Jun. 2009.
- [139] Y. Yu, A. P. Petropulu, and H. V. Poor, “MIMO radar using compressive sampling,” *IEEE J. Sel. Topics Signal Process.*, vol. 4, no. 1, pp. 146–163, Feb. 2010.
- [140] R. Tibshirani, “Regression shrinkage and selection via the lasso,” *Journal of the Royal Statistical Society. Series B (Methodological)*, vol. 58, no. 1, pp. 267–288, 1996.
- [141] E. J. Candès and T. Tao, “Decoding by linear programming,” *IEEE Trans. Inf. Theory*, vol. 51, no. 12, pp. 4203–4215, Dec. 2005.
- [142] E. J. Candès, “The restricted isometry property and its implications for compressed sensing,” *Comptes Rendus Mathématique*, vol. 346, no. 9–10, pp. 589–592, May 2008.
- [143] F. Y. Edgeworth, *Mathematical Physics: An Essay on the Application of Mathematics to the Moral Sciences*. London: C. K. Paul & Co., 1881.
- [144] V. Pareto, *Cours D’Economie Politique, volume I and II*. Lausanne, Switzerland: F. Rouge, 1896.
- [145] J. W. Enslin, “An evolutionary algorithm approach to simultaneous multi-mission radar waveform design,” Master’s thesis, Rochester Institute of Technology, Rochester, NY, Aug. 2007.
- [146] S. Mittal and K. Deb, “Three-dimensional offline path planning for UAVs using multiobjective evolutionary algorithms,” in *IEEE Congress on Evolutionary Computation (CEC)*, Singapore, Sep. 25–28, 2007, pp. 3195–3202.
- [147] B. R. Secrest and G. B. Lamont, “Multiobjective tuning of a multitarget tracking algorithm using an evolutionary algorithm,” in *IEEE Symp. on Computational Intelligence in Multi-Criteria Decision-Making (MCDM)*, Nashville, TN, Mar. 30 – Apr. 2, 2009, pp. 51–57.
- [148] V. Baghel, G. Panda, P. Srihari, K. Rajarajeswari, and B. Majhi, “An efficient multi-objective pulse radar compression technique using RBF and NSGA-II,” in *World Congress on Nature Biologically Inspired Computing (NaBIC)*, Coimbatore, India, Dec. 9–11, 2009, pp. 1291–1296.

- [149] V. Baghel, “Multiobjective optimization – new formulation and application to radar signal processing,” Master’s thesis, National Institute of Technology, Rourkela, India, 2009.
- [150] E. J. Candès, J. Romberg, and T. Tao, “Robust uncertainty principles: Exact signal reconstruction from highly incomplete frequency information,” *IEEE Trans. Inf. Theory*, vol. 52, no. 2, pp. 489–509, Feb. 2006.
- [151] D. L. Donoho, “Compressed sensing,” *IEEE Trans. Inf. Theory*, vol. 52, no. 4, pp. 1289–1306, Apr. 2006.
- [152] E. Candès and M. Wakin, “An introduction to compressive sampling [A sensing/sampling paradigm that goes against the common knowledge in data acquisition],” *IEEE Signal Process. Mag.*, vol. 25, no. 2, pp. 21–30, Mar. 2008.
- [153] J. E. Freehafer, W. T. Fishback, W. H. Furry, and D. E. Kerr, “Theory of propagation in a horizontal stratified atmosphere,” in *Propagation of Short Radio Waves*, D. E. Kerr, Ed. NY: McGraw-Hill Book Company, Inc., 1951.
- [154] H. Hitney, J. Richter, R. Pappert, K. Anderson, and G. Baumgartner, “Tropospheric radio propagation assessment,” *Proc. of the IEEE*, vol. 73, no. 2, pp. 265–283, Feb. 1985.
- [155] A. Giger, *Low-Angle Microwave Propagation: Physics and Modeling*. Boston, MA: Artech House Publishers, Jul. 1991.
- [156] T. Lo and J. Litva, “Low-angle tracking using a multifrequency sampled aperture radar,” *IEEE Trans. Aerosp. and Electron. Syst.*, vol. 27, no. 5, pp. 797–805, Sep. 1991.
- [157] M. A. Sletten, D. B. Trizna, and J. P. Hansen, “Ultrawide-band radar observations of multipath propagation over the sea surface,” *IEEE Trans. Antennas Propag.*, vol. 44, no. 5, pp. 646–651, May 1996.
- [158] D. Kershaw and R. Evans, “Optimal waveform selection for tracking systems,” *IEEE Trans. Inf. Theory*, vol. 40, no. 5, pp. 1536–1550, Sep. 1994.
- [159] S. P. Sira, D. Morrell, and A. Papandreou-Suppappola, “Waveform design and scheduling for agile sensors for target tracking,” in *Proc. 38th Asilomar Conf. on Signals, Systems and Computers*, Pacific Grove, CA, Jul. 4–9, 2004, pp. 820–824.
- [160] S. P. Sira, A. Papandreou-Suppappola, and D. Morrell, “Time-varying waveform selection and configuration for agile sensors in tracking applications,” in *Proc. 30th Int. Conf. on Acoustics, Speech, and Signal Processing (ICASSP)*, vol. 5, Philadelphia, PA, Mar. 18–23, 2005, pp. 881–884.

- [161] H. Hitney, "Frequency diversity effects of evaporation duct propagation," *IEEE Trans. Antennas Propag.*, vol. 38, no. 10, pp. 1694–1700, Oct. 1990.
- [162] A. Zancla, *Modern Topics in Microwave Propagation and Air-Sea Interaction NATO Science Series C*, 1st ed. Boston, MA: Springer, Dec. 1973.
- [163] J. D. Whalen, "Comparison of evaporation duct height measurement methods and their impact on radar propagation estimates," Master's thesis, Naval Postgraduate School, Monterey, CA, Mar. 1998.
- [164] M. Katzin, R. Bauchman, and W. Binnian, "3- and 9-Centimeter propagation in low ocean ducts," *Proc. of the IRE*, vol. 35, no. 9, pp. 891–905, Sep. 1947.
- [165] L. J. Anderson and E. E. Gossard, "Oceanic duct and its effect on microwave propagation," *Nature*, vol. 172, no. 4372, pp. 298–300, Aug. 1953.
- [166] H. Hitney and R. Vieth, "Statistical assessment of evaporation duct propagation," *IEEE Trans. Antennas Propag.*, vol. 38, no. 6, pp. 794–799, Jun. 1990.
- [167] E. Bossé, R. Turner, and D. Dion, "Low-angle tracking in the presence of ducting, coherent and incoherent multipath," Defence Research Establishment Ottawa, Canada, Tech. Rep. 1240, Nov. 1994.
- [168] K. Anderson, B. Brooks, P. Caffrey, A. Clarke, L. Cohen, K. Crahan, K. Davidson, A. D. Jong, G. D. Leeuw, D. Dion, S. Doss-Hammel, P. Frederickson, C. Friehe, T. Hristov, D. Khelif, M. Moerman, J. S. Reid, S. Reising, M. Smith, E. Terrill, and D. Tsintikidis, "The RED experiment: An assessment of boundary layer effects in a trade winds regime on microwave and infrared propagation over the sea," *Bulletin of the American Meteorological Society*, vol. 85, no. 9, pp. 1355–1365, Sep. 2004.
- [169] M. W. Long, *Radar Reflectivity of Land Sea*, 3rd ed. Artech House, Apr. 2001.
- [170] T. Lo and J. Litva, "Use of a highly deterministic multipath signal model in low-angle tracking," *IEE Proc. F - Radar and Signal Process.*, vol. 138, no. 2, pp. 163–171, Apr. 1991.
- [171] J. Huynen, "Measurement of the target scattering matrix," *Proc. of the IEEE*, vol. 53, no. 8, pp. 936–946, Aug. 1965.
- [172] D. Giuli, "Polarization diversity in radars," *Proc. of the IEEE*, vol. 74, no. 2, pp. 245–269, Feb. 1986.
- [173] Y. Bar-Shalom, X. R. Li, and T. Kirubarajan, *Estimation with Applications to Tracking and Navigation*, 1st ed. New York, NY: Wiley-Interscience, Jun. 2001.



- [174] B. Hochwald and A. Nehorai, "Polarimetric modeling and parameter estimation with applications to remote sensing," *IEEE Trans. Signal Process.*, vol. 43, pp. 1923–1935, Aug. 1995.
- [175] K. Ward, C. Baker, and S. Watts, "Maritime surveillance radar. I. Radar scattering from the ocean surface," *IEE Proc. F - Radar and Signal Process.*, vol. 137, no. 2, pp. 51–62, Apr. 1990.
- [176] A. Farina, F. Gini, M. Greco, and L. Verrazzani, "High resolution sea clutter data: Statistical analysis of recorded live data," *IEE Proc. - Radar, Sonar and Navigation*, vol. 144, no. 3, pp. 121–130, Jun. 1997.
- [177] A. Balleri, A. Nehorai, and J. Wang, "Maximum likelihood estimation for compound-Gaussian clutter with inverse gamma texture," *IEEE Trans. Aerosp. and Electron. Syst.*, vol. 43, no. 2, pp. 775–779, Apr. 2007.
- [178] A. Gelman, J. B. Carlin, H. S. Stern, and D. B. Rubin, *Bayesian Data Analysis*, 2nd ed. Chapman & Hall/CRC, Jul. 2003.
- [179] R. A. Thisted, *Elements of Statistical Computing: Numerical Computation*, 1st ed. New York, NY: Chapman & Hall/CRC, Mar. 1988.
- [180] P. M. Woodward and I. L. Davies, "A theory of radar information," *Phil. Mag.*, vol. 41, pp. 1001–1017, Oct. 1951.
- [181] M. Bell, "Information theory and radar waveform design," *IEEE Trans. Inf. Theory*, vol. 39, no. 5, pp. 1578–1597, Sep. 1993.
- [182] Y. Yang and R. Blum, "MIMO radar waveform design based on mutual information and minimum mean-square error estimation," *IEEE Trans. Aerosp. and Electron. Syst.*, vol. 43, no. 1, pp. 330–343, Jan. 2007.
- [183] A. Leshem, O. Naparstek, and A. Nehorai, "Information theoretic adaptive radar waveform design for multiple extended targets," *IEEE J. Sel. Topics Signal Process.*, vol. 1, no. 1, pp. 42–55, Jun. 2007.
- [184] J. R. Roman, D. W. Davis, J. W. Garnham, and P. Antonik, "Waveform diversity via mutual information," *Digital Signal Process.*, vol. 19, no. 1, pp. 45–58, Jan. 2009.
- [185] S. Kullback and R. A. Leibler, "On information and sufficiency," *The Annals of Mathematical Statistics*, vol. 22, no. 1, pp. 79–86, Mar. 1951.
- [186] S. S. Blackman, *Multiple-Target Tracking with Radar Applications*. Dedham, MA: Artech House, Inc., Dec. 1986.

- [187] Y. Bar-Shalom, *Multitarget-Multisensor Tracking: Advanced Applications*. Boston, MA: Artech House, Inc., 1990.
- [188] Y. Bar-Shalom and E. Tse, "Tracking in a cluttered environment with probabilistic data association," *Automatica*, vol. 11, no. 5, pp. 451–460, Sep. 1975.
- [189] T. Fortmann, Y. Bar-Shalom, and M. Scheffe, "Sonar tracking of multiple targets using joint probabilistic data association," *IEEE J. Ocean. Eng.*, vol. 8, no. 3, pp. 173–184, Jul. 1983.
- [190] D. Reid, "An algorithm for tracking multiple targets," *IEEE Trans. Autom. Control*, vol. 24, no. 6, pp. 843–854, Dec. 1979.
- [191] J. Vermaak, S. J. Godsill, and P. Pérez, "Monte Carlo filtering for multi-target tracking and data association," *IEEE Trans. Aerosp. and Electron. Syst.*, vol. 41, no. 1, pp. 309–332, Jan. 2005.
- [192] D. J. Salmond and H. Birch, "A particle filter for track-before-detect," in *Proc. American Control Conf.*, Arlington, VA, Jun. 25–27, 2001, pp. 3755–3760.
- [193] Y. Boers and J. Driessen, "Multitarget particle filter track before detect application," *IEE Proc. - Radar, Sonar and Navigation*, vol. 151, no. 6, pp. 351–357, Dec. 2004.
- [194] C. Kreucher, K. Kastella, and A. O. Hero, "Multitarget tracking using the joint multitarget probability density," *IEEE Trans. Aerosp. and Electron. Syst.*, vol. 41, no. 4, pp. 1396–1414, Oct. 2005.
- [195] R. G. Baraniuk, V. Cevher, M. F. Duarte, and C. Hegde, "Model-based compressive sensing," *IEEE Trans. Inf. Theory*, vol. 56, no. 4, pp. 1982–2001, Apr. 2010.
- [196] G. Visick, "A quantitative version of the observation that the Hadamard product is a principal submatrix of the Kronecker product," *Linear Algebra and its Applications*, vol. 304, no. 1-3, pp. 45–68, Jan. 2000.

# Vita

Satyabrata Sen

- Date of Birth** November 7, 1979
- Place of Birth** Kolkata, India
- Degrees** B.E., Electronics & Tele-Communication Engineering, Jadavpur University, Kolkata, India, June 2002  
M.Tech., Electrical Engineering, Indian Institute of Technology (IIT) Bombay, India, June 2005  
Ph.D., Electrical & Systems Engineering, Washington University in St. Louis, MO, USA, December 2010
- Affiliations** Student member of IEEE Signal Processing Society
- Awards** Second place award in the student paper competition at the *5th Int. Waveform Diversity & Design (WDD) Conf.*, Niagara Falls, Canada, Aug. 8–13, 2010.
- Publications** S. Sen and A. Nehorai, “Sparsity-based multi-target tracking using OFDM radar,” *IEEE Trans. Signal Process.*, to appear.
- S. Sen, G. Tang, and A. Nehorai, “Multi-objective optimization-based OFDM radar waveform design for target detection,” *IEEE Trans. Signal Process.*, vol. 59, no. 2, Feb. 2011.
- S. Sen and A. Nehorai, “Adaptive OFDM radar for target detection in multipath scenarios,” *IEEE Trans. Signal Process.*, vol. 59, no. 1, pp. 78-90, Jan. 2011.
- S. Sen and A. Nehorai, “OFDM MIMO radar with mutual-information waveform design for low-grazing angle tracking,” *IEEE Trans. Signal Process.*, vol. 58, no. 6, pp. 3152–3162, Jun. 2010.
- S. Sen and A. Nehorai, “Adaptive design of OFDM radar signal with improved wideband ambiguity function,” *IEEE Trans. Signal Process.*, vol. 58, no. 2, pp. 928–933, Feb. 2010.

S. Sen and A. Nehorai, "Target detection in clutter using an adaptive OFDM radar," *IEEE Signal Processing Letters*, vol. 16, no. 7, pp. 592–595, Jul. 2009.

S. Sen and A. Nehorai, "Performance analysis of 3D direction estimation based on head-related transfer function," *IEEE Trans. Audio, Speech and Language Process.*, vol. 17, no. 4, pp. 607–613, May 2009.

S. Sen and A. Nehorai, "Exploiting close-to-the-sensor multipath reflections using a human-hearing-inspired model," *IEEE Trans. Signal Process.*, vol. 57, no. 2, pp. 803–808, Feb. 2009.

S. Sen, G. Tang, and A. Nehorai, "Sparsity-based estimation for target detection in multipath scenarios," submitted to *IEEE Radar Conf.*, Kansas City, MO, May 23–27, 2011.

S. Sen, G. Tang, and A. Nehorai, "Multi-objective optimized OFDM radar waveform for target detection in multipath scenarios," in *44th Asilomar Conf. Signals, Systems, and Computers*, Pacific Grove, CA, Nov. 7–10, 2010.

S. Sen and A. Nehorai, "OFDM radar waveform design for sparsity-based multi-target tracking," in *Proc. 5th Int. Waveform Diversity & Design (WDD) Conf.*, Niagara Falls, Canada, Aug. 8–13, 2010, pp. 18–22.

S. Sen and A. Nehorai, "Slow-time multi-frequency radar for target detection in multipath scenarios," in *Proc. 35th Int. Conf. on Acoustics, Speech, and Signal Process. (ICASSP)*, Dallas, TX, Mar. 14–19, 2010, pp. 2582–2585.

S. Sen and A. Nehorai, "OFDM MIMO radar design for low-angle tracking using mutual information," in *Proc. 3rd Int. Workshop on Computational Advances in Multi-Sensor Adaptive Process. (CAMSAP)*, Aruba, Dutch Antilles, Dec. 13–16, 2009, pp. 173–176.

S. Sen and A. Nehorai, "OFDM MIMO radar for low grazing angle tracking," in *Proc. 43rd Asilomar Conf. Signals, Systems, and Computers*, Pacific Grove, CA, Nov. 1–4, 2009, pp. 125–129.

S. Sen, M. Hurtado, and A. Nehorai, “Adaptive OFDM radar for detecting a moving target in urban scenarios,” in *Proc. 4th Int. Waveform Diversity & Design (WDD) Conf.*, Orlando, FL, Feb. 8–13, 2009, pp. 264–268.

S. Sen, R. Singh, and V. M. Gadre, “Bandpass sampling for software radio,” in *XXVIIIth General Assembly of Intl Union of Radio Science (URSI)*, New Delhi, India, Oct. 23–29, 2005.

S. Sen and V. M. Gadre, “An algorithm for minimum bandpass sampling frequency for multiple RF signals in SDR system,” in *Proc. IEEE/SP 13th Workshop on Statistical Signal Process.*, Bordeaux, France, Jul. 17–20, 2005, pp. 327–332.

December 2010

**Adaptive OFDM Radar, Sen, Ph.D. 2010**